BLACK HOLE TRANSIENTS and AM CVn SYSTEMS

by

Walid El-Khoury

Department of Mathematics,
Australian National University,
Canberra, Australia

A thesis submitted for the degree of
Doctor of Philosophy
of the Australian National University

August 24, 1999

To My Family

Contributions of the Candidate

The original work in this thesis consists of versions of three journal papers, either published or submitted for publication. In all three papers, the candidate undertook the original research under the supervision of Professor Dayal T. Wickramasinghe, and with advice from formal advisors Dr Stephen Roberts and Dr Stéphane Vennes. Their contributions are as follows:

- Chapter 3 is a version of the paper published with Professor Wickramasinghe in volume 303, of *Monthly Notices of the Royal Astronomical Society.* The numerical modelling was developed and applied by the candidate, with occasional assistance from Dr Roberts. Professor Wickramasinghe contributed to the discussion.

- Chapter 4 is a version of a paper submitted for publication with Professor Wickramasinghe to *Astronomy & Astrophysics.* The paper was largely the work of the candidate, subject to guidance from Professor Wickramasinghe.

- Chapter 5 is a version of a paper submitted for publication with Dr Vennes and Professor Wickramasinghe to *Astronomy & Astrophysics.* The observational data was obtained and reduced by Dr Vennes. Model-fitting and analysis were undertaken by the candidate.

Walid El-Khoury

Acknowledgements

I owe a considerable debt to my supervisor Professor Dayal Wickramasinghe for his support while preparing this thesis, and for his encouraging supervision which made this work possible.

I am equally indebted to my advisor Dr Stephen Roberts for his valuable help with the numerical aspects of the work.

I am also very grateful to my advisor Dr Stéphane Vennes for his generosity and patience in discussing with me various topics — including classical history — at numerous pubs.

Thanks are also due to Dr Lilia Ferrario, Professor Rainer Wehrse and Professor Ronald Webbink for their helpful feedback throughout my Ph.D. years.

Many staff in ANU's Department of Mathematics have been very supportive, and I particularly would like to thank Dr James Gifford, Nick Guoth and Dr Neville Smythe for their astronomical patience towards my impatience.

This work would not have been completed without the Australian Postgraduate Award offered by the Australian government for which I am very grateful.

While I am indebted to many dear friends and their breakfasts and dinners during the blue Ph.D. days, I wish to gratefully acknowledge the help of my close friend and colleague Michael Burgess, whose constant wonderful generosity and support made life after the Ph.D. a sure reality. I also would like to thank his wife Marion for her kindness and care: words can never do justice to them, nor to the unconditional love and support of my immediate family.

ABSTRACT

We model the vertical structure and emergent spectra of accretion discs using the α-viscosity and thin-disc approximations. The results are applied to the study of accretion discs in two classes of semi-detached compact binaries:

- black hole soft X-ray transients, i.e., low-mass X-ray binaries with black hole accretors which are believed to be subject to thermal accretion disc instabilities. Using a bi-grey disc model, we study the effect of X-ray irradiation on disc stability and compare the results to observed soft X-ray transient data. The common assumption that such X-rays are totally absorbed by the disc is not supported by our results: indeed we show that irradiation can result in the disc becoming optically-thin to X-rays.

- the ultra-compact AM Canum Venaticorum (AM CVn) systems, which are hydrogen-depleted cataclysmic variables. Modelled vertical disc structures are used to calculate emergent optical spectra, which are then fitted — via a χ^2-minimisation technique — to observed data in order to estimate disc parameters. We find good agreement with the observed properties of some AM CVn systems.

Contents

List of Figures

Chapter 1

Thesis Aims, Approach and Structure

1.1 Aims and Approach

The aim of this work is to develop a numerical model of the vertical structure and spectra of accretion discs in interacting low-mass close binary star systems, and apply the model to

- low-mass X-ray binary systems in order to investigate the effects of X-ray irradiation on the thermal stability of the disc, and
- to fit model disc spectra to observed optical spectra for three AM CVn cataclysmic variable systems — AM Canum Venaticorum, CR Bootis and EC15330-14 — in order to estimate disc parameters.

The model describes the steady-state behaviour of accretion discs, and takes as inputs parameters such as mass-transfer rate, mass and radius of the accretor, inclination angle and maximum radius of the disc, as well as gas composition and viscosity parameter. The outputs are vertical profiles of temperature, pressure and density at points in a grid of disc radii, together with the emergent spectrum integrated over all the grid points. It is based on Shaviv and Wehrse's two-stream grey atmosphere model (Shaviv and Wehrse 1986, Wehrse et al. 1994), with minor

modifications when applied to the modelling of AM CVn systems. Significant developments to their model are made in the treatment of X-ray irradiation of the disc through the use of a self-consistent bi-grey approximation. A finite-difference initial-value solver for algebraic-differential equations developed by Brenan et al. (1989) is used to determine the vertical disc structure as a boundary-value problem, with disc thickness and X-ray optical depth as possible eigenvalues.

1.2 Structure

The thesis is organised with an introductory section giving the background to interacting low-mass close binaries, followed by three chapters which consist of journal papers either published or submitted for publication. The final chapter comprises suggestions for future work to improve and apply the model. In more detail the layout is as follows:

- Chapter 2 firstly categorises low-mass close binaries, concentrating on cataclysmic variables and low-mass X-ray binaries which are the subject of this work. Basic physical concepts for interacting close binaries are then discussed which leads into consideration of evolutionary models for such systems. This introduction, which is a review of current knowledge, contains no original contributions but sets the framework for the subsequent three chapters which do.

- Chapter 3 is a version of the paper published with Professor D.T. Wickramasinghe in volume 303 of *Monthly Notices of the Royal Astronomical Society.* The chapter corrects some misprints in the original paper and incorporates some more detail on the methodology of the numerical model. The abstract is as follows:

  > It has recently been suggested that the thermal stability of accretion discs in the high $\dot{M}$ regime may be influenced by X-rays that irradiate the disc. We investigate this problem by calculating the vertical structure of externally X-ray irradiated accretion

discs using a two-stream bi-grey approximation for radiative transfer. The effects of X-ray heating depend on the hardness of the incident X-ray spectrum, and the magnitude of the X-ray flux relative to the viscously-generated flux. For heating by soft X-rays, a temperature inversion occurs in the upper atmosphere of the disc when X-ray heating dominates. For heating by hard X-rays, no significant X-ray inversion occurs. In general, the S-curves become increasingly distorted as the irradiation flux increases. The location of the upper critical point of the S-curve, and the corresponding critical mass-transfer rate above which the disc is thermally stable, is significantly reduced if the heating is predominantly by soft X-rays. Our results are used to discuss the stability of accretion discs in black hole soft X-ray transients: in particular, we show that they lie below the X-ray irradiated instability lines and that one of them, GRO1655-40, is in the regime where the disc instability is first triggered close to the outer edge of the disc.

- Chapter 4 is a version of a paper submitted for publication with Professor D.T. Wickramasinghe to *Astronomy & Astrophysics*. The abstract is as follows:

  Using a model of the vertical structure of accretion discs, we calculate disc spectra across a range of system parameters for the helium-rich AM CVn cataclysmic variables, and investigate thermal instabilities in their discs.

  Applying a χ^2-minimisation technique, predicted HeI and HI continuum and line profiles are compared with those observed for two such systems, AM CVn and CR Boo, to estimate several system parameters. We find:

  - mean accretor masses close to, but somewhat higher than, the $0.7 - 0.8 M_{\odot}$ range predicted by present population synthesis studies;

- typical helium-to-hydrogen number density ratios of $10^2 - 10^4$, consistent with a helium-degenerate donor surrounded by a helium-rich envelope; and
- mass-transfer rates of about $10^{17}\mathrm{gs}^{-1}$, which may place the systems in the region of potential disc instability.

S-curves calculated for the best-fit models are consistent with a thermally-stable disc in AM CVn, and a thermally unstable disc in CR Boo.

- Chapter 5 is a version of a paper submitted for publication with Dr S. Vennes and Professor D.T. Wickramasinghe to *Astronomy & Astrophysics*. The abstract is as follows:

> We attempt to model the observed spectrum of EC15330-1403 by applying χ^2-minimisation techniques to a standard accretion disc model. Spectral phases could not be successfully fitted because of insufficient signal-to-noise, but the time-averaged observed spectrum shows a steeper blue continuum than that predicted for a typical helium-rich accretion disc. The reason, we believe, is a significant external source such as the accreting white dwarf, the disc/accretor boundary layer or the bright spot in the disc's outer region.

Bibliography

[1] Brenan, K. E., Campbell, S. L., & Petzold, L. R. 1989, Numerical Solution of Initial-Value Problems in Differential-Algebraic Equations (New York: Elsevier)

[2] Shaviv, G., & Wehrse, R. 1986, A&A, 159, L5

[3] Wehrse, R., Baschek, B., & Shaviv, G. 1994, in ASP Conf. Ser. Vol. 56, Interacting Binary Stars, ed. A. W. Shafter (Provo: Brigham Young Univ.), 35

Chapter 2

Introduction to Interacting Low-Mass Close Binaries

This chapter begins by categorising low-mass close binaries, concentrating on cataclysmic variables (CVs) and low-mass X-ray binaries (LMXBs) which are the subject of this work. Then basic physical concepts for interacting close binaries are discussed, which leads into consideration of evolutionary models for such systems.

2.1 Categories of Low-Mass Close Binaries

Low-mass close binaries comprise CVs, LMXBs and binary radio pulsars, all of which contain at least one component which is a compact star, i.e., a white dwarf, a neutron star or a black hole. CVs are examples of *semi-detached* close binary systems, in which the compact star — in this case a white dwarf — accretes mass via an accretion disc from a low-mass donor star. For most CVs this low-mass donor is either an M or K dwarf, but at a late evolutionary stage it could be a helium-rich star. LMXBs are similar to CVs but the compact accreting star is either a neutron star or a black hole. Binary radio pulsars — comprising a neutron star and a white dwarf — are examples of *detached* close binary systems, which have no mass transfer between component stars. Semi-detached systems are examples of *interacting* binaries; *contact* binary systems — where the two component stars share a *common envelope* — are also examples of interacting

binary systems. Interacting low-mass close binaries have been the subject of much interest in recent years, as an understanding of them should unravel much of the mystery surrounding their evolution and may give insights into the structure of Active Galactic Nuclei.

Observational data indicate that, for both CVs and LMXBs, the mass M_2 of the donor (or secondary) star is both less than the mass M_1 of the accretor (or primary) and less than a few solar masses. Note that we follow the convention that subscript '1' always refers to the mass-accretor, while subscript '2' always refers to the mass-donor star. Hence, during the evolution of a binary system, a particular component star will have different subscripts if it changes from an accretor to a donor or vice versa.

2.1.1 Cataclysmic Variables

Cataclysmic variables are characterised by their eruptive behaviour which is fed by mass transfer between the two components. The present family of CVs consists of *classical novae*, *dwarf novae*, *recurrent novae*, *nova-like variables* and *helium-rich CVs* (the latter not usually classified separately). Their properties can be summarised as follows — for more detail see Warner (1995a).

- Classical novae are CVs for which only one eruption has been observed. These eruptions seem to be successfully modelled as thermonuclear runaways of accreted hydrogen-rich matter on the surface of the white dwarf primary (Giannone & Weigert 1967, Starrfield 1989).

- Dwarf novae are perhaps the most interesting members of the CV family, since their varied characteristics permit study of many accretion-related phenomena. It is now generally accepted (e.g., Livio 1994) that dwarf nova outbursts are triggered by thermal, or thermal plus tidal, instabilities in the accretion disc. To-date there are three subtypes of dwarf novae:

  - Z Cam systems which exhibit decreases from maximum brightness by about 0.7 mag for extended periods of time.

  - SU UMa systems are well-known for their regular outbursts, on which are superimposed occasional *superoutbursts*. These superoutbursts exceed the maximum brightness of a normal outburst by about 0.7 mag for durations 5-10 longer than normal outbursts (Warner 1995a). High-speed photometry of SU UMa systems also discloses *superhumps*, which are brightness excursions typically lasting from the time of maximum superoutburst intensity to its end. They have a triangular profile of 0.3–0.4 mag amplitude, independent of inclination angle, with periodicity 3% longer than the system's orbital period. The *tidal resonance model*, in which a precessing elliptical ring of higher density gas in the outer disc region causes superhumps, is the commonly-accepted explanation (Whitehurst 1988ab, Whitehurst & King 1991).
  - U Gem systems include the rest of the family of CVs whose characteristics match neither those of Z Cam nor those of SU UMa systems.

- Recurrent novae are previously recognised classical novae which are observed to repeat their thermonuclear eruptions.

- Nova-like variables are relatively stable members of the class of CVs which are believed to be either in a post-eruption or pre-eruption stage of long duration. Also some may be Z Cam systems in a longer brightness standstill than the current observational baseline (Warner 1995a).

- Magnetic CVs include the subclasses *polars* — also known as AM Her systems — which exhibit strong magnetic fields, and *intermediate polars* — also known as DQ Her systems — with weaker magnetic fields. In these systems, magnetic fields significantly disrupt or distort the accretion process (Wickramasinghe 1988).

- Helium-rich CVs are hydrogen-depleted systems. Within this class we only consider AM CVn systems, which are helium-rich binaries with extremely short orbital periods ($\sim$ 18 mins). Presently only six such systems are known, and they are believed to comprise a white dwarf accretor and a helium-rich

degenerate, or semi-degenerate, companion. Some exhibit thermal instabilities similar to those of dwarf novae. The difficulty in understanding the nature of these objects stems from the fact that they exhibit multi-periodic modulations in their light curves, which disguise their binary nature. For this reason, the first ones discovered were originally believed to be single DB white dwarfs, until signatures of accretion phenomena were subsequently noted (Warner 1995ab, O'Donoghue et al. 1994). The investigations reported here tend to confirm that these systems are indeed helium-rich CVs with helium-degenerate donors.

2.1.2 Low-Mass X-ray Binaries

X-ray binaries are systems with a neutron star or a black hole accretor, and are the brightest X-ray sources in the sky. They are divided into two main categories depending on donor mass: those with M_2 greater than a few solar masses are known as high-mass X-ray binaries, and the others as low-mass X-ray binaries. Accretion in the high-mass variety is believed to be due to wind from the massive donor, and is mostly spherical. In this case, the donor dominates the optical spectrum, and its bolometric luminosity is much greater than the X-ray luminosity due to accretion from the inner disc region. On the other hand, the optical spectrum of LMXBs is dominated by accretion disc luminosity, and is significantly enhanced by reprocessed X-rays — i.e., X-rays emitted by the inner regions of the disc but absorbed and reprocessed in the outer regions.

Many LMXBs — termed *soft X-ray transients* (SXTs) — exhibit variations in brightness similar to those observed in some CVs, except that their timescales are much longer (e.g., months and years compared to days and weeks). Those LMXBs that do not display such variations of brightness are termed *persistent*. It is presently accepted wisdom (van Paradijs 1996, King & Ritter 1998) that the brightness variations in SXTs are caused by thermal disc instabilities similar to those in dwarf novae: timescale differences are most likely caused by gravitational field differences and effects due to X-ray heating of the disc. It is also speculated (King et al. 1996, King et al. 1997) that X-ray irradiation effects are greater for

neutron star than for black hole accretors — because of the event horizon associated with black holes — in which case thermal disc instabilities may be more likely for black hole accretors. The investigations into X-ray heating of the disc reported here may shed some light on this issue.

2.2 Basic concepts

For interacting binaries at any era in their history, the key behavioural determinants are mass transfer, stellar timescales and angular momentum losses. We briefly summarise these basic concepts below (see Warner (1995a) or Frank et al. (1992) and references therein, for more comprehensive accounts).

2.2.1 Mass Transfer

In an interacting binary system, mass transfer from donor to accretor occurs when the surface of the donor approaches its Roche equipotential surface (i.e., its *Roche lobe*), causing stellar material to flow from the donor through the Lagrangian L_1 point to an accretion disc within the accretor's Roche lobe.

If q is the donor-to-accretor mass ratio M_2/M_1 and a is the binary separation, then a good fit to the volume radius R_{L2} of the donor's Roche lobe — i.e., the radius of a sphere with the same volume as that enclosed by the donor's Roche lobe — is (Eggleton 1983)

$$R_{L2} = a\frac{0.49q^{2/3}}{0.6q^{2/3} + \ln(1 + q^{1/3})} \qquad : 0 \leq q \leq \infty \tag{2.1}$$

or (Paczyński 1971)

$$R_{L2} = 0.462a\left(\frac{q}{1+q}\right)^{1/3} \qquad : 0 \leq q \leq 0.8. \tag{2.2}$$

With donor radius R_2, the condition for mass transfer via Roche lobe overflow is $R_{L2} = R_2$ which, for donors on the lower main sequence where to a good approximation (e.g., Kippenhahn & Weigert 1990)

$$\frac{R_2}{R_\odot} = \frac{M_2}{M_\odot}\,, \tag{2.3}$$

may be expressed as

$$R_{L2} = \left(\frac{R_\odot}{M_\odot}\right) M_2. \tag{2.4}$$

From this, a useful relationship between orbital period P_{orb} and donor mass M_2 may be derived when $q < 0.8$ by using (2.2) and Newton's generalisation of Kepler's third law

$$P_{orb}^2 = \frac{4\pi^2 a^3}{G(M_1 + M_2)} \tag{2.5}$$

to give

$$P_{orb} \approx \frac{2\pi}{\sqrt{GM_\odot}} \left(\frac{R_\odot}{0.462}\right)^{3/2} \left(\frac{M_2}{M_\odot}\right) = 8.9 \left(\frac{M_2}{M_\odot}\right) \text{hrs}. \tag{2.6}$$

The accretion process releases energy which contributes to the luminosity of the binary system. For a steady-state disc, assuming that matter spirals down to the accretor in essentially Keplerian circular orbits, the binding energy per unit accreting mass at radius R from the accretor is the sum of gravitational potential energy and kinetic energy, i.e., $-GM_1/2R$. In spiralling down to the accretor from the L_1 point, energy equal to $GM_1\dot{M}/2R_1$ per second is therefore dissipated from the accretion disc, where $\dot{M}$ is the disc's mass-transfer rate and R_1 is the radius of the accretor. For both CVs and LMXBs the accretion disc is by far the most significant contributor to system luminosity. But in the process of accretion onto the surface of the accretor, an additional amount of energy equal to $GM_1/2R_1$ per unit accreting mass is given up to the accretor, which contributes to the accretor's luminosity.

According to convention (Kippenhahn & Weigert 1967), mass transfer when the donor is on the main sequence is called Case A. If the donor is on its first ascent of the giant branch — i.e., with shell-hydrogen-burning before core helium ignition — then it is termed Case B mass transfer: if the donor is on the second ascent of the giant branch — i.e., with shell-helium-burning before core carbon ignition — then it is termed Case C.

2.2.2 Timescales

Three basic timescales — namely *dynamical*, *thermal* and *nuclear* — are important in determining the structure and evolution of a star. In an interacting binary system the same timescales describe the response of both the donor to mass loss and of the accretor to mass accretion.

As mass is removed, the donor firstly adjusts adiabatically on a dynamical timescale in order to achieve hydrostatic equilibrium, and the star tends to either expand, if its envelope is convective, or else contract if its envelope is radiative. The dynamical timescale of a star of mass M_2 and radius R_2 can be estimated by the free-fall timescale:

$$\tau_{dyn} \approx \frac{1}{[G < \rho_d >]^{1/2}} \approx 5.1 \times 10^{-5} \left(\frac{M_\odot}{M_2}\right)^{1/2} \left(\frac{R_2}{R_\odot}\right)^{3/2} \text{ yrs}, \tag{2.7}$$

where $< \rho_d >$ is the mean star density and G is the gravitational constant. Typical values for main sequence stars range from 1.2×10^{-4} yrs (i.e., $\sim$ 1 hr) for $M_2 = 10M_\odot$, to 6.3×10^{-6} yrs (i.e., $\sim$ 3 mins) for $M_2 = 0.1M_\odot$.

The consequent expansion or contraction cause changes in core temperature and density, which in turn affects the nuclear burning needed to resupply radiative diffusion or convection of heat to the outer stellar layers. Hence the initial adiabatic changes put the star out of thermal equilibrium, and result in secondary structural changes in order to re-balance the stellar energy budget and restore thermal equilibrium. This process is characterised by the thermal timescale — the time taken by the star to achieve thermal equilibrium — which, for a star of luminosity L_2, is estimated by the ratio of thermal energy content to stellar luminosity:

$$\tau_{th} \approx \frac{GM_2^2/R_2}{L_2} \approx 3.1 \times 10^7 \left(\frac{M_2}{M_\odot}\right)^2 \frac{R_\odot}{R_2} \frac{L_\odot}{L_2} \text{ yrs}. \tag{2.8}$$

Typical values for main sequence stars range from 1.4×10^5 yrs for $M_2 = 10M_\odot$ to 2.8×10^9 yrs for $M_2 = 0.1M_\odot$.

The third timescale, usually the longest, is the nuclear timescale: as the chemical composition inside the star changes there is a succession of nuclear burning cycles on nuclear timescales. The transition from one such cycle to the next is usually separated by an overall expansion of the star, preceded by short periods

of contraction as the next burning cycle is ignited in the stellar core. The nuclear timescale for hydrogen-burning on the main sequence is

$$\tau_{nuc} \approx \frac{M_{H2}\epsilon_N}{L_2} \approx 10^{10}\frac{M_2}{M_\odot}\frac{L_\odot}{L_2} \text{ yrs} \tag{2.9}$$

where M_{H2} is the mass of hydrogen consumed in the donor's core and ϵ_N is the specific energy released by hydrogen burning. Typical values for main sequence stars range from 1.7×10^7 yrs for $M_2 = 10M_\odot$ to 10^{12} yrs for $M_2 = 0.1M_\odot$.

For interacting binary systems there is an additional timescale which is crucial in understanding their behaviour, the donor's mass-loss timescale

$$\tau_{\dot{M}} \approx \frac{M_2}{\dot{M}_2} \approx 6.3 \times 10^8 \left(\frac{M_2}{M_\odot}\right)\left(\frac{10^{17}}{\dot{M}_2}\right) \text{ yrs.} \tag{2.10}$$

Typical values, based on mass-transfer rates inferred from observations, in CVs and LMXBs with $0.7 - 6.0$ hrs orbital periods (corresponding to a $0.1 - 0.7M_\odot$ donor mass range according to (2.6)) lie in the interval $10^7 - 10^{12}$ yrs.

The details of binary evolution are determined by the relative importance of the mass-loss timescale with respect to the dynamical, thermal and nuclear timescales. For example (Webbink 1979), if $\tau_{\dot{M}} \ll \tau_{nuc}$ then the donor's core mass should be very close to that of the donor's progenitor at the start of mass transfer. On the other hand, if mass transfer occurs over timescales longer than τ_{th}, then the star will generally continue to evolve, and core mass increase, until the system is detached.

2.2.3 Angular Momentum Losses

The orbital angular momentum J of a binary system is given by

$$J^2 = \frac{GM_1^2M_2^2}{(M_1 + M_2)}a \tag{2.11}$$

and so the rate of change of binary separation $\dot{a}$ is given by

$$\frac{\dot{a}}{a} = 2\frac{\dot{J}}{J} - \frac{1+2q}{1+q}\frac{\dot{M}_1}{M_1} - \frac{2+q}{1+q}\frac{\dot{M}_2}{M_2} \tag{2.12}$$

which, assuming conservation of mass (i.e., $\dot{M}_1 = -\dot{M}_2$), becomes

$$\frac{\dot{a}}{a} = 2\frac{\dot{J}}{J} + 2(q-1)\frac{\dot{M}_2}{M_2}. \tag{2.13}$$

As $\dot{M}_2 < 0$, this shows that in the absence of orbital angular momentum losses (i.e., $\dot{J} = 0$), mass transfer from the donor will cause binary separation to always decrease if $q > 1$, and to always increase if $q < 1$. We have previously noted that $M_2 < M_1$ — i.e., $q < 1$ — for both CVs and LMXBs so, for these systems, if both mass and angular momentum are conserved, then binary separation must increase. However, this is contrary to what is observed, and therefore orbital angular momentum loss must play an important role in the evolution of CVs and LMXBs.

Apart from cataclysmic events, the most important mechanisms for orbital angular momentum loss in low-mass close binaries are believed to be gravitational radiation and magnetic braking via a magnetised wind from the donor.

Gravitational Radiation

From Einstein's quadrupole formula, the rate of angular momentum loss from gravitational radiation dissipation is (Landau & Lifshitz 1958)

$$\frac{\dot{J}_{GR}}{J} = -\frac{32}{5}\frac{G^3}{c^5}\frac{M_1 M_2 (M_1 + M_2)}{a^4} \tag{2.14}$$

where c is the speed of light. Using (2.5) this may be written as

$$\frac{\dot{J}_{GR}}{J} = -1.3 \times 10^{-8} P_{orb}^{-8/3}(\mathrm{hr}) \left(\frac{M_1}{M_\odot}\right)\left(\frac{M_2}{M_\odot}\right)\left(\frac{M_1}{M_\odot} + \frac{M_2}{M_\odot}\right)^{-1/3} \mathrm{yr}^{-1}. \tag{2.15}$$

Magnetic Braking

Angular momentum losses due to magnetic braking only exist in systems with a magnetic donor star. If such stars are rotating, and also have an ionised stellar wind, then the motion of the plasma in the wind is affected by that magnetic field. In fact, out to a transition distance — the Alfvén radius — where kinetic and magnetic energy densities are equal, the plasma is constrained to corotate with the star, but beyond the Alfvén radius the wind drags the field lines with it: typically (van den Heuvel 1994) the Alfvén radius is $5 - 10$ stellar radii or more. An important consequence of this magnetically-coupled stellar wind is that matter leaves the surface of the star with angular momentum per unit mass corresponding to the Alfvén, rather than stellar, radius. Therefore, the magnetic field enhances

the star's spin angular momentum loss, although the corresponding mass loss is negligible, being of order $10^{-13} M_\odot$ yr^{-1} (van den Heuvel 1994).

It is believed that donor stars in close binaries lose spin angular momentum via this magnetic braking effect and, because of the tidal spin-orbit interaction which tends to keep the component stars always presenting the same face to each other, this translates to orbital angular momentum losses. Models of magnetic braking frequently use the empirical finding (Skumanich 1972) that the equatorial velocity of G dwarfs decays with time as $t^{-1/2}$ from which, assuming that this relationship holds for synchronously rotating close binary donor stars, it can be shown (Verbunt & Zwaan 1981) that

$$\dot{J}_{MB} = -5 \times 10^{-29} f_{MB}^{-2} k_R^2 M_2 R_2^4 \left(\frac{2\pi}{P_{orb}}\right)^3 \text{ dyne cm} \tag{2.16}$$

where k_R is the star's radius of gyration ($k_R^2 \approx 0.1$ for lower main sequence stars) and f_{MB} is a parameter of order unity. Hence, using (2.5) and (2.11)

$$\frac{\dot{J}_{MB}}{J} = -5 \times 10^{-29} f_{MB}^{-2} k_R^2 \frac{G(M_1 + M_2)^2}{M_1 a^5} R_2^4 \text{ sec}^{-1} \tag{2.17}$$

$$= -9.1 \times 10^{-5} \frac{f_{MB}^{-2} k_R^2}{P_{orb}^{10/3}(\text{hr})} \left(\frac{R_2}{R_\odot}\right)^4 \left(\frac{M_1}{M_\odot} + \frac{M_2}{M_\odot}\right)^{1/3} \left(\frac{M_1}{M_\odot}\right)^{-1} \text{ yr}^{-1}. \tag{2.18}$$

Although the mechanisms behind stellar magnetic fields are not well understood, it is believed that differential rotation between convective and radiative stellar layers is the most likely dynamo. If this is the case, then stars of mass less than about $0.3 M_\odot$ would not be expected to have magnetic fields, since they are fully-convective.

The relationship between $\dot{J}$ and $\dot{M}$

The relative importance of magnetic braking and gravitational radiation in determining orbital behaviour for low-mass close binaries may be seen by assuming the mass-radius, and consequent period-mass, relationships (2.3) and (2.6) for lower main sequence donors with $q < 0.8$. In that case, from (2.15) and (2.18)

$$\frac{\dot{J}_{MB}}{\dot{J}_{GR}} = 1.6 \times 10^3 f_{MB}^{-2} k_R^2 \left(\frac{M_1}{M_\odot} + \frac{M_2}{M_\odot}\right)^{2/3} \left(\frac{M_2}{M_\odot}\right)^{7/3} \left(\frac{M_1}{M_\odot}\right)^{-1}. \tag{2.19}$$

Typically for CVs $M_1/M_\odot \approx 1$, $f_{MB} \approx 1$ and $k_R^2 \approx 0.1$ and so

$$\frac{\dot{J}_{MB}}{\dot{J}_{GR}} = 160 \left(1 + \frac{M_2}{M_\odot}\right)^{2/3} \left(\frac{M_2}{M_\odot}\right)^{7/3} \tag{2.20}$$

and it is clear that magentic braking is dominant provided $M_2/M_\odot$ exceeds about 0.1, i.e., for periods greater that about 1 hr. But the question arises as to how well these models of orbital angular momentum loss accord with mass-transfer rates deduced from observational data. For quasi-steady-state mass transfer between binary components — a typical scenario during later stages of low-mass close binary evolution — the effect of angular momentum losses on mass-transfer rate can be established as follows.

The $R_2 = R_{L2}$ condition for quasi-steady-state mass transfer from the donor's Roche lobe, assuming mass conservation with (2.1), becomes

$$R_2(M_2, t) = R_{L2}(M_2, a) \tag{2.21}$$

where nuclear and thermal evolution of the donor account for the *explicit* dependence of R_2 on time t. Therefore

$$\frac{d}{dt}\{\ln R_2(M_2, t)\} = \frac{d}{dt}\{\ln R_{L2}(M_2, a)\} \tag{2.22}$$

which, using (2.12), may be expressed as

$$\xi_S \frac{\dot{M}_2}{M_2} + \zeta_R = \xi_J \frac{\dot{M}_2}{M_2} + 2\frac{\dot{J}}{J} \tag{2.23}$$

where, for entropy S

$$\left.\frac{\partial \ln R_2}{\partial \ln M_2}\right|_S = \xi_S \tag{2.24}$$

is the donor's adiabatic (here equivalent to 'instantaneous' or 'within dynamical timescales') radius-mass coefficient,

$$\left.\frac{\partial \ln R_2}{\partial t}\right|_{M_2} = \zeta_R \tag{2.25}$$

is the change in donor's radius due to nuclear and thermal evolution only, and

$$\left.\frac{\partial \ln R_{L2}}{\partial \ln M_2}\right|_J = \xi_J \tag{2.26}$$

depends only on M_1 and M_2. Hence, for quasi-steady-state conditions

$$\frac{2\dot{J}}{J} - \zeta_R = (\xi_S - \xi_J)\frac{\dot{M}_2}{M_2} \tag{2.27}$$

and, as $|\zeta_R| \ll 2|\dot{J}/J|$ together with $(\xi_S - \xi_J) \sim 1$ for typical low-mass close binary configurations (D'Antona et al. 1989) , we can say

$$\frac{\dot{J}}{J} \sim \frac{\dot{M}_2}{M_2}. \tag{2.28}$$

From observations of CVs and LMXBs, we find that for orbital periods between 3.0 hrs and 1 day the inferred mass-transfer rates — 10^{-8} to $10^{-11} M_\odot$ yr^{-1} — tend to be larger than those — 10^{-10} to $10^{-11} M_\odot$ yr^{-1} — for systems with periods in the range $2.0 - 0.7$ hr. These estimates fit well with (2.28) if orbital angular momentum losses from magnetic braking per (2.18) dominate in longer period systems, and only gravitational radiation losses per (2.15) apply to the shorter period ones. So, in general terms, observational data supports the models of orbital angular momentum loss. However, the predicted 1 hr orbital period for transition from one loss mechanism to the other does not accord with puzzling observational data pertaining to periods in the $2 - 3$ hrs interval.

The period gap

The number of CVs or LMXBs with orbital periods in the range $2.2 - 2.8$ hrs is significantly less than the number outside this range. In the case of LMXBs, this *period gap* appears to extend down to 1 hr (White et al. 1995), but the interpretation of observed number densities of LMXBs in terms of a period gap has been questioned (King 1998). The most popular explanation for the period gap hypothesises a sharp reduction in angular momentum loss due to magnetic braking as the period decreases to about 3 hrs, when the donor tends to become fully-convective and non-magnetic. Now low-mass donors with $P_{orb} \leq 6$ hrs have significant convective envelopes which swell adiabatically for mass loss at timescales less than the envelope's thermal relaxation time: so any sharp reduction in $\dot{J}/J$ — and hence, via (2.28), in $\dot{M}_2/M_2$ — when $P_{orb} \approx 3$ hrs, causes the donor to shrink within its Roche lobe and cease mass transfer. Eventually, as the orbit decays from

gravitational radiation and $P_{orb} \approx 2$ hrs, the binary components get close enough to restart mass transfer on gravitational-radiation timescales per (2.28).

However, while plausible, this model is not entirely satisfactory: in particular the basis on which it rests — the stellar dynamo mechanism — is not understood, let alone why there should be an abrupt transition when $P_{orb} \approx 3$ hrs. Interestingly, Pylyser & Savonije (1988b) observe that the commonly accepted explanation of a transition to a fully-convective star at $P_{orb} \approx 3$ hrs holds for most low-mass donors except highly-evolved ones, which seem to become fully-convective when $P_{orb} \approx 2$ hrs. As LMXBs are believed to have more highly-evolved donor stars (see below), this may help resolve questions about the period gap for LMXBs raised in King (1998).

The period minimum

Apart from a period gap, the observed period distribution of low-mass close binaries with hydrogen-burning donors also shows evidence of a *minimum period* — i.e., a scarcity of systems with $P_{orb} < 40$ mins (Pylyser & Savonije 1988b). This is well-explained (e.g., Paczyński & Sienkiewicz 1981, Rappaport et al. 1982, Paczyński & Sienkiewicz 1983, Savonije et al. 1986, Pylyser & Savonije 1988b) by noting that, with orbital decay from gravitational radiation for $P_{orb} \leq 2$ hrs, eventually the donor's convective envelopes will swell adiabatically when the envelope's thermal timescale exceeds that of angular momentum losses due to gravitational radiation. Moreover, this expansion will tend to extinguish nuclear burning in the low-mass donor, making it move to a semi or fully-degenerate state and therefore liable to expand further with mass loss. Under these circumstances, it is evident from (2.13) that the consequent rapid increase in mass-transfer rate will ultimately dominate the rate of angular momentum loss and cause binary separation — and therefore P_{orb} — to increase. Hence the binary experiences a period minimum, and subsequently continues to expand under mass loss driven by gravitational radiation.

The actual minimum orbital period depends on donor mass and evolutionary state. Evolutionary studies by Pylyser & Savonije (1988b) conclude that hydrogen-burning systems with relatively unevolved donors (i.e., core hydrogen abundances

$X_c = 0.6 - 0.7$) at commencement of mass transfer typically experience a minimum period near 80 mins, which is halved for evolved systems (i.e., $X_c = 0.1 - 0.3$). Savonije et al. (1986) modelled a close binary with an even more evolved $0.6M_\odot$ core helium-burning donor commencing mass transfer to a $1.3M_\odot$ compact companion. Compared to hydrogen-burning donors of the same mass, such donors have much reduced radii (typically by a factor of 0.25), Roche lobe and orbital separation, and hence experience higher mass-transfer rates. It was found that gravitational radiation caused the orbit to decay to a minimum period of 10.6 mins, when donor mass shrank to about $0.2M_\odot$, after which binary separation increased with the donor remaining semi-degenerate for a significant part of its further evolution.

2.3 Evolution

We now review current theories on the evolution of low-mass close binaries. There seems to be a consensus view on evolutionary processes for CVs that have main sequence donors, but much work remains to be done before there is a similar consensus on the evolution of LMXBs and helium-rich CVs such as AM CVn systems.

From the fact that all low-mass close binaries have a compact component star, we can reasonably deduce that the progenitor binary system contained a star which evolved off the main sequence. For example, accretors in CVs tend to have masses in the range $0.5 - 1.2M_\odot$, and are believed to be C-O or O-Ne-Mg white dwarfs (van den Heuvel 1994). This strongly suggests their progenitor stars evolved to the shell-helium-burning giant branch with an initial mass between $3 - 10M_\odot$ and, while on that branch, they somehow lost their envelope to expose the white dwarf core. Chemically homogeneous stars seem to offer the only alternative route to a white dwarf without the necessity of evolution to the giant branch, but they require a much more efficient mixing mechanism than currently predicted by stellar evolutionary theory.

Assuming evolution to the shell-helium-burning giant branch, stellar evolutionary theory predicts that the radius of the compact star progenitor must have been between $28R_\odot$ (corresponding to $3M_\odot$ at the base of the branch) and $50R_\odot$ (corresponding to $10M_\odot$). Further assuming that it was also the more massive component

in a binary system, and that Case C mass transfer through its L_1 point initiated processes leading to loss of its envelope, use of the Roche lobe equation (2.1) in the limit as $q \to \infty$, shows that the binary separation in that progenitor system was at least $34R_\odot$. But binary separations for CVs observed at the present epoch are typically $0.5 - 2.4R_\odot$, so it is clear that some mass transfer during CV evolution is far from conservative because significant mass and angular momentum must have been lost from the system.

We use this example of a typical progenitor system for low-mass close binaries to explain below likely mechanisms for three evolutionary stages to reach present configurations. Against this background, we then briefly survey evolutionary paths for the two low-mass close binary systems of interest here; namely AM CVn systems and LXMBs.

2.3.1 Initial Roche Lobe Overflow

The scenario under consideration has a binary with one $3 - 10M_\odot$ component reaching the shell-helium-burning giant branch, together with a companion of lesser mass still on the main sequence. On that giant branch, stellar envelopes expand dramatically, so the $3 - 10M_\odot$ component will eventually begin to overflow its Roche lobe and become a Case C mass donor for the system.

We know from (2.1) and (2.13) that, assuming conservation of mass within the binary system

$$R_{L2} = a\frac{0.49q^{2/3}}{0.6q^{2/3} + \ln(1 + q^{1/3})} \tag{2.29}$$

and

$$\frac{\dot{a}}{a} = 2\frac{\dot{J}}{J} + 2(q-1)\frac{\dot{M}_2}{M_2}. \tag{2.30}$$

Hence, noting that with conservation of mass

$$\frac{\dot{q}}{q} = (1+q)\frac{\dot{M}_2}{M_2}, \tag{2.31}$$

we have

$$\frac{\dot{R}_{L2}}{R_{L2}} = 2\frac{\dot{J}}{J} - 2\frac{\dot{M}_2}{M_2}\left\{1 - q + \frac{1+q}{3}\left(\frac{0.5\frac{q^{1/3}}{1+q^{1/3}} - \ln(1+q^{1/3})}{0.6q^{2/3} + \ln(1+q^{1/3})}\right)\right\} \tag{2.32}$$

and if angular momentum is conserved — i.e., $\dot{J} = 0$ — then, as $\dot{M}_2 < 0$, the Roche lobe contracts over time if

$$1 - q + \frac{1+q}{3}\left(\frac{0.5\frac{q^{1/3}}{1+q^{1/3}} - \ln(1+q^{1/3})}{0.6q^{2/3} + \ln(1+q^{1/3})}\right) < 0. \tag{2.33}$$

This condition is satisfied for all $q > 0.76$ so in the scenario we are examining, providing $M_2 > 0.76M_1$, the Roche lobe of the donor on the shell-helium-burning giant branch shrinks as mass loss proceeds. But stars on that branch have convective envelopes, and it is characteristic of such envelopes to expand with mass loss. In this situation, large-scale mass transfer will occur over dynamical timescales and, as the Roche lobe continues to shrink while (2.33) holds, runaway mass transfer from the donor's envelope is inevitable.

The response of the accretor to such high rates of mass transfer is also important. Firstly, when the mass-transfer rate exceeds the critical *Eddington limit* where radiation pressure forces from the accretor exceed gravitational forces at its surface, then the accretor accepts no more mass and material from the runaway donor remains circulating in the accretor's Roche lobe. Secondly, while the runaway mass-transfer timescale may be greater than the accretor's dynamical timescale, its thermal timescale almost certainly will not be. Consequently, the accretor will probably not be able to achieve thermal equilibrium and (van den Heuvel 1994) will rapidly expand and begin to resemble a pre-main sequence star on the Hayashi track, invariably filling its Roche lobe.

Therefore, a short time after initial mass transfer commences, the progenitor binary system comprises two component stars which fill their respective Roche lobes and form a contact binary. Envelope material from the more massive donor forms a common envelope within the Roche equipotential surface through either the L_2 or L_3 Lagrangian points: in some instances, mass and angular momentum loss from the system could occur through these outer Lagrangian points.

2.3.2 The Common Envelope Phase

The common envelope mechanism for low-mass close binary evolution was originally suggested by Paczyński (1976) and Ostriker (1976) after it became clear —

e.g., see Kruszewski (1966) and Paczyński (1971) — that there was no reasonable evolutionary mechanism which conserved both mass and angular momentum.

In the early stages of the common envelope phase, with both components filling their Roche lobe, the increasingly envelope-depleted high-mass donor may be viewed as orbiting the low-mass accretor within an ever-burgeoning common envelope. The donor therefore experiences a drag force, and consequently dissipates orbital binding energy into that common envelope. Hence, during this stage of the common envelope phase, binary separation decays while the envelope becomes heated, although mass and angular momentum are largely conserved. Numerical modelling of this process is difficult (Livio 1994) as it needs to take into account three-dimensional hydrodynamic and thermodynamic processes occurring over a wide range of length and timescales. But the modelling which has been done (e.g., Livio & Soker 1988, Taam & Bodenheimer 1989) shows that

- the timescale of orbital decay is very short, typically of order $100 - 1000$ years,
- in such timescales, the amount of envelope material captured by the accretor is negligible so — from (2.33) — providing the donor's core mass $M_c > 0.76M_1$, the donor will be stripped of its envelope to expose the core, and
- orbital energy deposited into the common envelope cannot be radiated away, because thermal relaxation timescales for the common envelope are much greater than the orbital-decay timescale.

Initially the common envelope is bound to the binary system and has gravitational binding energy $-\Delta E_{env}$. Therefore, the fact that energy from the donor's orbital decay passes to the common envelope with high efficiency, suggests the possibility that the binding energy of the common envelope might become positive. The envelope will then be ejected from the binary system and, as detailed modelling shows (e.g., Soker & Livio 1989), mass ejection occurs in a narrow region around the orbital plane similar to a planetary nebula and generally occurs by the time the period of the embedded binary is less that about a day. The critical parameter which determines the final outcome of the common envelope phase is

the efficiency factor $\Delta E_{env}/\Delta E_{orb}$, where ΔE_{orb} is the change in orbital binding energy between initial and final configurations. It is a reasonable assumption that if this efficiency factor becomes equal to one then the common envelope is ejected (Webbink 1984): in that case the exposed degenerate core of the high-mass donor may become either the white dwarf component of a cataclysmic variable or, if the donor is sufficiently massive, it may evolve to become a neutron star or a black hole in an LMXB. Applying Monte Carlo techniques, de Kool (1990) studied the evolution of a synthesised population of zero-age main sequence binaries, and confirmed that an efficiency factor close to one gives a predicted number of planetary nebulae incorporating binaries of period less than 1 day, which is in reasonable agreement with the observed number. In fact, the observation of a number of planetary nebulae with embedded short-period binaries containing either a white dwarf or a white dwarf precursor and a low-mass unevolved companion is the best evidence in support of the common envelope theory (Ritter 1986).

We may use the "efficiency factor equal to one" condition to estimate the final binary system configuration at the end of the common envelope phase (e.g., see Verbunt (1993) and references therein). Consider a donor with mass $M_2 = M_c + M_e$, where M_c and M_e are core and envelope masses respectively. The rapidity, and hence adiabatic nature of mass transfer from the donor to form the common envelope, means that the initial binding energy of the common envelope is effectively the gravitational binding energy of the donor's envelope at the start of Roche lobe overflow. Hence the magnitude of the common envelope's gravitational binding energy

$$\Delta E_{env} = \frac{GM_2M_e}{\lambda R_2} \tag{2.34}$$

where $\lambda = \lambda(M_e, M_c)$ is a dimensionless parameter dependent on the donor's envelope structure. Furthermore, the change in orbital binding energy of the system is

$$\Delta E_{orb} = \left(\frac{GM_cM_1}{2a_f} - \frac{GM_1M_2}{2a_i} \right) \tag{2.35}$$

where a_i and a_f are respectively the initial and final star binary separations. The

condition for envelope ejection is $\Delta E_{env} = \Delta E_{orb}$, or

$$\frac{GM_2M_e}{\lambda R_2} = \left(\frac{GM_cM_1}{2a_f} - \frac{GM_1M_2}{2a_i}\right) \tag{2.36}$$

which can be written as

$$\frac{a_f}{a_i} = \frac{M_c}{M_2}\left(1 + \frac{2a_iM_e}{\lambda R_2M_1}\right)^{-1}. \tag{2.37}$$

If $a_f < R_c + R_1$ after the common envelope is expelled, then the accretor and core of the donor will merge: otherwise the binary will survive as a detached system.

2.3.3 The Post-Common Envelope Stage

After the dramatic and rapid changes of the common envelope phase there is an era of relatively slow evolutionary change. A useful way of investigating post-common envelope evolution is to consider whether or not the detached binary system remaining after ejection of the common envelope experiences significant orbital angular momentum losses (e.g., Taam et al. 1980, Pylyser & Savonije 1988ab).

As discussed earlier, the dominant angular momentum loss mechanisms for low-mass close binaries are believed to be magnetic braking and gravitational radiation, with magnetic braking being relatively more important at large orbital separations and vice versa for small separations. In the aftermath of the common envelope phase, if there are no significant angular momentum losses then, ultimately, expansion via nuclear evolution of the non-compact component will initiate mass transfer from its Roche lobe. Assuming angular momentum losses remain negligible, then from (2.13) and (2.33),

- binary separation will decrease if $q > 1$ at a rate determined by the structure of the donor and the interplay between, on the one hand, the donor's mass-loss timescale and, on the other, its dynamical, thermal and nuclear timescales; until

- when $q < 1$ binary separation increases and, although the donor's Roche lobe will contract while $q > 0.76$, eventually mass transfer stops. If the donor

depletes its envelope before mass transfer ceases, then its exposed core may evolve to a compact object. This $q < 1$ case is a possible evolutionary route for both wide LMXBs (Webbink et al. 1983) and pulsars (Paczyński 1983, Savonije 1983) .

Alternatively, if there are significant orbital angular momentum losses after the common envelope phase then the binary is *captured* (Taam et al. 1980, Pylyser & Savonije 1988ab), in which case orbital separation decreases until mass transfer is initiated. For any given post-common envelope configuration, whether or not a binary is captured depends upon the angular momentum loss mechanism. For example, as magnetic braking losses are relatively more important in wide binaries, a configuration with large binary separation and only gravitational radiation losses may not be captured, but the same configuration with magnetic braking may well be.

For captured systems, the donor's post-common envelope evolutionary path depends on its stage of nuclear evolution and hence, noting that more massive stars evolve faster, its mass. Following Pylyser & Savonije (1988b) and Tutukov & Yungelson (1996), we examine three levels of donor core hydrogen abundance X_c at the initiation of mass transfer.

- The donor star is on the zero-age main sequence with initial $X_c \geq 0.6 - 0.7$. In this case, studies (Pylyser & Savonije 1988b) show that the mass-loss timescale is much shorter than the nuclear timescale of the donor. Consequently, there will be little stellar evolution as the donor loses mass, and it evolves down the zero-age main sequence until becoming fully-convective at the Hayashi track: there nuclear-burning will tend to be extinguished and the donor become fully-degenerate.

- For more evolved donor stars with $X_c = 0.1 - 0.3$, it is found that the nuclear timescale is comparable or less than the mass-loss timescale. Consequently stellar evolution proceeds as the donor loses mass, its core density increases, and it leaves the zero-age main sequence to ultimately become, in most cases, a degenerate star with hydrogen envelope.

- The helium-rich binaries which have even more evolved donors at the commencement of mass transfer (e.g., $X_c \sim 0$) are examined in population synthesis studies by Tutukov & Yungelson (1996). They demonstrate that there are three possible paths for the subsequent evolution of the donor, leading to either a helium-degenerate dwarf, a helium-burning non-degenerate star or a helium-mantle star with C-O core. However, selection effects act against identifying either of the latter two as donors in a semi-detached system, as their intrinsic luminosity dominates that of the binary, leading to them being interpreted as singletons.

2.3.4 AM CVn Evolution

Faulkner et al. (1972) originally suggested that AM CVn systems were interacting white dwarf binaries, in which a low-mass white dwarf donor transfers mass via a hydrogen-deficient accretion disc to a white dwarf accretor. The Tutukov & Yungelson (1996) studies mentioned above compared birth rates for the three types of helium-rich binaries, and found that systems with helium-degenerate donors were generated more frequently than the other two types. The results also show that the range of orbital periods of systems with helium-degenerate donors overlap with that of the observed periods of AM CVn systems. Taking into account that the selection effects noted above militate against the other two types being observed as AM CVn systems, there seems every reason to suppose that AM CVn binaries contain a degenerate helium donor. With this assumption, a possible evolutionary path for AM CVn systems is as follows (Tutukov & Yungelson 1996).

The progenitor of the present white dwarf accretor has a $1.5 - 6M_{\odot}$ mass, and experiences Case C Roche lobe overflow in a $60 - 1000R_{\odot}$ orbit around the current donor's progenitor — which is less massive, subject to an approximate $2.5M_{\odot}$ maximum mass. This generates a common envelope and gives birth to a $0.65M_{\odot}$ C-O white dwarf — the present accretor. The subsequent detached system starts mass transfer, which leads to the current donor's progenitor experiencing Case B Roche lobe overflow and a second common envelope phase. The post-common envelope scenario which follows has a binary comprising a C-O white dwarf and a

helium-rich white dwarf: the latter becomes the present donor when orbital angular momentum losses from gravitational radiation bring the two close enough for mass transfer to commence.

2.3.5 LMXB Evolution

If the initial progenitor mass of a low-mass close binary accretor exceeds a value somewhere in the $8-10M_\odot$ range, then present wisdom (Verbunt & van den Heuvel 1995) is that evolution to an LXMB is possible. One evolutionary path, parallelling evolution in a high-mass singleton, requires completion of several nuclear-burning cycles until the progenitor's core is predominantly iron. The core then undergoes endothermic photo-disintegration and gravitational collapse, which explosively ejects the progenitor's envelope in a supernova, and fuses core protons and electrons into neutrons. If neutron-degeneracy pressure ultimately dominates gravitational forces in the collapse, then the remnant core becomes a neutron star; otherwise, for initial progenitor masses exceeding about $40M_\odot$, it becomes a black hole.

Other evolutionary paths are possible (see below) but, as most involve a supernova stage, the trick with LMXBs is for the low-mass companion to survive that stage and remain a binary component. A simple model suggests under what conditions survival may occur. Consider the low-mass companion of mass M_2 in a circular orbit of radius a around the supernova progenitor of mass M_1; assume an instantaneous supernova explosion, with rapid spherically-symmetric ejection of the envelope shell of mass δM. In the rest frame of the supernova, just after the ejected shell passes the orbit of M_2, the total energy E of the system is the sum of kinetic and potential energies which, in the reduced-mass formalism, is

$$E = \frac{1}{2}\frac{(M_1 - \delta M)M_2}{(M_1 - \delta M + M_2)}V_2^2 - \frac{G(M_1 - \delta M)M_2}{a} \tag{2.38}$$

where V_2 is the corresponding orbital velocity of M_2. But both orbital radius and velocity remain unchanged as the high-velocity ejected shell passes the orbit of M_2, so

$$V_2^2 = \frac{G(M_1 + M_2)}{a} \tag{2.39}$$

and, substituting this in (2.38), we find

$$E = \frac{G(M_1 - \delta M)M_2}{2a}\left(\frac{M_1 + M_2}{M_1 - \delta M + M_2} - 2\right). \tag{2.40}$$

For the binary to remain a bound system requires $E < 0$, or

$$\delta M < \frac{M_1 + M_2}{2}, \tag{2.41}$$

so the binary will not survive if the supernova ejects more than about half the initial system mass.

Therefore, to ensure that the envelope of the compact object's progenitor is small at the supernova stage, LMXB evolution scenarios usually rely on significant mass-loss mechanisms: stellar winds in high-mass progenitors and common envelope episodes are examples. Furthermore, the randomly-directed *kick velocity* imparted to a newborn neutron star by asymmetries during core collapse (Lyne et al. 1982), although usually disruptive, is sometimes enlisted to *maintain* binary stability if it is — by coincidence — appropriately-directed. Presently, there are four scenarios suggested for the formation of LMXBs, three of which include a common envelope phase, and only one which does not involve a supernova.

Accretion-induced Collapse

The first scenario postulates that a white dwarf accretor is able to grow sufficiently via accretion to cross the $1.4M_\odot$ Chandrasekhar limit and collapse to a neutron star (Whelan & Iben 1973, Flannery & van den Heuvel 1975, Canal & Schatzman 1976). With C-O white dwarfs the collapse would most likely be highly explosive but, for O-Ne-Mg types, electron capture on Ne and Mg isotopes may trigger a relatively "quiet" supernova. A major problems for the white dwarf in this scenario is balancing accretion rates against periodic nova-like ejection of surface material and formation of a red-giant envelope: van den Heuvel et al. (1992) argue that only for accretion rates of $1 - 4 \times 10^{-7} M_\odot$ yr^{-1} does nett mass-growth, and hence accretion-induced collapse, occur. One way around these problems is for binary evolution to generate a white dwarf accretor with mass so close to the Chandrasekhar limit that accretion-induced collapse occurs prior to the first nova-

like reaction on its surface: this would require a white dwarf progenitor mass close to the approximately $8M_{\odot}$ lower-limit for neutron star formation.

The Spiral-in Scenario

The term "spiral-in" here refers to a common envelope stage in the evolution of extreme mass ratio binaries into current X-ray binaries with embedded neutron stars or black holes. Such a scenario was originally proposed by Sutantyo (1975) in the context of Her X-1, which comprises an X-ray pulsar and a $2M_{\odot}$ A dwarf companion. Later van den Heuvel (1983) proposed a spiral-in mechanism to expose a helium core with mass greater than $2 - 3M_{\odot}$ from an initially wide binary with extreme mass ratio: subsequent core evolution leads to collapse in a supernova stage, which forms a neutron star or black hole. Embellishments of this scenario may include a second common envelope phase initiated by the neutron star's companion after the supernova, or (de Kool et al. 1987, Romani 1992) inclusion of significant mass loss via stellar winds from high-mass compact star progenitors.

Triple Star Evolution

The later evolutionary stages of a high-mass X-ray binary may result in system comprising a neutron star (or perhaps a black hole) accretor plus a high-mass donor which swells to become a red giant with a few-solar-mass helium core. If P_{orb} at that time is less than about 1 yr, the neutron star dissipates insufficient energy into the resulting common envelope for it to be ejected, eventually causing the neutron star to merge with the helium core and accrete mass from the surrounding envelope and post-merger debris. The resulting quasi-stable *Thorne-Żytkow object* is similar to a red supergiant in structure, except for the central accreting neutron star which is a significant energy source (Thorne & Żytkow 1977). Like supergiants, these objects exhibit strong mass loss by stellar winds, of order $10^{-6} - 10^{-5} M_{\odot}$ yr^{-1}. Eggleton & Verbunt (1986) suggest that if the original high-mass X-ray binary also had a low-mass companion in wide orbit around it, then that third component could be engulfed in the Thorne-Żytkow object's envelope and then spiral-in towards the central neutron star. Subsequently an LXMB would be formed if the wind mass-loss rate from the Thorne-Żytkow object, together with the rate of energy

dissipation into the envelope during spiral-in, was such as to cause the envelope to disappear by the time P_{orb} for the low-mass companion was less than about a day.

Direct Supernova Evolution

A fourth scenario, recently proposed by Kalogera (1998), involves a supernova, but no prior common envelope, stage during LMXB evolution. The model requires that an appropriately-directed kick-velocity is imparted to the neutron star at birth, which both keeps the binary bound and decreases orbital separation. A subsequent study (Kalogera & Webbink 1998) found that, without the fortuitous intervention of natal kick-velocities, *any* normal evolutionary process for the formation of LMXBs with P_{orb} less than about a day via a common envelope and subsequent supernova requires a fully-degenerate neutron star progenitor (e.g., as in accretion-induced collapse). Furthermore, it was found that age, stability constraints and magnetic-braking efficiency largely determine the characteristics of newborn LMXBs.

Bibliography

References

[1] Canal, R., & Schatzman, E. 1976, A&A, 46, 229

[2] D'Antona, F., Mazzitelli, I., & Ritter, H. 1989, A&A, 225, 391

[3] de Kool, M., van den Heuvel, E. P. J., & Pylyser, E. 1987, A&A, 183, 47

[4] de Kool, M. 1990, ApJ, 358, 189

[5] Eggleton, P. P. 1983, ApJ, 268, 368

[6] Eggleton, P. P., & Verbunt, F. 1986, MNRAS, 220, 13

[7] Faulkner, J., Flannery, B. P., & Warner, B. 1972, ApJ 175, L79

[8] Flannery, B. P., & van den Heuvel, E. P. J. 1975, A&A, 39 61

[9] Frank, J., King, A., & Raine, D. 1992, Accretion Power in Astrophysics (Cambridge: Cambridge Univ. Press)

[10] Giannone, P., & Weigert, A. 1967, Z. Astrophys, 67, 41

[11] Kalogera, V. 1998, ApJ, 493, 351

[12] Kalogera, V., & Webbink, R. F. 1998, ApJ, 493, 351

[13] King, A. R., Kolb, U., & Burderi, L. 1996, ApJ, 464, L127

[14] King, A. R., Kolb, U., & Szuszkiewicz, E. 1997, ApJ, 488, 89

[15] King, A. R. 1998, in ASP Conf. Ser. Vol. 137, Wild Stars in the Old West, ed. S. Howell, E. Kuulkers, & C. Woodward (Provo: Brigham Young Univ.), 174

[16] King, A., & Ritter H. 1998, MNRAS, 293, L42

[17] Kippenhahn, R., & Weigert, A. 1967, Z. Astrophys, 65, 251

[18] Kippenhahn, R., & Weigert, A. 1990, Stellar Structure and Evolution (Berlin: Springer-Verlag)

[19] Kruszewski, A. 1966, Adv. Astr. Astrophys., 4, 233

[20] Landau, L., & Lifshitz, E. 1958, The Classical Theory of Fields (Oxford: Pergamon)

[21] Livio, M., & Soker, N. 1988, ApJ, 329, 764

[22] Livio, M. 1994, in Saas-Fee Adv. Course 22, Interacting Binaries, ed. H. Nussbaumer, & A. Orr (Berlin: Springer-Verlag) 135

[23] Lyne, A. G., Anderson, B., & Salter, M. J. 1982, MNRAS, 201, 503

[24] O'Donoghue, D., Kilkenny, D., Chen, A., Stobie, R. S., Koen, M. C., Warner, B., & Lawson, W. A. 1994, MNRAS, 271, 910

[25] Ostriker, J. P. 1976, in IAU Symp. No. 73, Structure and Evolution of Close Binary Systems, ed. P. Eggleton, S. Mitton, & J. Whelan (Dordrecht: Reidel), 206

[26] Paczyński, B. 1971, Ann. Rev. A&A, 9, 183

[27] Paczyński, B. 1976, in IAU Symp. No. 73, Structure and Evolution of Close Binary Systems, ed. P. Eggleton, S. Mitton, & J. Whelan (Dordrecht: Reidel), 75

[28] Paczyński, B. & Sienkiewicz, R. 1981, ApJ, 248, L27

[29] Paczyński, B. 1983, Nature, 304, 421

[30] Paczyński, B. & Sienkiewicz, R. 1983, ApJ, 268, 825

[31] Pylyser, E., & Savonije, G. J. 1988a, A&A, 191, 57

[32] Pylyser, E., & Savonije, G. J. 1988b, A&A, 208, 52

[33] Rappaport, S., Joss, P. C., & Webbink, R. F. 1982, ApJ, 254, 616

[34] Ritter, H. 1986, A&A, 169, 139

[35] Romani, R. W. 1992, ApJ, 399, 621

[36] Savonije, G. J. 1983, Nature, 304, 422

[37] Savonije, G. J., de Kool, M., & van den Heuvel, E. P. J. 1986, A&A, 155, 51

[38] Skumanich, A. 1972, ApJ, 171, 565

[39] Soker, N., & Livio, M. 1989, ApJ, 339, 268

[40] Starrfield, S. 1989 in Classical Novae, ed. M. F. Bode & A. Evans (Chichester: Wiley), 39

[41] Sutantyo, W. 1975, A&A, 41, 47

[42] Taam, R. E., & Bodenheimer, P. 1989, ApJ, 337, 849

[43] Taam, R. E., Flannery, B. P., & Faulkner, J. 1980, ApJ, 239, 1017

[44] Thorne, K. S., & Żytkow, A. N. 1977, ApJ, 212, 832

[45] Tutukov, A., & Yungelson, L. 1996, MNRAS, 280, 1035

[46] van den Heuvel, E. P. J. 1983, in Accretion-driven Stellar X-ray Sources, ed. W. H. G. Lewin & E. P.J. van den Heuvel (Cambridge: Cambridge Univ. Press), 303

[47] van den Heuvel, E. P. J., Bhattacharya, D., Nomoto, K., & Rappaport, S. A. 1992, A&A , 262, 97

[48] van den Heuvel, E. P. J. 1994, in Saas-Fee Adv. Course 22, Interacting Binaries, ed. H. Nussbaumer & A. Orr (Berlin: Springer-Verlag), 263

[49] van Paradijs, J. 1996, ApJ, 464, L139

[50] Verbunt, F., & Zwaan, C. 1981, A&A, 100, L7

[51] Verbunt, F. 1993, Ann. Rev. Astron. Astrophys, 31, 93

[52] Verbunt, F., & van den Heuvel, E. P. J. 1995, in X-ray Binaries, ed. W. H. G. Lewin, J. van Paradijs & E. P. J. van den Heuvel (Cambridge :Cambridge University Press), 457

[53] Warner, B. 1995a, Cataclysmic Variable Stars (Cambridge: Cambridge Univ. Press)

[54] Warner, B. 1995b, Astr. Sp. Sc, 225, 249

[55] Webbink, R. F. 1979, in Proc. IAU Colloq. 53, White Dwarfs and Variable Degenerate Stars, ed. H. M. van Horn & V. Weidemann (New York: Univ. of Rochester), 426

[56] Webbink, R. F., Rappaport, S., & Savonije, G. J. 1983, ApJ, 270, 678

[57] Webbink, R. F. 1984, ApJ, 277, 355

[58] Whelan, J., & Iben, I. 1973, ApJ, 186, 1007

[59] White, N. E., Nagase, F., & Parmar A. N. 1995, in X-ray Binaries, ed. W. H. G. Lewin, J. van Paradijs & E. P. J. van den Heuvel (Cambridge: Cambridge University Press), 1

[60] Whitehurst, R. 1988a, MNRAS, 232, 35

[61] Whitehurst, R. 1988b, MNRAS, 232, 529

[62] Whitehurst, R., & King, A. R. 1991, MNRAS, 249, 25

[63] Wickramasinghe, D.T. 1988, in Polarized Radiation of Circumstellar Origin, ed. G. V. Coyne S.J., A. M. Magalhães, A. F. J. Moffat, R. E. Schulte-Ladbeck, S. Tapia & D. T. Wickramasinghe (Vatican City State: Vatican Observatory), 3

Chapter 3

S-Curves of X-ray Heated Accretion Discs and Black Hole Soft X-ray Transients

Walid El-Khoury[1,†] & Dayal Wickramasinghe[1,*]

[1] The Astrophysical Theory Centre and The Department of Mathematics, Australian National University, ACT, 0200, Australia.

[†] email: walid@maths.anu.edu.au

[*] email: dayal@maths.anu.edu.au

3.1 Introduction

It is now generally accepted that the dwarf nova outbursts in cataclysmic variables (CVs) are triggered by a thermal (or thermal plus tidal) instability in the accretion disc. The characteristics of the light variations exhibited by the different classes of CVs can be explained, at least semi-qualitatively, by differences in the mean mass-transfer rates $\dot{M}$. If, for a given orbital period P_{orb}, $\dot{M}$ is above a critical value $\dot{M}_{crit}(P_{orb})$, the discs are stable and dwarf nova activity is not seen (e.g., nova-like variables), while if $\dot{M}_{tr}$ is somewhat below $\dot{M}_{crit}(P_{orb})$ the discs tends to exhibit dwarf nova outbursts. Some classes of CVs, such as the Z Cam systems, appear to have properties in between these two classes, sometimes showing dwarf nova outbursts and at other times exhibiting stable behaviour. They tend to have mean mass-transfer rates close to the critical value. In very short period CVs, $P_{orb} < 2$ hrs, – e.g., the SU UMa and the ER UMa systems – additional effects occur due to tidal resonances which may also influence the structure of the disc and its outburst properties, as discovered by Whitehurst (1988) (see also Osaki (1997)

for a recent review).

Thermal stability can be discerned from a study of the S-curves which may occur in the relationship between $\log T_{eff}$ — or equivalently $\log \dot{M}$ — and $\log \Sigma$, where T_{eff} and Σ are the effective temperature and surface density respectively. Physically they represent a vertically-averaged heating/cooling balance relationship. Regions of negative slope correspond to thermal instability and those of positive slope to stability. For CV or low-mass X-ray binary (LMXB) discs, $\dot{M}_{crit}$ is identified as the upper critical point of this curve which occurs when hydrogen changes from being mainly neutral to ionised ($T_{eff} = 8000 - 10000$ K) with increase in $\dot{M}$.

In LMXBs, accretion energy is converted more efficiently into high-energy photons than in CVs and, as a result, the effects of X-ray irradiation on the thermal structure of the disc could be significant. It has been suggested recently that discs in LMXBs with black hole (or even neutron star) companions are also subject to instabilities which give rise to brightness variations, but that the instability criterion may be different due to X-ray heating (van Paradijs 1996, King et al. 1996): such LXMBs are termed *soft X-ray transients* (SXTs). In particular, it has been proposed that in the presence of the strong X-ray heating expected in LMXBs, the critical mass-transfer rate above which the discs become stable would be significantly reduced.

Previous studies (Tuchman et al. (1990) and references therein) have already shown that heating could have an important impact on disc structure. However these studies have been restrictive in that radiative transfer has been treated in the diffusion approximation, and specific assumptions have been made which preclude an investigation of the optically-thin and marginally optically-thick discs in a self-consistent manner.

In this paper we construct a simple bi-grey model for the vertical structure of X-ray irradiated discs and investigate the impact of X-ray heating on the disc structure in an attempt to place the above ideas on a firmer footing. Our models are used to construct S-curves for X-ray heated discs and to investigate instability.

3.2 X-ray Heating of Discs — General Considerations

In LMXBs the inner regions of the disc and the accretors surface (if the compact object is a neutron star) can both emit hard X-rays, which can, in principle, affect the disc structure and change the value of $\dot{M}_{crit}$. The maximum effect that X-ray heating can have on a disc can be estimated by the following arguments. For accretion at rate $\dot{M}$ onto a central object, the accretion luminosity is given by

$$L = \eta \dot{M} c^2$$

where $\eta \approx 0.1$ or 0.0001 for a Schwarschild black hole or a white dwarf respectively. The high-energy component of the radiation (the bulk of this luminosity) will originate from the inner regions of the disc, which can be taken to be a point source as a first approximation. Due to the flaring (concavity) of the disc, some of this radiation will be intercepted and reprocessed by the outer regions of the disc. It is also possible that radiation may scatter off a disc corona and impinge on the disc. The X-ray flux, F_X, incident on a unit area of disc at radius R can be parametrised as

$$F_X = \sigma T_X^4 = C \frac{\eta \dot{M} c^2}{4\pi R^2} \tag{3.1}$$

where T_X is an equivalent black body effective temperature for X-ray heating and is given by

$$T_X = 7.1 \times 10^4 \left(\frac{\eta}{0.1}\right)^{1/4} \left(\frac{C}{10^{-2}}\right)^{1/4} \left(\frac{\dot{M}}{10^{18}}\right)^{1/4} \left(\frac{10^{10}}{R}\right)^{1/2}. \tag{3.2}$$

Here σ is the Stefan-Boltzmann constant, C is a parameter which takes into account disc flaring and oblique incidence, inadequacies in the point source approximation, and the possibility of the intensification of flux due to scattering from a disc corona. For the black hole case we have (see Tuchman et al. (1990) and references therein)

$$C = (1 - \beta) \left(\frac{z_0}{R}\right)^2 \left(\frac{d \ln z_0}{d \ln R} - 1\right) \tag{3.3}$$

where β is the X-ray albedo and z_0 is the local disc semi-thickness. From LMXB observations we have $z_0/R \approx 0.2$ and $\beta = 0.9$ (see King et al. (1997) and references

therein) which gives $C \approx 7.8 \times 10^{-4}$ for a black hole. In our calculations we take $C = 5 \times 10^{-4}$. Dubus et al. (1999) use a disc model in which C is parametrised and evaluated self-consistently, but only in an optically-thick disc where the diffusion approximation may be used. The above value can be compared with the flux generated by viscous dissipation in the upper half of the disc, which for large R can be written as (Shakura & Sunyaev 1973)

$$F_V = \sigma T_V^4 = \left(\frac{3}{8\pi}\right)\left(\frac{GM\dot{M}}{R^3}\right) \tag{3.4}$$

where G is the gravitational constant, M is the accretor mass and T_V is the viscous effective temperature given by

$$T_V = 4 \times 10^4 \left(\frac{\dot{M}}{10^{18}}\right)^{1/4} \left(\frac{10^{10}}{R}\right)^{3/4} \left(\frac{M}{10M_\odot}\right)^{1/4} \text{K}. \tag{3.5}$$

Since F_V has a steeper dependence on R than F_X, it follows that the ratio

$$Y_X = \frac{F_X}{F_V} = \frac{T_X^4}{T_V^4} \tag{3.6}$$

can approach or exceed unity at large R.

One can formally define an effective temperature for the irradiated disc through

$$T_{eff} = (T_V^4 + T_X^4)^{0.25} = T_V(1 + Y_X)^{0.25}.$$

King et al. (1996) and van Paradijs (1996) have argued that, for X-ray irradiated discs in the regime where $Y_X >> 1$, the disc's effective temperature is $T_{eff} \approx T_X \approx Y_X^{0.25} T_V$, significantly larger than the value generated by viscous dissipation, and that the onset of thermal stability at a given radius in the high $\dot{M}$ branch (assumed to be when $T_{eff} = 8 \times 10^3 - 10^4$ K) would therefore occur at a smaller value of M_{crit}. However, it is not immediately apparent that the gas in the disc would attain temperatures of the order of T_X, even if the irradiation flux is significant compared to the viscously-generated flux. A minimum requirement is that the *irradiated* disc structure remains optically-thick to X-ray irradiation, and this is not known a priori. Furthermore, detailed calculations are required to investigate if the S-curves preserve the same character as in non-irradiated discs.

3.3 The Model — Assumptions

We present below the main assumptions used here; they are a compromise between accuracy, plausibility and computing time.

- The disc is geometrically thin; i.e., the radial dimension of the accretion disc is much more extended than its vertical dimension. Consequently, we assume that heat transfer in the radial direction is negligible, and the disc is modelled as a collection of independent elemental rings.

- The disc is axially symmetric, with rotational velocity following Kepler's law.

- The self-gravity of the disc is negligible compared with the vertical component of central gravity due to the accretor.

- The accretion disc follows the α-prescription of Shakura & Sunyaev (1973), where local viscous energy generation is proportional to gas pressure.

- When calculating vertical temperature distributions, we assume a grey disc structure in the optical bands, and use Rosseland mean opacities. We believe this is reasonable for the range of parameters considered, but the grey assumption is less accurate in optically-thin discs, particularly for temperatures less than about 5000 K (Mineshige & Wood 1990). Moreover, since there are a large number of calculations performed in each run of the model, computing time is an issue for consideration. Non-grey calculations would be at least an order of magnitude longer, and would not be rewarded by significantly more accurate results (R. Wehrse, private communication).

- Viscously-generated energy is transported by radiation only. Any modelling of convective energy transport would also be very demanding of computing time, and its inclusion in this case is not warranted (R. Wehrse, private communication and J. K. Cannizzo, private communication).

- Gas in the disc is assumed to be in local thermal equilibrium equilibrium (LTE).

3.4 The Model — Analytical Formulation

In developing equations for the vertical structure (z-structure) of a disc ring at radius R, we do not solve the full non-grey problem but instead, adopt a bi-grey approximation which encapsulates its essential features. That is, we treat the radiative transfer in the X-ray band assuming X-ray opacity, with κ_X, σ_e and $\chi_X = \kappa_X + \sigma_e$ as the absorption, scattering and extinction coefficients per unit volume respectively; and in the optical bands we assume corresponding quantities κ_R, σ_e and $\chi = \kappa_R + \sigma_e$ where κ_R is the Rosseland mean opacity. The composition is taken to be solar.

Our grey formulation is somewhat similar to that developed by Wehrse et al. (1994) — see also Shaviv & Wehrse (1986) — for α-disc models, where a grey two-stream approximation is used for the radiation field. For normal angle-of-incidence θ, the frequency-integrated flux, F, and mean intensity, J, are defined in terms of the frequency-integrated intensity I by

$$F = \int_{-1}^{1} I\mu d\mu, \tag{3.7}$$

$$J = \frac{1}{2}\int_{-1}^{1} I d\mu, \tag{3.8}$$

where $\mu = \cos\theta$. Using n-point Gaussian quadrature, these relationships may be approximated by

$$F = 2\pi \sum_{i=1}^{n} a_i \{\mu_i I_i^+ - \mu_i I_i^-\}, \tag{3.9}$$

$$J = \frac{1}{2} \sum_{i=1}^{n} a_i \{I_i^+ - I_i^-\}. \tag{3.10}$$

where the a_i are Gaussian weighting-factors, and the I_i^+ and I_i^- are corresponding frequency-integrated outgoing and incoming intensities respectively. We use the standard two-stream approximation with $n = 1$, $a_1 = 1$ and $\mu_1 = 1/\sqrt{3}$, in which case

$$F = 2\pi\mu_1 (I^+ - I^-), \tag{3.11}$$

$$J = \frac{1}{2}(I^+ + I^-). \tag{3.12}$$

The model in Wehrse et al. (1994) uses a modified version with $\mu_1 = 1$. In Appendix A we confirm that our two-stream approximation correctly converges to the radiative diffusion equation at large optical depth. Nevertheless, the difference in results between the two formulations is second order with respect to other model assumptions.

The corresponding radiative transfer equations are

$$\mu_1 \frac{dI^+}{dz} = -\chi I^+ + \sigma_e J + \kappa_R B, \tag{3.13}$$

$$-\mu_1 \frac{dI^-}{dz} = -\chi I^- + \sigma_e J + \kappa_R B, \tag{3.14}$$

where z is the vertical coordinate measured from the mid-plane of the disc, and the frequency-integrated Planck function

$$B = \int_{-\infty}^{+\infty} B_\nu d\nu = \frac{\sigma T^4}{\pi}. \tag{3.15}$$

Subtracting and adding (3.13) and (3.14), we find the following equations for the z-structure of a disc ring at radius R which relate flux and mean intensity

$$\frac{dF}{dz} = 4\pi\kappa_R(\frac{\sigma T^4}{\pi} - J), \tag{3.16}$$

$$\frac{dJ}{dz} = -\frac{\chi F}{4\pi\mu_1^2}. \tag{3.17}$$

We assume that the disc is irradiated *vertically* by incident X-ray intensity

$$I_0 = f_X I_{std},$$

where $I_{std} = B(10^4)$ and f_X is a scaling parameter.

The transfer problem in the X-ray band is simplified by assuming that the plasma absorbs and scatters X-rays but that $B_X T_{disc} \ll B_{opt} T_{disc}$, where B_{opt} is the Planck's function in the optical band. This assumption is justified provided the characteristic disc temperature T_{disc} is much less than the characteristic temperature of the X-ray irradiation field, which is the case except in the very inner regions of the disc. The equation of transfer in this band can then be solved explicitly to yield

$$\begin{aligned} I_X^+ &= I_0 \exp\left[-(2\tau_{Xc} - \tau_X)\right] \\ I_X^- &= I_0 \exp\left(-\tau_X\right) \end{aligned}$$

which, using the two-stream approximation, gives us the X-ray mean intensity J_X and flux F_X. Here τ_X is the X-ray optical depth which satisfies

$$\frac{d\tau_X}{dz} = -\chi_X. \tag{3.18}$$

Finally, we have a global energy balance equation which equates the excess of emission over absorption in the optical band, to the energy generated by viscous heating and by X-ray heating. Using the standard α-disc value for viscous energy generation, this equation can be written as

$$4\pi\kappa_R(\frac{\sigma T^4}{\pi} - J) = \frac{3}{2}\alpha\Omega_K P_g + \epsilon_X \tag{3.19}$$

where P_g is the gas pressure, Ω_K is the Keplerian velocity and

$$\epsilon_X = 4\pi\kappa_X J_X = 4\pi\kappa_X I_0 \exp(-\tau_X)\{\exp[-2(\tau_{Xc} - \tau_X)] + 1\}$$

Equations (3.19), (3.17), and (3.18), along with the hydrostatic equilibrium equation

$$\frac{dP_g}{dz} = -\Omega_K^2 z\rho + \frac{\chi}{c}F, \tag{3.20}$$

constitute a closed algebraic-differential equation system for a *boundary-value* problem with two eigenvalues: the disc thickness z_0 and the central X-ray optical depth τ_{Xc}. The boundary conditions are as follows: at the surface of the disc, $z = z_0$, we have

$$F(z_0) = \sigma T_{eff}^4$$
$$J(z_0) = \frac{\sigma T_{eff}^4}{2\pi\mu_1}$$
$$P(z_0) = P_0,$$

with

$$\sigma T_{eff}^4 = \sigma T_V^4 + \int_0^{z_0} \epsilon_X dz$$

We choose P_0 such that the maximum surface density $\rho(z_0) \sim 10^{-10}$ g cm^{-3}. At the disc centre, $z = 0$, we have by symmetry

$$F(0) = 0. \tag{3.21}$$

The eigenvalues are calculated iteratively until the system converges to a consistent solution. The thickness z_0 is chosen such that $F(0) = 0$, and τ_{Xc} is chosen such that the solution with the outer boundary condition $F(z_0)$ — which depends on τ_{Xc} — converges to the same value of τ_{Xc} at the disc centre. The adaptive finite-difference code FORTRAN DASSL (Brenan et al. 1989) is used to solve the equations. Although DASSL is presented as an *initial-value* algebraic-differential equation solver, we treat the boundary conditions at z_0 as initial values, and then iteratively solve for the central boundary condition at $z = 0$ using Newton's method. Fig. 3.1 explains the algorithm for the numerical procedure used. In solving the above equations we have searched only for the cool solutions valid in the body of the disc. The hotter coronae which may lie above the disc are not investigated. Nor have we investigated the possibility of X-ray heated hot solutions for the body of the disc, which may occur at low $\dot{M}$. Our structures are in the regime where the ionisation parameter $\xi = 4\pi F_X/n$, for number density of particles n, satisfies $\xi \leq 10^4$ (Tarter et al. 1969).

3.5 Results and Discussion

The central mass M, the accretion rate $\dot{M}$, the nature of the central accreting object (white dwarf, neutron star or black hole), and the viscosity parameter α all play important roles in determining the properties of the accretion disc. In what follows we consider accretion discs around a black hole of mass $M = 10M_\odot$ and apply our results mainly to black hole SXTs. Our findings, however, have a wider applicability.

In this paper we present the results of three series of calculations using the above technique, with the following different assumptions about X-ray heating.

3.5.1 Case (a): X-ray Irradiated Discs

The heating of the disc atmosphere by X-ray irradiation depends strongly on the energy distribution of the incident photons. Depending on the state of the system,

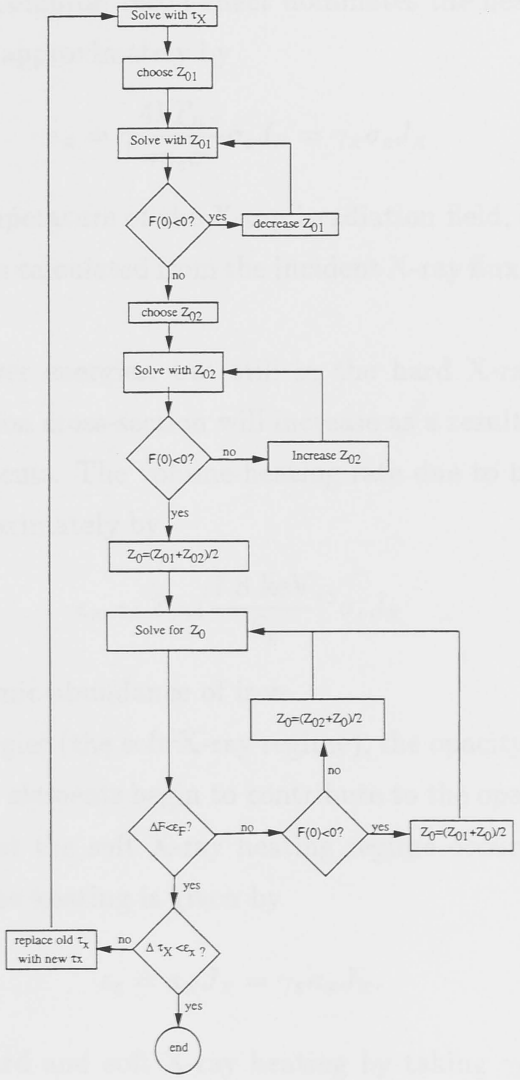

Figure 3.1: This flowchart outlines the algorithm for solving the set of algebraic-differential equations described in the paper. ΔF denotes the absolute value of the difference between the newly-calculated central flux and that from the previous iteration; the parameter ϵ_F therefore determines the desired accuracy of the central flux. Similarly, the parameter ϵ_X is the absolute value of the difference between the newly-calculated τ_X and the old value. The notation $Z_0 = (Z_{01} + Z_0)/2$ means give Z_0 a new value equal to $(Z_{01} + Z_0)/2$, as in Newton's method.

different photon energy distributions are expected, ranging from very soft to hard spectra. If the heating is due mainly to hard X-rays (incident photon energies $E_p \gg 10$ keV) the Compton recoil effect dominates the heating, and the volume heating rate is given approximately by

$$\epsilon_X = \gamma \frac{4kT_{HX}}{m_e c^2} \sigma_e J_X = \gamma_X \sigma_e J_X \tag{3.22}$$

where T_{HX} is the temperature of the X-ray irradiation field, and γ depends on the X-ray spectrum. J_X is calculated from the incident X-ray flux assuming exponential attenuation.

At somewhat lower energies, but still in the hard X-ray regime ($E_p \sim 2 - 10$ keV), the absorption cross-section will increase as a result of photo-electric processes by heavy elements. The volume-heating rate due to true absorption in this regime is given approximately by

$$\epsilon_X \sim Z_{Fe} (\frac{7.8 \text{ keV}}{E_p})^3 \sigma_e J_X \tag{3.23}$$

where Z_{Fe} is the cosmic abundance of iron.

At still lower energies (the soft X-ray regime), the opacity will increase dramatically as other lighter elements begin to contribute to the opacity. In our modelling we have assumed that the soft X-ray heating regime occurs when $\kappa_X \geq \sigma_e$, and that in this regime the heating is given by

$$\epsilon_S = \kappa_X J_X = \gamma_S \kappa_R J_X. \tag{3.24}$$

We consider both hard and soft X-ray heating by taking $\gamma_X = 0.1 - 1$ and $\gamma_S = 1 - 100$ in the above expressions.

We first consider hard X-ray heating, and show in Figs 3.2 and 3.3 the S-curves at radii $R = 10^{10}$ and $R = 10^{11}$ cm respectively for viscosity parameter $\alpha = 0.3$. The three sets of calculations correspond to no X-ray irradiation with $f_X = 0$, moderate X-ray irradiation with $f_X = 1$ ($T_X = 10^4$ K), and high X-ray irradiation with $f_X = 2.9$ ($T_X = 1.3 \times 10^4$ K). All calculations assume $\gamma_X = 1$.

The properties of the S-curves can be understood in terms of simple considerations based on the temperature and density dependence of opacity (e.g.,. Faulkner

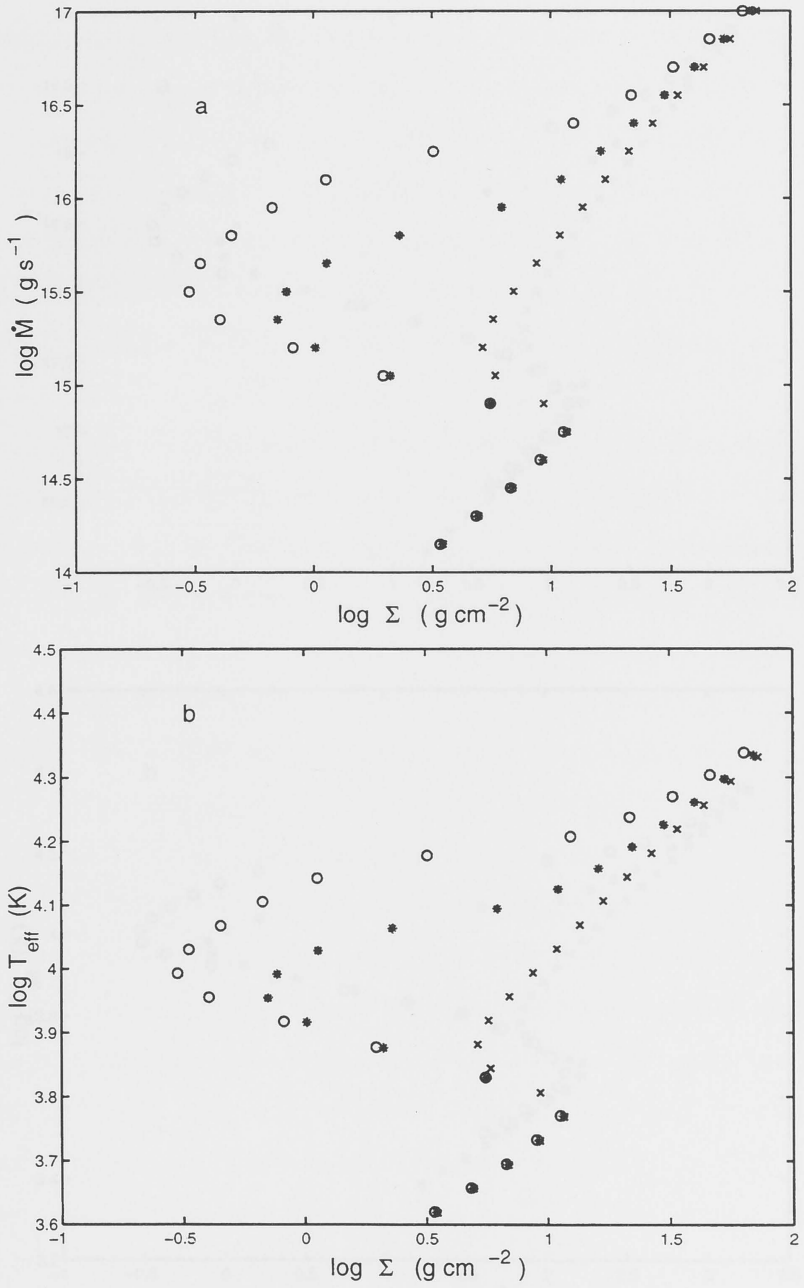

Figure 3.2: S-curves for the hard X-ray irradiated disc ring at $R = 10^{10}$ cm with $\alpha = 0.3$ for three values of the irradiating flux: $f_X = 0$ (crosses) , $f_X = 1.0$ (asterisks) and $f_X = 2.9$ (circles).

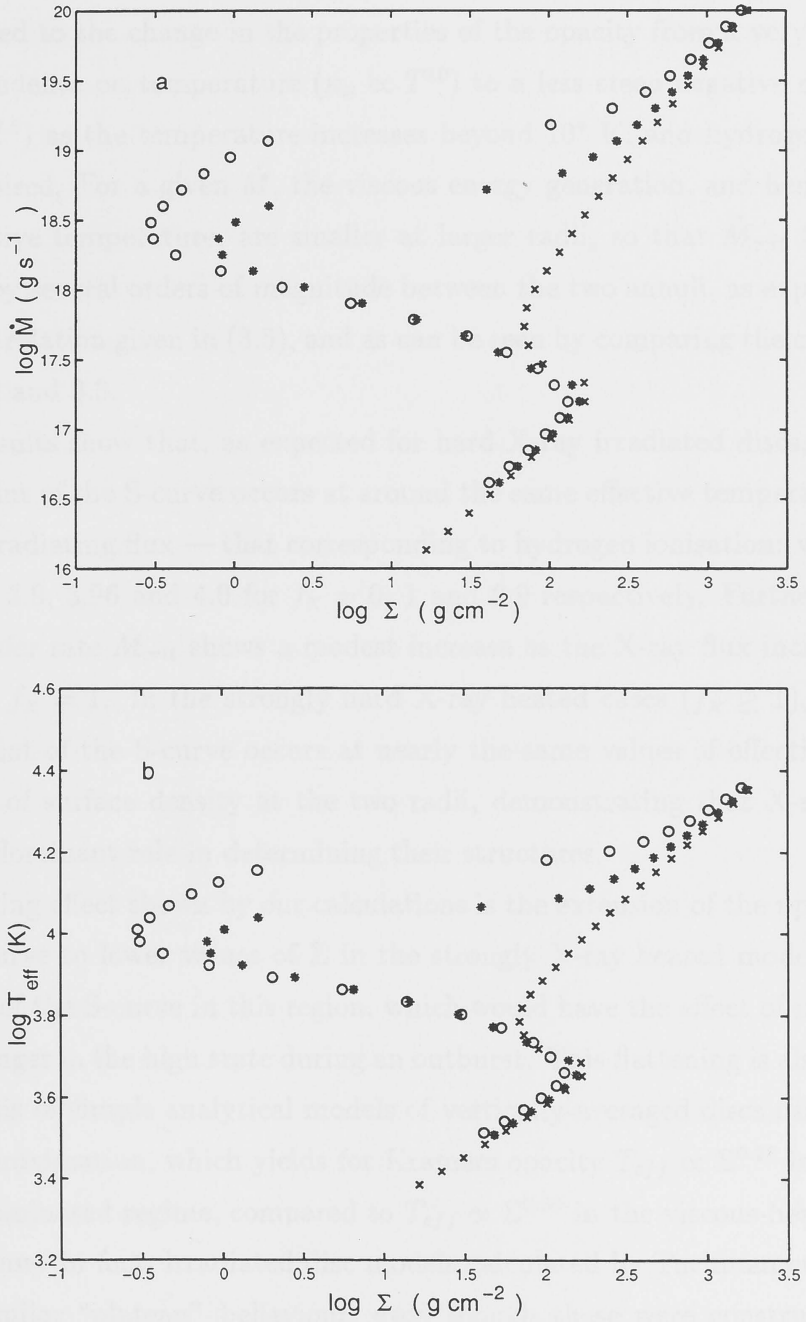

Figure 3.3: S-curves for the hard X-ray irradiated disc ring at $R = 10^{11}$ cm with $\alpha = 0.3$. Point designations as in Fig. 3.2.

et al. 1983). The occurrence of the upper bend in the S-curve corresponding to a critical mass-transfer rate $\dot{M}_{crit}$ (which we refer to as the upper critical point) is attributed to the change in the properties of the opacity from a very steep positive dependence on temperature ($\kappa_R \propto T^{10}$) to a less steep negative dependence ($\kappa_R \propto T^{-2.5}$) as the temperature increases beyond 10^4 K, and hydrogen becomes mainly ionised. For a given $\dot{M}$, the viscous energy generation, and hence the viscous effective temperature, are smaller at larger radii, so that $\dot{M}_{crit}$ for $f_X = 0$ increases by several orders of magnitude between the two annuli, as expected from the simple relation given in (3.5), and as can be seen by comparing the cross-curves in Figs 3.2 and 3.3.

Our results show that, as expected for hard X-ray irradiated discs, the upper critical point of the S-curve occurs at around the same effective temperature whatever the irradiating flux — that corresponding to hydrogen ionisation: we estimate $\log T_{eff} = 3.9$, 3.96 and 4.0 for $f_X = 0$, 1 and 2.9 respectively. Furthermore, the mass-transfer rate $\dot{M}_{crit}$ shows a modest increase as the X-ray flux increases from $f_X = 0$ to $f_X = 1$. In the strongly hard X-ray heated cases ($f_X \geq 1$), the upper critical point of the S-curve occurs at nearly the same values of effective temperature and of surface density at the two radii, demonstrating that X-ray heating plays the dominant role in determining their structures.

A striking effect shown by our calculations is the extension of the upper branch of the S-curve to lower values of Σ in the strongly X-ray heated models, and the flattening of the S-curve in this region, which would have the effect of maintaining the disc longer in the high state during an outburst. This flattening is also expected on the basis of simple analytical models of vertically-averaged discs using the diffusion approximation, which yields for Kramers opacity $T_{eff} \propto \Sigma^{0.28}$ in the X-ray heating dominated regime, compared to $T_{eff} \propto \Sigma^{0.50}$ in the viscous-heating dominated regime. In fact, irradiated disc models calculated by Tuchman et al. (1996) showed similar "plateau" behaviour, even though these were constructed under very different assumptions (see below), indicating that this is a generic property of X-ray heated discs. The sequence of models constructed with a lower value of the viscosity parameter α ($\alpha = 0.03$) shown in Fig. 3.4 also demonstrates simi-

lar effects. In these models, material drifts in at a slower rate due to the lower viscosity, and there is a greater accumulation of material at a given radius. The surface densities are therefore higher at the same mass-transfer rate or effective temperature in comparison to the higher α models.

We show in Fig. 3.5 the Rosseland mean and electron scattering optical depths at $R = 10^{10}$ cm for the models in Fig. 3.2. The electron scattering optical depth is in general significantly less than the Rosseland optical depth in all models except for those near $\dot{M} = 10^{15}$ gs^{-1} and $T_{eff} = 10^4$ K, where both optical depths approach unity. The heating by hard X-rays is therefore expected to have a significant effect on the disc structure precisely in this regime. It should be noted that the total optical depth is reduced relative to the unheated models, which is a general characteristic of all heated models. Likewise, for mass-transfer rates significantly below this value, the scattering optical depth is low ($\tau_X \ll 1$), and so hard X-ray heating has a minimal effect on disc structure. However, since non-LTE effects are not considered, our results in this regime may not be fully justified. Although this may affect the lower branch, we expect that it will have little effect on $\dot{M}_{crit}$.

For significantly larger $\dot{M}$, the disc is optically-thick to electron scattering, and significant X-ray heating is expected. However, viscous heating now exceeds X-ray heating, and again the X-ray flux has a negligible affect on the disc structure.

In Fig. 3.6 we show hard X-ray irradiated and non-irradiated disc structures for $\alpha = 0.3$ and $\dot{M} = 10^{15}$ gs^{-1}, which is in the middle of the instability range. In general, for the range of X-ray fluxes considered, and the range of $\dot{M}$ for which hard X-ray irradiation has an impact, irradiated discs tend to be hotter than their non-irradiated counterparts, and the total optical depth is smaller. The local maximum in the run of density versus optical depth corresponds to the ionisation of hydrogen. This inversion disappears for models with significantly lower and higher mass-transfer rates.

We next investigate the effects of soft X-ray heating by calculating a series of models with $\gamma_S = 100$. The results in Fig. 3.7 show the effect of increasing the incident soft X-ray flux from $f_X = 6.3 \times 10^{-2}$ ($T_X = 5 \times 10^3$ K) through to $f_X = 1$ ($T_X = 10^4$ K) for $\alpha = 0.3$ and $R = 10^{10}$ cm. Because of the larger opacity in the

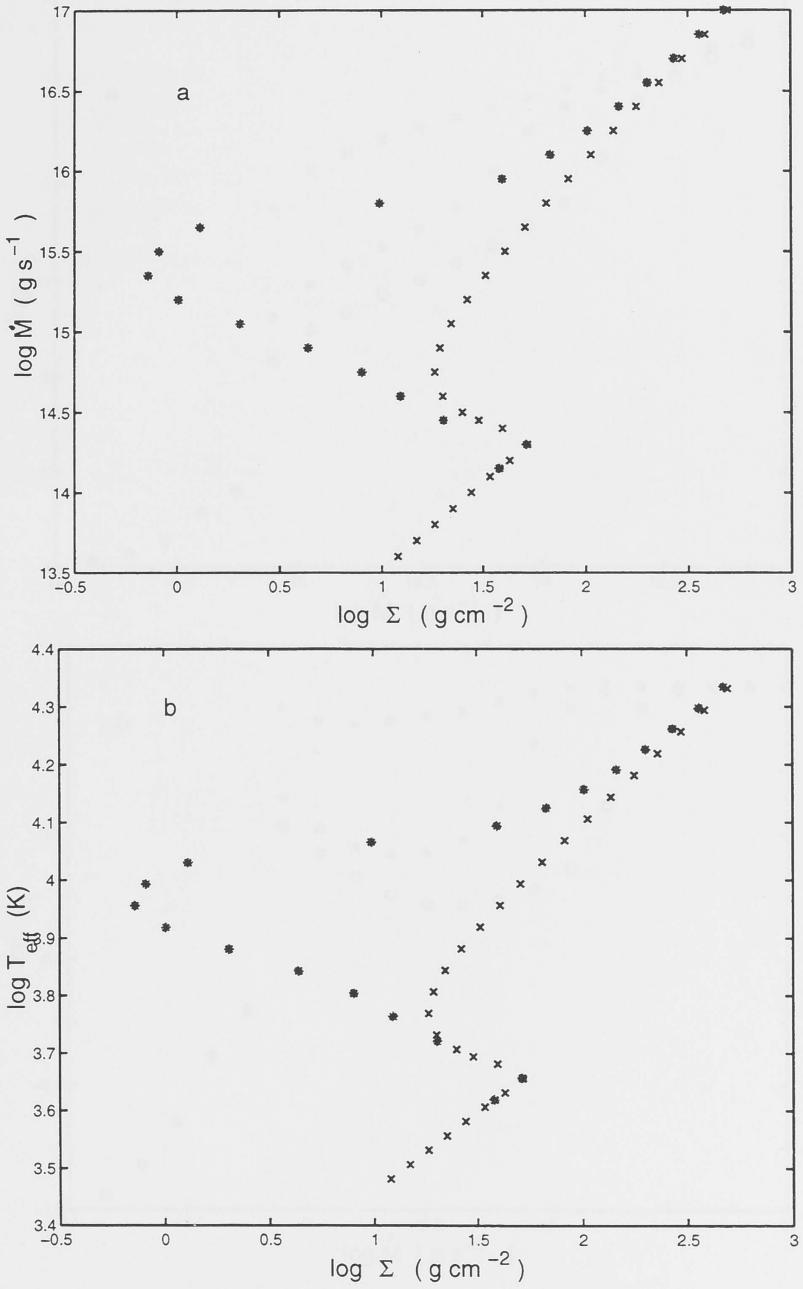

Figure 3.4: S-curves for the disc ring at $R = 10^{10}$ cm as in Fig. 3.2 but with $\alpha = 0.03$. The external flux is fixed at $f_X = 0$ (crosses) and $f_X = 1$ (asterisks).

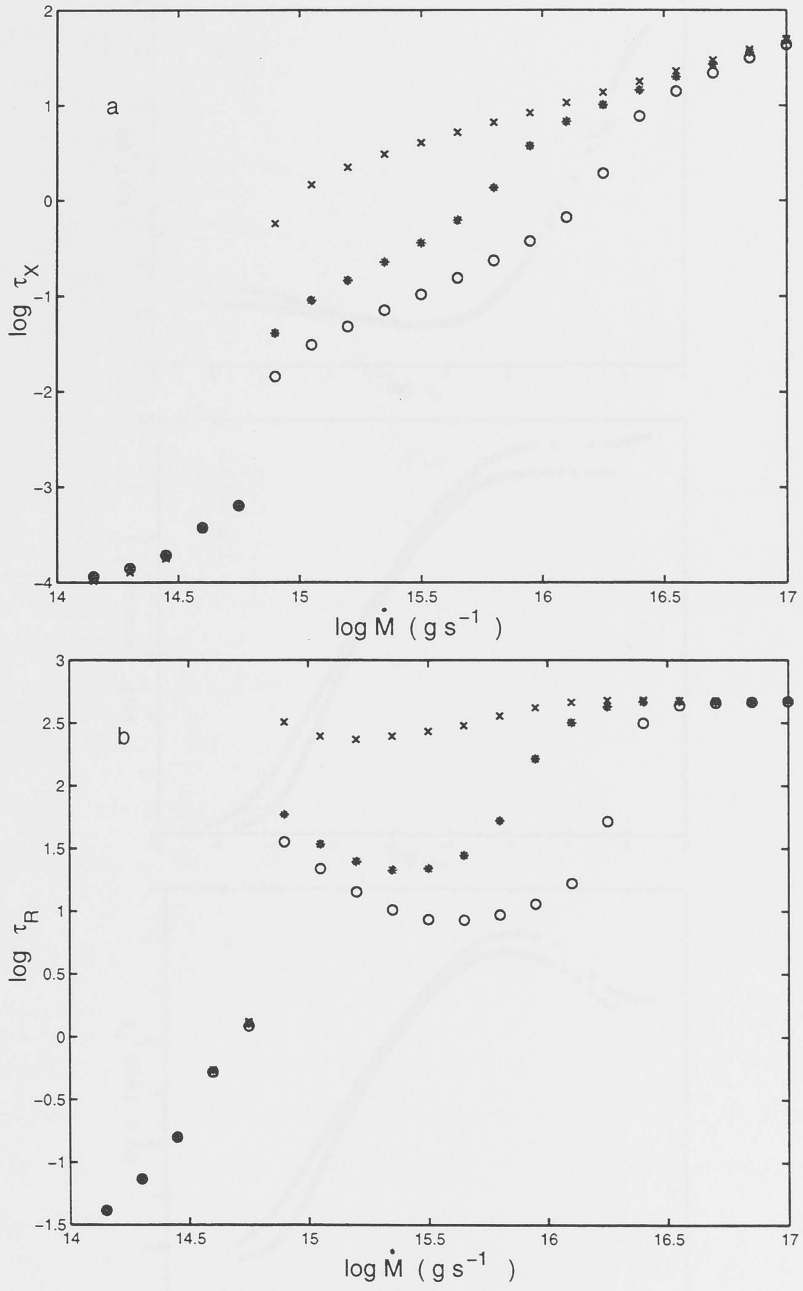

Figure 3.5: Optical depths for the disc ring at $R = 10^{10}$ cm for the same three cases as in Fig. 3.2. Panel (a) : electron scattering optical depth, $\log \tau_X$, versus $\log \dot{M}$. Panel (b) : Rosseland mean optical depth, $\log \tau_R$, versus $\log \dot{M}$.

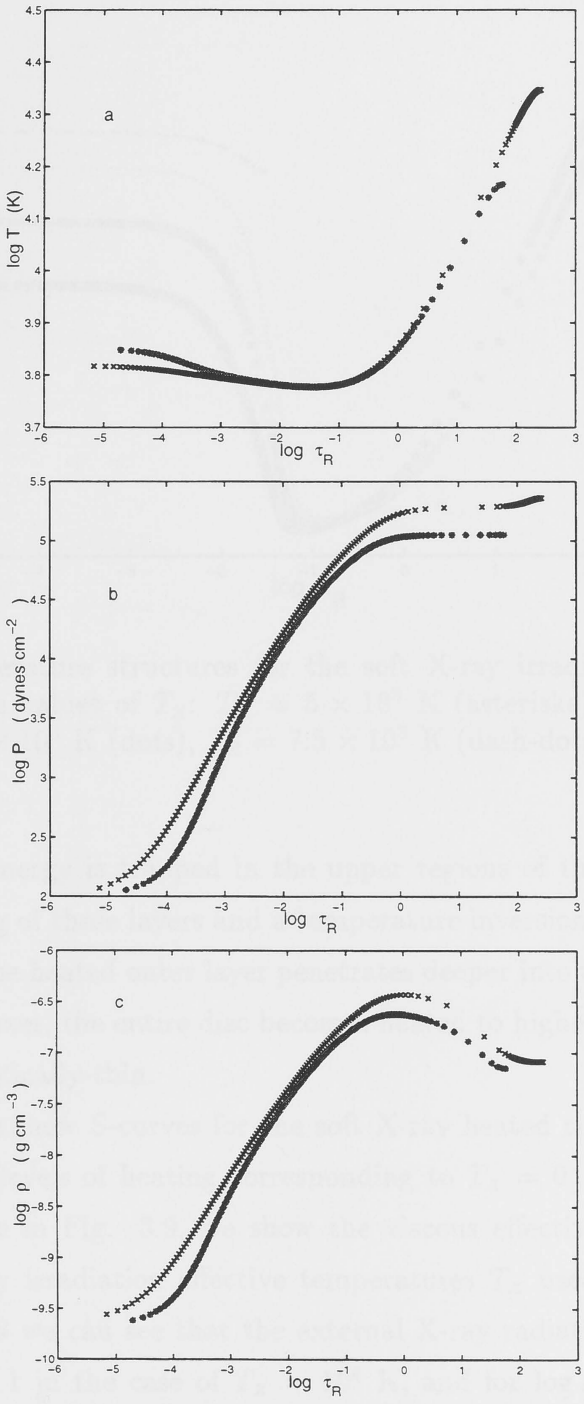

Figure 3.6: Temperature $\log T$, gas pressure $\log P$ and density $\log \rho$ versus $\log \tau_R$ for the disc ring at $R = 10^{10}$ cm with $\log \dot{M}(\mathrm{gs}^{-1}) \approx 15$. Point designations as in Fig. 3.2.

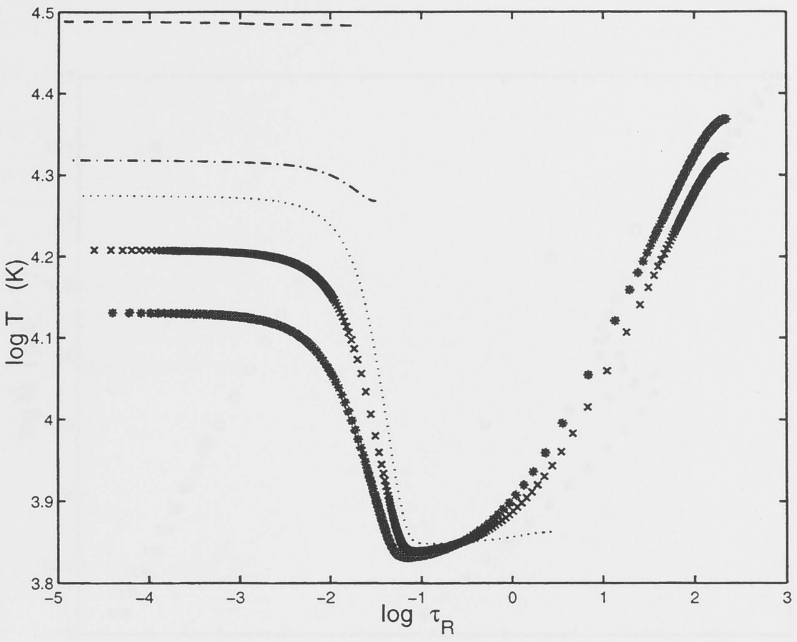

Figure 3.7: Temperature structures for the soft X-ray irradiated ring at $R = 10^{10}$ cm, at various values of T_X: $T_X = 5 \times 10^3$ K (asterisks), $T_X = 6 \times 10^3$ K (crosses), $T_X = 7 \times 10^3$ K (dots), $T_X = 7.5 \times 10^3$ K (dash-dots) and $T_X = 10^4$ K (dashes).

soft X-ray band, energy is trapped in the upper regions of the disc atmosphere, resulting in heating of these layers and a temperature inversion. As the soft X-ray flux is increased, the heated outer layer penetrates deeper into the atmosphere. At sufficiently high fluxes, the entire disc becomes heated to higher temperatures and becomes totally optically-thin.

In Fig. 3.8, we show S-curves for the soft X-ray heated ring $R = 10^{10}$ cm at different constant levels of heating corresponding to $T_X = 0$, 5×10^3 and 10^4 K for $\alpha = 0.3$; while in Fig. 3.9, we show the viscous effective temperature and the constant X-ray irradiation effective temperatures T_X used in Fig. 3.8. By looking at Fig. 3.9 we can see that the external X-ray radiation is dominant for $\log \dot{M}_{crit}(\mathrm{gs}^{-1}) \gtrsim 15.1$ in the case of $T_X = 10^4$ K, and for $\log \dot{M}_{crit}(\mathrm{gs}^{-1}) \gtrsim 14.4$ in the case of $T_X = 5 \times 10^3$ K. When the external radiation becomes dominant, the efficiency of the soft X-ray heating causes a distortion in the S-curve, which could eliminate the unstable branch if the external X-ray flux is high enough, as is the

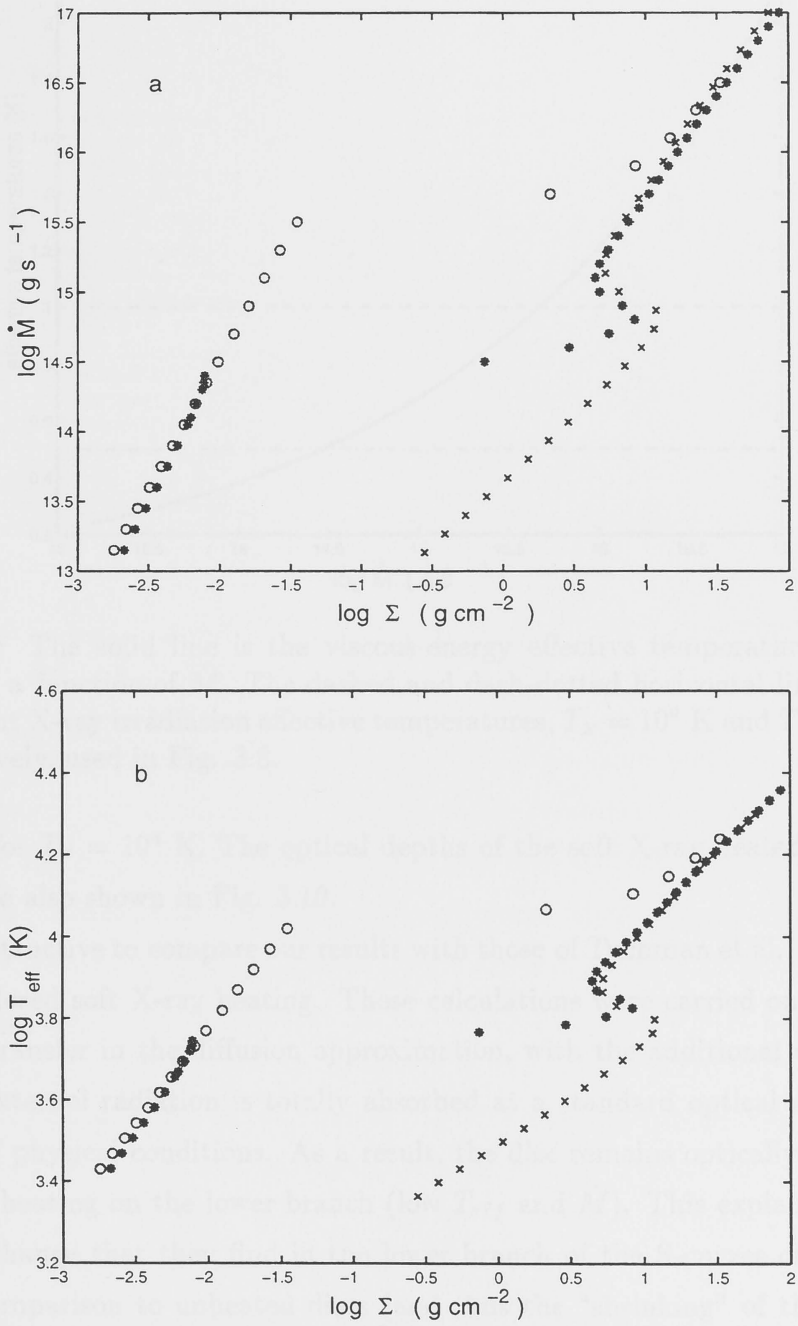

Figure 3.8: S-curves for the soft X-ray irradiated ring at $R = 10$ cm with $\alpha = 0.3$ for the three cases: $f_X = 0$ (crosses) , $f_X = 6.25 \times 10^{-2}$ with $T_X = 5 \times 10^3$ K (asterisks) and $f_X = 1$ with $T_X = 10^4$ K (circles).

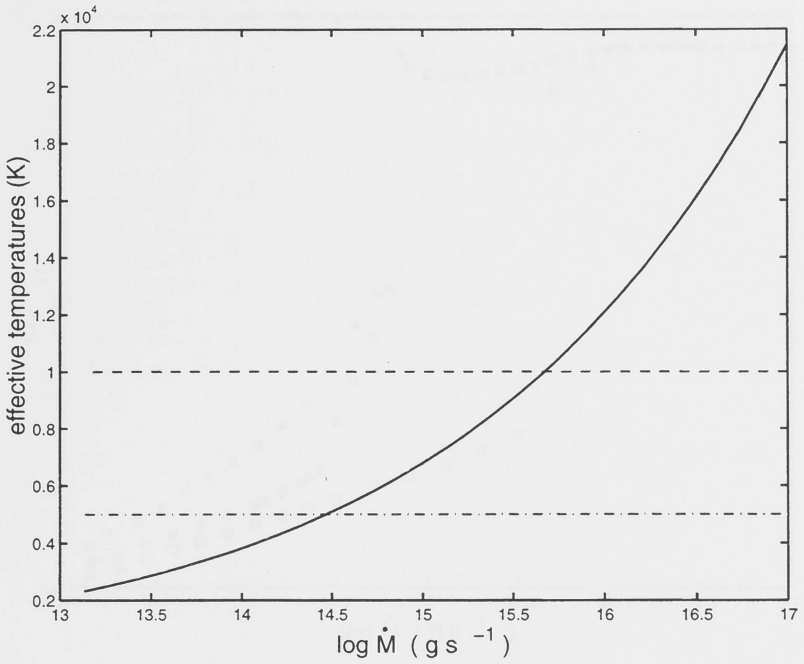

Figure 3.9: The solid line is the viscous-energy effective temperature for $R = 10^{10}$ cm as a function of $\dot{M}$. The dashed and dash-dotted horizontal lines refer to the constant X-ray irradiation effective temperatures, $T_X = 10^4$ K and $T_X = 5 \times 10^3$ K respectively, used in Fig. 3.8.

case here for $T_X = 10^4$ K. The optical depths of the soft X-ray heated models in Fig. 3.8 are also shown in Fig. 3.10.

It is instructive to compare our results with those of Tuchman et al. (1990) who also considered soft X-ray heating. These calculations were carried out assuming radiative transfer in the diffusion approximation, with the additional assumption that the external radiation is totally absorbed at a standard optical depth independent of physical conditions. As a result, the disc remains optically-thick even for strong heating on the lower branch (low T_{eff} and $\dot{M}$). This explains the considerable change that they find in the lower branch of the S-curves of irradiated discs in comparison to unheated discs (and thus the "shrinking" of the unstable branch). However, as we have shown, the temperature inversion caused by soft X-rays, can penetrate deep enough into the disc to affect the entire disc structure, and consequently distort the S-curves through a decrease in surface density in a manner not predicted by the previous calculations.

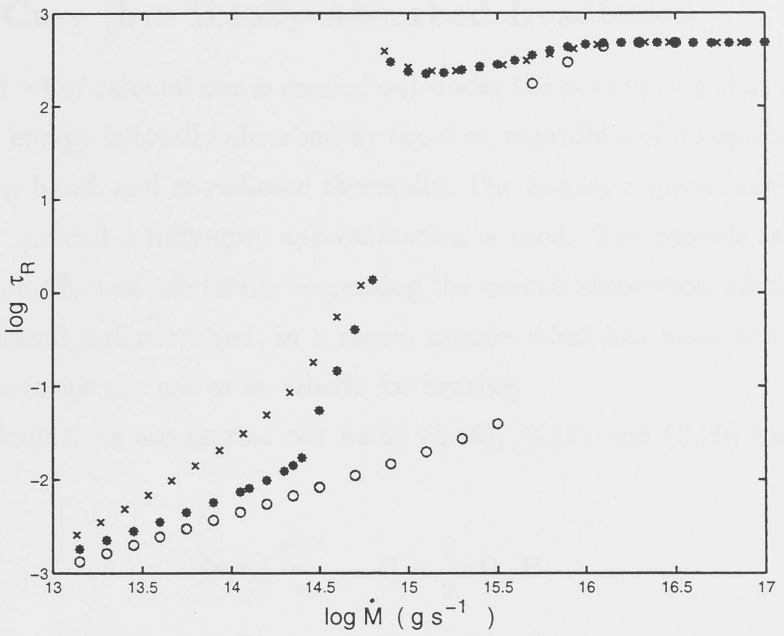

Figure 3.10: Rosseland optical depth, $\log \tau_R$, versus $\log \dot{M}$ for the soft X-ray irradiated disc ring in Fig. 3.8.

We can summarise the effects of heating on S-curves by a constant flux of X-rays as follows. In general, heating influences disc structure only for a small range of $\dot{M}$ when $F_X/F_V > 1$ and the optical depth of the disc to the X-ray flux is high. It is only for values of $\dot{M}$ close to the critical range where instability occurs that hard X-ray heating become important. This arises because the critical points of the S-curve, which delineate the range of unstable $\dot{M}$, occur at surface densities in the range $1 - 100$ g cm^{-2} when hydrogen is becoming significantly ionised, and it is precisely under these circumstances that the electron-scattering optical depth $\tau_X = 0.4\Sigma$ becomes large enough for hard X-ray heating to have an impact on the disc structure. In the case of hard X-ray heating, although the surface density is significantly reduced, the upper critical point happens virtually at the same viscous effective temperature. Soft X-rays, however, are generally more effective in changing the disc structure: the X-rays are much more efficiently absorbed in this wave-band, and as a result the upper critical point could vanish, as we saw earlier.

3.5.2 Case (b): Totally-Absorbed Irradiation

The second set of calculations is carried out under the assumption that all the incident X-ray energy is totally absorbed by the disc, regardless of its optical thickness in the X-ray band, and re-radiated thermally. The bi-grey approximation is abandoned, but instead a fully-grey approximation is used. The models are meant to illustrate the effect of arbitrarily increasing the overall absorption efficiency of the disc to external radiation and, in a sense, mimics what has been adopted in the literature through the use of an albedo for heating.

The calculations are carried out using (3.16), (3.17) and (3.20) but replacing (3.19) by

$$4\pi\kappa_R(\frac{\sigma T^4}{\pi} - J) = \frac{3}{2}\alpha\Omega_K P \tag{3.25}$$

The boundary condition on $F(z_0)$ and $J(z_0)$ are now

$$\begin{aligned} F(z_0) &= (1+Y_X)\sigma T_V^4, \\ J(z_0) &= (1+3Y_X)\sigma T_V^4/2\pi\mu_1 \end{aligned}$$

where Y_X is defined in (3.6).

Implicit in the above formulation is the assumption that absorption and emission occur in the same grey sense. The above approximation is therefore expected to yield realistic results if the incident spectrum is similar to that of the disc (heating mainly by UV and optical photons in the outer regions of the disc). We have also implicitly assumed that the disc is optically-thick. However, it is clear that for models with $\log \dot{M}(\mathrm{gs}^{-1}) \leq 14.8$, the Rosseland optical depth of the disc is less than unity (Fig. 3.5), and that the optical depth is a strong function of mass-transfer rate. The full-absorption models are therefore expected to have limited applicability and have to be interpreted with caution.

The S-curves for the full-absorption models are shown in Fig. 3.11, where we have assumed that the X-ray flux is given by $f_X = 1.0$ at each radius. The assumption of total absorption of incident radiation necessarily implies that there is a lower limit to the effective temperature set by the irradiating flux — the effective temperature cannot decrease below the irradiation effective temperature

T_X. If $f_X = 1.0$ then $T_X = 10^4$ K, and this is seen as a limit to the disc's effective temperature in the calculations illustrated in Fig. 3.11. Interestingly, the lower bend in the S-curve which heralds instability has completely disappeared in this case, and instead there is a monotonic relationship between $\dot{M}$ and surface density Σ. Thus, irradiation can have a damping influence on the development of thermal instability, if the black body temperature associated with this radiation is equal to (or above) 10^4 K.

3.5.3 Case (c): Self-Consistent Illumination

In cases (a) and (b), the irradiation flux is fixed at a given value f_X at all radii. These results may, for instance, be applicable during an outburst, when a given ring may be subject to different levels of X-ray heating not necessarily related to a steady X-ray luminosity originating from the central regions of the disc.

However, in a steady disc, the flux is determined by the luminosity from the central regions of the disc, which in turn depends on the mass-transfer rate. Therefore the flux ratio, Y_X, is the following function of radius

$$Y_X = F_X/F_V = 4.5 \left(\frac{M_\odot}{M}\right) \left(\frac{\eta}{0.1}\right) \left(\frac{\beta}{10^{-2}}\right) \left(\frac{R}{10^{10}}\right) \tag{3.26}$$

Clearly, as already noted, X-ray heating becomes relatively more important in comparison to viscous heating at larger radii, even though the absolute value of the X-ray irradiating flux decreases. The cross-over radius beyond which X-ray heating dominates occurs at $R \approx 2 \times 10^{10}$ cm for a $10 M_\odot$ black hole.

Models for self-consistent illumination corresponding to cases (a) and (b) are constructed as follows. For a given α and C, calculations are carried out for a range of $\dot{M}$ at each radius R by estimating Y_X from (3.26) and using F_V to obtain F_X and hence T_X. These results are then used to construct S-curves and to calculate the mass-transfer rate at the upper critical point which separates stable and unstable discs. One of the uncertainties in these calculations lies in the estimation of β. This quantity will need to be calculated self-consistently using an iterative scheme, since the disc flaring which determines the flux intercepted by the disc is itself a

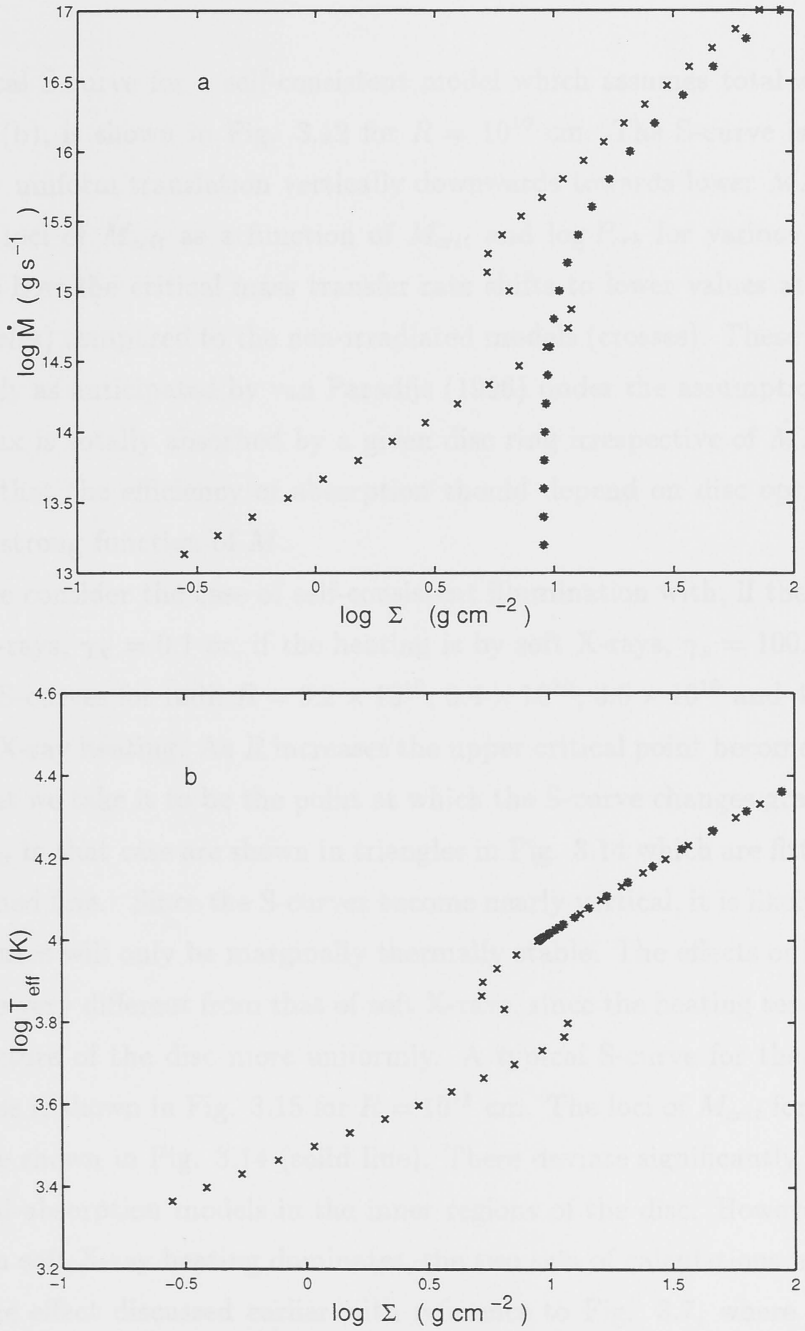

Figure 3.11: S-curves for the X-ray irradiated disc ring at $R = 10^{10}$ cm with $\alpha = 0.3$ for case (b), i.e., a constant X-ray flux of $f_X = 1$ and total absorption. Note the disappearance of the S-curve in panel (a). Point designations as in Fig. 3.2.

function of heating. We have simply adopted a constant value of $C = 5 \times 10^{-4}$ in the present calculations, which is approximately what is expected for standard flaring.

A typical S-curve for a self-consistent model which assumes total absorption, as in case (b), is shown in Fig. 3.12 for $R = 10^{10}$ cm. The S-curve is subjected to a nearly uniform translation vertically downwards towards lower $\dot{M}$. Fig. 3.14 shows the loci of $\dot{M}_{crit}$ as a function of $\dot{M}_{crit}$ and $\log P_{orb}$ for various radii, and we can see how the critical mass transfer rate shifts to lower values at any given radius (circles) compared to the non-irradiated models (crosses). These results are qualitatively as anticipated by van Paradijs (1996) under the assumption that the incident flux is totally absorbed by a given disc ring irrespective of $\dot{M}$. However, it is clear that the efficiency of absorption should depend on disc optical depth, which is a strong function of $\dot{M}$.

Next we consider the case of self-consistent illumination with, if the heating is by hard X-rays, $\gamma_X = 0.1$ or, if the heating is by soft X-rays, $\gamma_S = 100$. Fig. 3.13 shows the S-curves for radii $R = 3.2 \times 10^{10}$, 3.4×10^{10}, 3.6×10^{10} and 4×10^{10} cm with hard X-ray heating. As R increases the upper critical point becomes less well-defined, but we take it to be the point at which the S-curve changes gradient. The loci of $\dot{M}_{crit}$ in that case are shown in triangles in Fig. 3.14 which are fitted linearly by the dashed line. Since the S-curves become nearly vertical, it is likely that such disc structures will only be marginally thermally stable. The effects of hard X-ray heating are very different from that of soft X-rays, since the heating tends to affect the z-structure of the disc more uniformly. A typical S-curve for the soft X-ray heating case is shown in Fig. 3.15 for $R = 10^{11}$ cm. The loci of $\dot{M}_{crit}$ for soft X-ray heating are shown in Fig. 3.14 (solid line). These deviate significantly from those of the total-absorption models in the inner regions of the disc. However, at large radii, when soft X-ray heating dominates, the two sets of calculations merge. This is the same effect discussed earlier with reference to Fig. 3.7, where we showed the transition from an optically-thick to a totally optically-thin z-structure as soft X-ray heating becomes dominant. This transition occurs rather rapidly in Fig. 3.14 and corresponds to the radius $R \sim 3.6 \times 10^{10}$ cm at which the disc structure

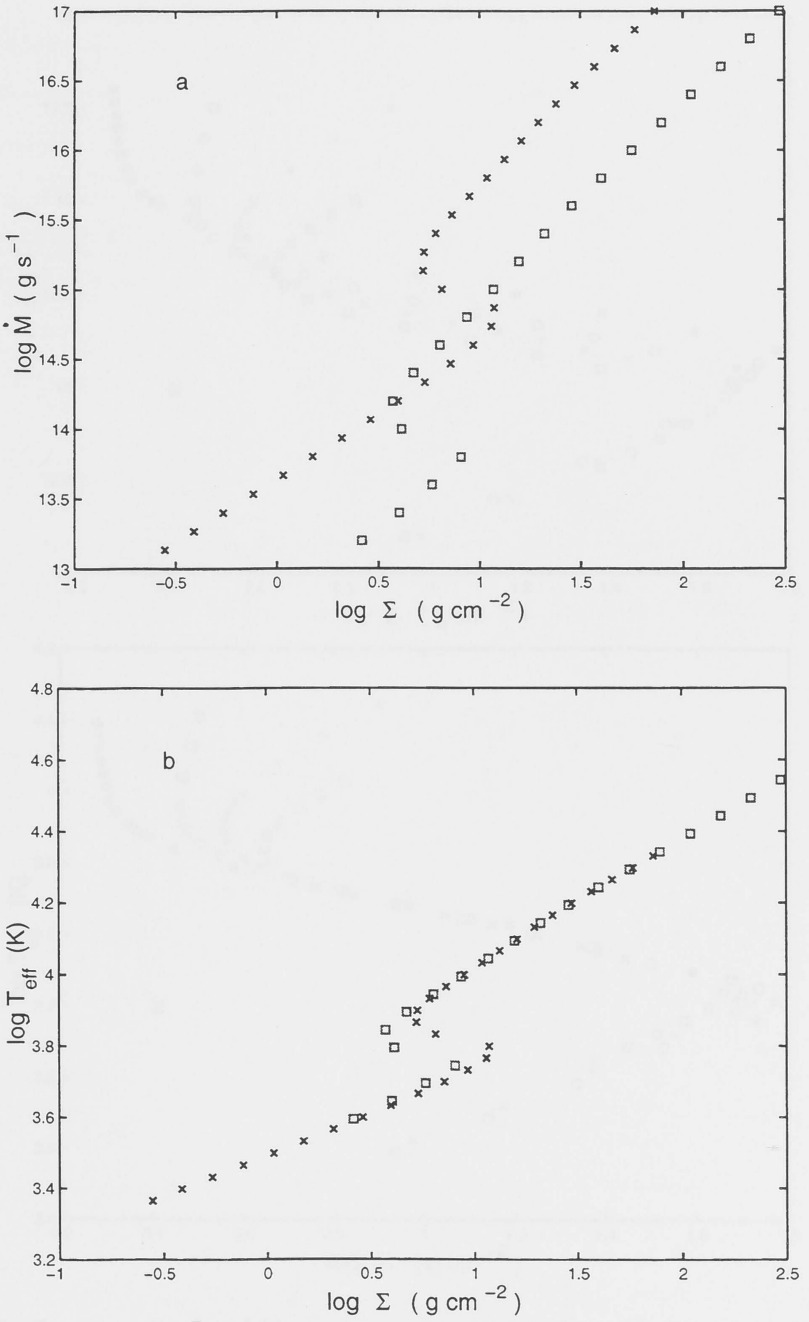

Figure 3.12: S-curves at $R = 10^{10}$ cm for $f_X = 0$ (crosses) and for models with self-consistent illumination and total absorption (squares) as discussed in case (c).

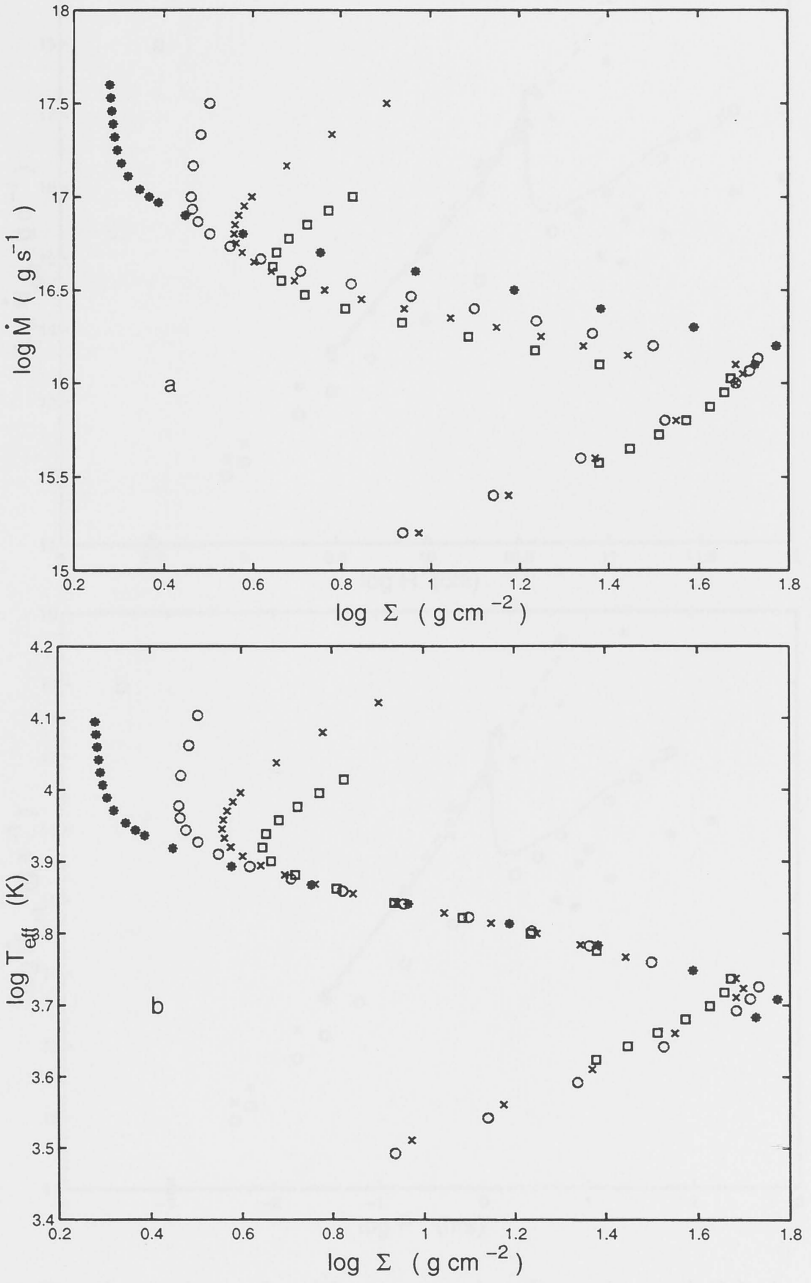

Figure 3.13: S-curves for hard X-ray heated radii for the self-consistent illumination models discussed in case (c): $R = 3.2 \times 10^{10}$ cm (squares), $R = 3.4 \times 10^{10}$ cm (crosses), $R = 3.6 \times 10^{10}$ cm (circles) and $R = 4 \times 10^{10}$ cm (asterisks).

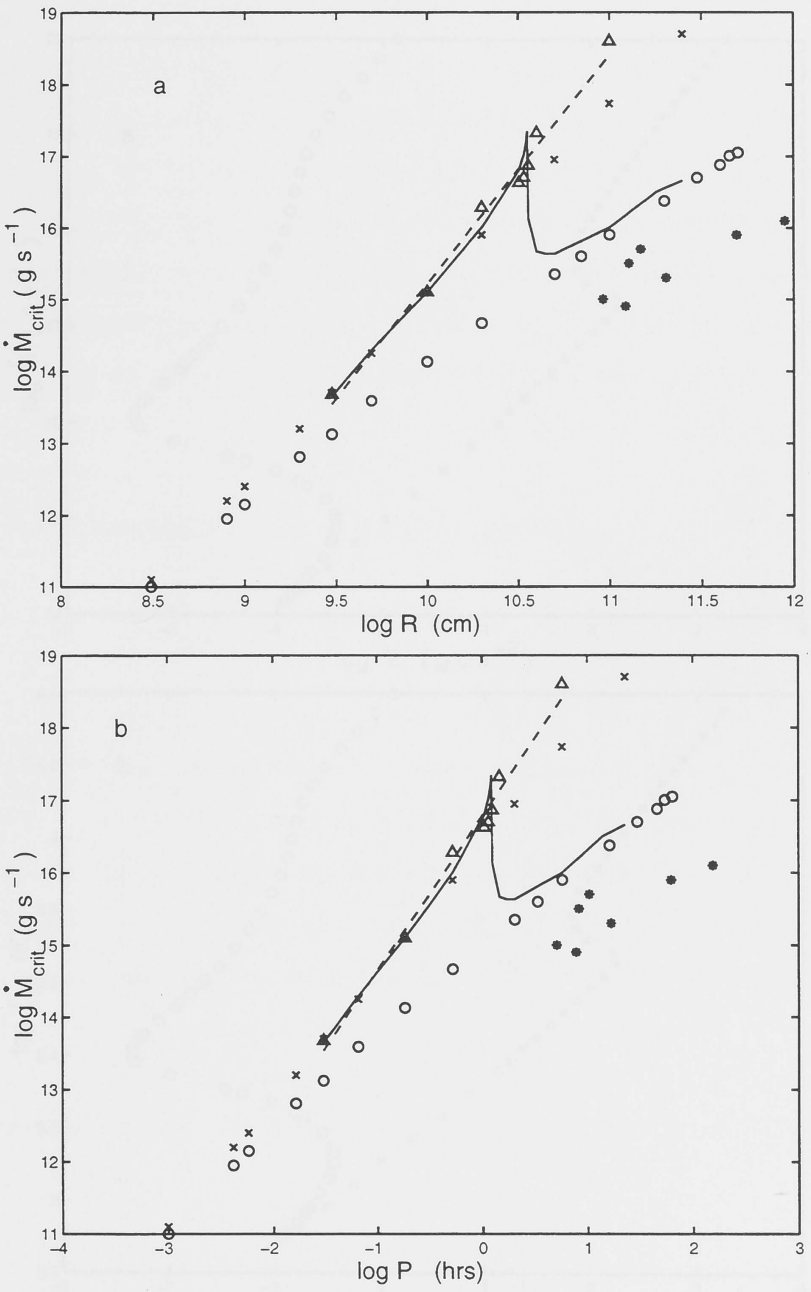

Figure 3.14: Panel (a) shows log $\dot{M}_{crit}$ versus log R, and panel (b) shows log $\dot{M}_{crit}$ versus log P_{orb}. The following cases are considered: no illumination (crosses), self-consistent illumination with total absorption (circles), soft X-ray illumination (solid line) and hard X-ray illumination (triangles linearly fitted by the dashed line). We also include observed black hole SXTs from van Paradijs (1996) (asterisks).

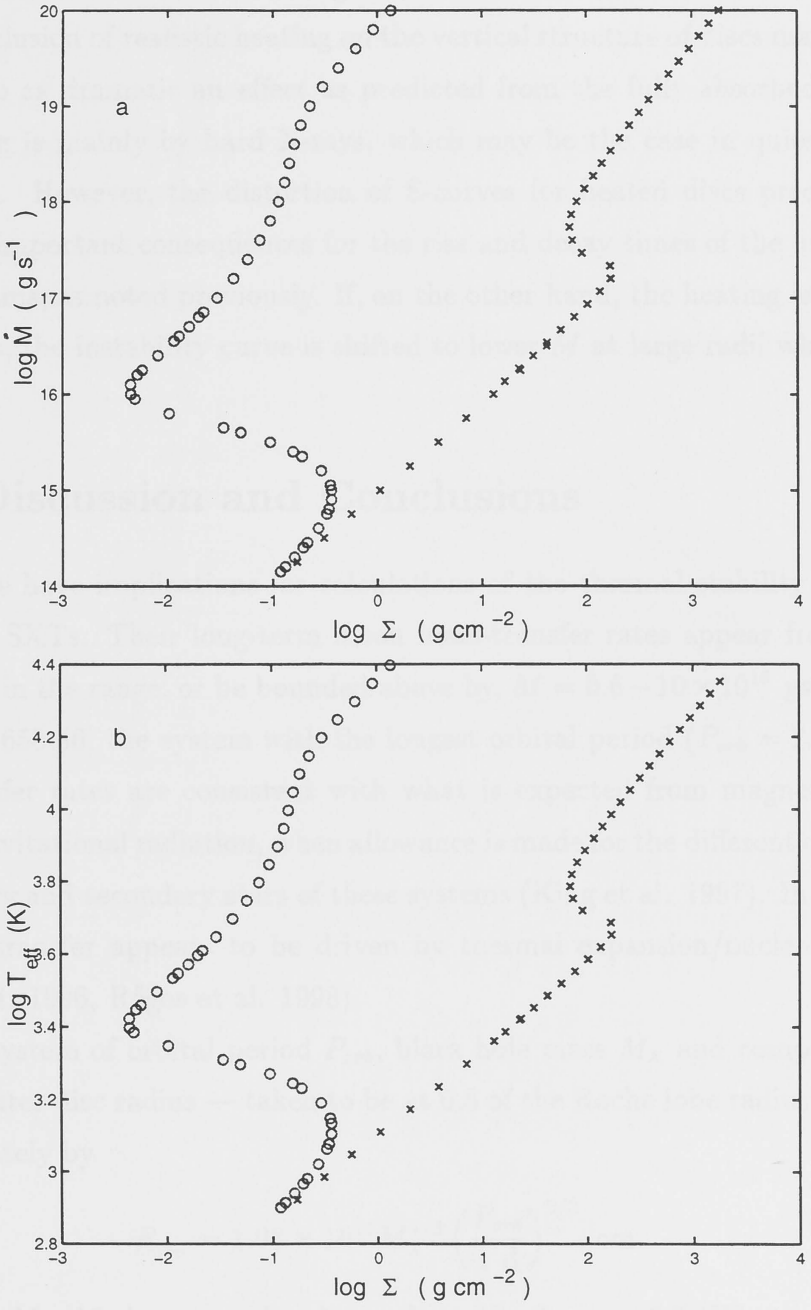

Figure 3.15: S-curves for the soft X-ray heated ring at $R = 10^{11}$ cm, for models with self-consistent illumination as discussed in case (c). The irradiated S-curve (circles) is compared with the non-irradiated S-curve (crosses) from Fig. 3.3.

changes from being optically-thick with a temperature inversion to optically-thin, as is the case for $R = 10^{11}$ cm in Fig. 3.15.

The inclusion of realistic heating on the vertical structure of discs may therefore not lead to as dramatic an effect as predicted from the fully-absorbed models if the heating is mainly by hard X-rays, which may be the case in quiescent black hole SXTs. However, the distortion of S-curves for heated discs predicted here may have important consequences for the rise and decay times of the outbursts in these systems, as noted previously. If, on the other hand, the heating is mainly by soft X-rays, the instability curve is shifted to lower $\dot{M}$ at large radii when heating dominates.

3.6 Discussion and Conclusions

Our results have implications for calculations of the thermal stability of discs in black hole SXTs. Their long-term mean mass-transfer rates appear from present data to lie in the range, or be bounded above by, $\dot{M} = 0.6 - 10 \times 10^{15}$ gs^{-1}. Except for GRO 1655-40, the system with the longest orbital period ($P_{orb} = 2.6$ d), these mass-transfer rates are consistent with what is expected from magnetic braking and/or gravitational radiation, when allowance is made for the different character of the primary and secondary stars of these systems (King et al. 1997). In GRO1655-40, mass transfer appears to be driven by thermal expansion/nuclear evolution (King et al. 1996, Rĕgos et al. 1998).

For a system of orbital period P_{orb}, black hole mass M_X and companion mass M_C, the outer disc radius — taken to be at 0.8 of the Roche lobe radius — is given approximately by

$$R_{out} = 1.08 \times 10^{11} M_X^{1/3} \left(\frac{P_{orb}}{1 \text{ d}} \right)^{2/3} \text{ cm} \qquad (3.27)$$

where $q = M_X/M_C$ is assumed to be in the range $0 < q < 0.3$ (Warner 1995). For the disc instability model to be viable, the critical radius at which instability can first set in will have to be within R_{out}.

We have calculated the outer disc radii for each of the six black hole SXTs listed by van Paradijs (1996), and these are shown plotted against the observed

mean mass-transfer rates in Fig. 3.14 (asterisks). In each case we have assumed a mass of $10M_{\odot}$ for the black hole, which appears typical for black hole SXTs. All observed systems are located to the right of the instability lines for both hard and soft X-ray heated models, and also for the total-absorption models, lending strong support to the disc instability model for the black hole SXTs.

Fig. 3.14b shows on the $\log \dot{M} - \log P_{orb}$ diagram, where we have also plotted the disc instability loci for the total-absorption model, results from the hard and soft X-ray heating models as well as the simple analytical models discussed in the previous section. The theoretical relations delineate the boundaries between stable and unstable discs. Again, we note that all black hole SXTs lie well below the theoretical curves (hard or soft X-ray heating, or total-absorption) and in the region of unstable discs.

The black hole SXTs tend to have hard X-ray spectra during their low states, so we expect that our hard X-ray heated models are more relevant. For GRO 1655-40 the estimated mean mass-transfer rate ($\log \dot{M}(\mathrm{gs}^{-1}) = 15.9$) implies that disc instability will be first triggered at $\log R(\mathrm{cm}) = 11$, which is close to the outer radius of the disc where $\log R_{out}(\mathrm{cm}) = 11.6$. This system is therefore likely to undergo an outside-in outburst (Hameury et al. 1997), although we should emphasise that in the above reasoning, we have assumed that the density in a ring in a quiescent disc can be described by the density of an equivalent steady disc.

We conclude that the effects of X-ray heating will lead to a dramatic shift of the disc instability line of black hole LMXB discs in the $\log \dot{M}_{crit} - \log R$ diagram, particularly if the heating is predominantly by soft X-rays. It is intriguing that all known black hole transients appear to be close to the instability line, and lie only in the region where X-ray heating has a dramatic effect on the disc structure. The effects of heating may not be as dramatic during the quiescent state, when hard X-ray photons are expected to play the dominant heating role. However, our results for heated discs are still consistent with the disc instability model for black hole LMXBs, with the observed black hole LMXBs all lying in the disc instability region.

Our calculations show that the S-curves for X-ray heated discs can be signifi-

cantly distorted relative to those of unheated discs, with the upper branch extending to significantly lower values of surface density. Such discs are therefore expected to exhibit different outburst properties from non-irradiated discs. In particular, X-ray heating may have the consequence of extending the duration of the high state, or changing the rise and decay times of outbursts in the black hole SXTs.

Further development of our model will require the inclusion of more realistic X-ray opacities, and the possibility of convective energy transport (Tuchman et al. 1990). The results of such a study, including an application to neutron star binaries, will be reported in a subsequent communication.

Acknowledgements

We thank Professor Rainer Wehrse for many helpful discussions on various aspects of accretion discs. We are grateful to Dr Stephen Roberts for his valuable help on various computational aspects, and to Michael Burgess for his valuable assistance in preparing this work.

Bibliography

[1] Brenan, K. E., Campbell, S. L., & Petzold, L. R. 1989, Numerical Solution of Initial-Value Problems in Differential-Algebraic Equations (New York: Elsevier)

[2] Dubus, G., Lasota, J. P., Hameury, J. M., & Charles, P. 1999, MNRAS, 303, 139

[3] Faulkner, J., Lin, D. N. C., & Papaloizou, J. C. B. 1983, MNRAS, 205, 359

[4] Hameury, J. M., Lasota, J. P., McClintock, J. E., & Narayan, R. 1997, ApJ, 489, 234

[5] King, A. R., Kolb, U., & Burderi, L. 1996, ApJ, 464, L127

[6] King, A. R., Kolb, U., & Szuszkiewicz, E. 1997, ApJ, 488, 89

[7] Osaki, Y. 1997, in IAU Colloquium 163, Accretion Phenomena and Related Outflows, ed. D. T. Wickramasinghe, L. Ferrario & G. V. Bicknell (Provo: Brigham Young Univ.), 269

[8] Rĕgos, E., Tout, C., & Wickramasinghe, D. T. 1998, ApJ, 509, 362

[9] Shakura, N. I., & Sunyaev, R. 1973, A&A, 24, 337

[10] Shaviv, G., & Wehrse, R. 1986, A&A, 159, L5

[11] Tarter, C. B., Tucker, W., & Salpeter, E. E. 1969, ApJ, 156, 943

[12] Tuchman, Y., Mineshige, S., & Wheeler, J. C. 1990, ApJ, 359, 164

[13] van Paradijs, J. 1996, ApJ, 464, L139

[14] Warner, B. 1995, Cataclysmic Variable Stars (Cambridge: Cambridge Univ. Press)

[15] Wehrse, R., Baschek, B., & Shaviv, G. 1994, in ASP Conf. Ser. Vol. 56, Interacting Binary Stars, ed. A. W. Shafter (Provo: Brigham Young Univ.), 35

[16] Whitehurst, R. 1988, MNRAS, 232, 187

Chapter 4

Accretion Disc Models for AM Canum Venaticorum Systems

Walid El-Khoury[1,†] & Dayal Wickramasinghe[1,*]

[1] The Astrophysical Theory Centre and The Department of Mathematics, Australian National University, ACT, 0200, Australia.

[†] email: walid@maths.anu.edu.au

[*] email: dayal@maths.anu.edu.au

4.1 Introduction

AM CVn systems are puzzling variable stars with hydrogen-deficient spectra and ultrashort period photometric variations in the range $1000 - 3000$ s. Only six have been observed to date. It is currently believed that they are interacting white dwarf binary (IWDB) systems (Faulkner et al. 1972) in which a low-mass white dwarf secondary of mass $M_2 \sim 0.04 M_\odot$ fills it Roche lobe and transfers helium-rich gas to a white dwarf primary, around which a hydrogen-deficient accretion disc is formed. They are the white dwarf counterparts of the better studied neutron star binary systems, and are an interesting but little understood end-product of close binary evolution.

The original motivation behind the IWDB model was to explain a peculiar object, HZ 29 (later designated AM Cangum Venaticorum, or AM CVn), following observations by Malmquist (1936) and Humason & Zwicky (1947). Greenstein & Mathews (1957) had classified HZ 29 as a DB white dwarf since it was hydrogen deficient, exhibiting only strong HeI absorption lines. Later observations suggested a

quasi-stellar object (Burbidge et al. 1967) or a hot star (Wampler 1967). However, the discovery of periodic variability ($\sim$ 17 min) by Smak (1967) suggested a binary system and, after discovering flickering in the high speed photometry, Warner & Robinson (1972) suggested that AM CVn was a close binary in mass-transfer mode.

More objects with similar characteristics were identified: G61-29 (GP COM) was thought by Burbidge & Strittmatter (1971) to be an isolated white dwarf, but later photometry showed flickering activity, suggestive of a binary system (Warner 1972). PG1346+082, later designated CR Bootis, or CR Boo (Nather 1985), and V803 Cen were other objects showing similar characteristics (O'Donoghue et al. 1987). CP Eri was found by Howell et al. (1991) to be a short-period photometric variable of the AM CVn type. The latest object exhibiting AM CVn class characteristics is EC15330-1403, discovered by O'Donoghue et al. (1994).

Some class members exhibit high and low states in their optical flux, which is also strongly suggestive of a mass-transferring close binary, while others are more stable. The characteristics of this long-term variability are reminiscent of what is seen in cataclysmic variables of different sub-types — dwarf novae, nova-likes, SU UMa etc. — where a combination of thermal and tidal disc instabilities appear to play the major role in explaining the long-term variability. A similar interpretation may be possible for AM CVn systems (Warner 1995). AM CVn and EC153330 seem to be in a permanent high state, showing broad and shallow absorption lines presumably originating from a stable high mass-transfer rate $\dot{M}$ and optically-thick accretion disc — similar to nova-like variables and Z Cam systems. GP Com is the only member with a stable low state, and exhibits an emission line spectrum indicative of optically-thinner discs with lower $\dot{M}$. The other three members — CR Boo, V803 Cen and CP Eri — alternate between high and low states, with their spectra showing absorption lines in the former case, and continuous or weak emission lines in the latter case. Such behaviour is expected if $\dot{M}$ is in an intermediate range where the disc becomes thermally unstable — as in dwarf novae. Over and above the thermal instabilities, the discs in AM CVn stars are also expected to be tidally-unstable by virtue of their low donor-to-accretor mass ratio $q = M_2/M_1$. Thus it has been suggested that AM CVn may be in a permanent superoutburst

state exhibiting a superhump period that is slightly larger than the orbital period, making it similar to the high mass-transfer rate SU UMa variables (Osaki 1996).

Our main aims here are to investigate the viability of a disc-instability explanation for some observed behaviour in these systems, and to constrain their parameters by modelling the spectra expected from helium-rich accretion discs and then fitting the results to observed spectra. The paper is arranged as follows. In Section 4.2 we outline the current theoretical and observational status of AM CVn and CR Boo. Section 4.3 presents the equations used to calculate the vertical structures and emergent flux of accretion discs, describing both modelling techniques and assumptions. Numerical results for disc structures and line profiles are presented in Section 4.4, together with spectral-fitting results for AM CVn and CR Boo. Finally, in Section 4.5 results are discussed, and conclusions drawn, in relation to disc instability models and independent estimates of binary masses.

4.2 Observations

This Section summarises relevant observational data on, and theoretical speculation about, AM CVn and CR Boo. We identify the sources of orbital and spectral data that are subsequently used in in the paper.

4.2.1 AM CVn

AM CVn, the prototype, was discovered as a blue object with a peculiar spectrum exhibiting strong but shallow HeI lines mainly in absorption, but with no evidence of hydrogen lines. A late stage of stellar evolution was thus indicated, but an early idea that AM CVn was a single DB type white dwarf (Greenstein & Mathews 1957) was soon dismissed after the discovery of photometric variability with a period of 1051 s. This short photometric period, and evidence of flickering in the light curve, soon led to the realisation that AM CVn was a semi-detached binary system comprising two evolved stars in the process of mass transfer.

Subsequent observations of AM CVn have shown the presence of multiple periodicities (Patterson et al. 1992). The 1051 s period is far from stable, changing erratically from year-to-year, making it a poor candidate for the orbital period of

the system. Patterson et al. (1992) suggested that this was the period of a permanent superhump due to a precessing disc, which is consistent with the low mass ratio indicated for this system. A second more coherent period at 1028.7325 s $\pm$ 0.0004 is also seen in this system, but it sometimes changes to a period of 1011 s. Harvey et al. (1998) proposed the 1028.7325 s period as the actual orbital period of the system. This identification builds on the wobbling-disc theory, in which disc wobbling causes the radial position of the disc's bright spot — where the matter stream from the secondary impacts the disc — to sometimes vary, leading to the apparent change in period from 1028 to 1011 s. Although the periods show complex behaviour, the disc in the system appears to be stable in the long-term, with no reports of large changes in the mean apparent magnitude. Indeed it seems that AM CVn is a system with a disc in a permanent high state, and most likely in permanent superoutburst.

In what follows we take 1028.7325 s as the orbital period P_{orb}. We use as our basic source of spectral data the phase-averaged optical spectrum published by Patterson et al. (1993) — hereafter PHS — which shows characteristic features such as the shape of the continuum, line widths and the double-peaked feature of the lines. From the lack of radial velocity variations in the spectrum of AM CVn, PHS deduced that the radial velocity amplitude of the primary $K_1 < 50$ km/s.

4.2.2 CR Bootis

CR Boo is one of the three known unstable AM CVn systems, and exhibits variations in mean apparent magnitude strongly reminiscent of those caused by thermal disc instabilities in dwarf novae.

Extensive photometric analysis — Patterson et al. (1997) and references therein — led to the current belief that its orbital period $P_{orb} = 1471$ s, and that a 1490 s variation is a good candidate for a superhump period which seems to stabilise at 1487.29 s $\pm$ 0.02 after $300 - 600$ orbits.

For our purposes, we assume $P_{orb} = 1471$ s and adopt a spectrum for CR Boo in its high state kindly provided to us by J. Patterson.

4.3 The Model

This Section sets out the analytical and computational basis for our modelling of the vertical structure and emergent spectra of accretion discs. Assumptions made about system parameters are discussed, as are techniques used to fit observational and modelled spectra. Thermal instability processes in accretion discs are also briefly reviewed.

4.3.1 Accretion Disc Structure

We assume an axisymmetric disc — extending from inner radius R_{in} to outer radius R_{out} — around a central accretor, and use the geometrically-thin approximation with α-prescription for viscosity (Shakura & Sunyaev 1973) to describe the disc structure. Under these assumptions radial pressure gradients are negligible, and angular velocity is effectively the Keplerian value. In systems with extreme mass ratios, tidal effects due to the companion star will distort outer regions of the disc beyond the 3-1 resonance radius. While these distortions may be important in calculating and interpreting phase-dependent line spectra, we neglect them here as we model only phase-averaged spectra.

For mass-transfer at rate $\dot{M}$ through a thin accretion disc around a primary with negligible rotation, the effective temperature T_{eff} at disc radius R is independent of viscosity parameter α and given by (Frank et al. 1992)

$$T_{eff}^4 = \frac{3}{8\pi\sigma}\left(\frac{GM_1\dot{M}}{R^3}\right)\left\{1-\left(\frac{R_1}{R}\right)^{1/2}\right\}, \tag{4.1}$$

where σ and G are the Stefan-Boltzmann and gravitational constants respectively. Note that the radius R_1 of the white dwarf may be related to its mass M_1 and the Chandrasekhar limiting mass M_{ch} by (Nauenberg 1972)

$$R_1 = 7.79\times10^8\left\{\left(\frac{M_1}{M_{ch}}\right)^{-2/3}-\left(\frac{M_1}{M_{ch}}\right)^{2/3}\right\}^{1/2}, \tag{4.2}$$

and that T_{eff} may be expressed as

$$T_{eff} = 7.837\times10^4\left(\frac{M_1}{M_\odot}\right)^{1/2}\left(\frac{\dot{M}}{10^{17}}\right)^{1/4}\left(\frac{R}{R_1}\right)^{-7/8}\left\{\left(\frac{R}{R_1}\right)^{1/2}-1\right\}^{1/4}\ \mathrm{K}, \tag{4.3}$$

where $\dot{M}$ is measured in gs^{-1} and we have used a simplified version of (4.2)

$$\frac{R_1}{R_\odot} = 0.013 \left(\frac{M_1}{M_\odot} \right)^{-1/3}. \tag{4.4}$$

Typically for AM CVn stars, T_{eff} falls from $T_{in} = 5 \times 10^4$K to $T_{out} = 10^4$K as R increases from R_{in} to R_{out}.

We calculate the radial and vertical structure of an accretion disc — ignoring convection — as follows. We first divide the disc into a number of elemental rings of width δR: the choice of this number, as well as of R_{in} and R_{out}, will be discussed below. For each ring, radiative transfer in the vertical direction z is treated in the two-stream grey approximation, using a formulation similar to that in Wehrse et al. (1994) — see also Shaviv & Wehrse (1986). They assume the two streams of radiation to travel normal to the disc, but we assume they travel at angle $\theta = \cos^{-1}(1/\sqrt{3})$ to the normal, which means we may use conventional Gaussian quadrature to approximate the flux integral. We stress that variations in disc structures between the two formulations are minimal.

The frequency-integrated flux, F, and mean intensity, J, are defined in terms of the frequency-integrated intensity I by

$$F = \int_{-1}^{1} I \mu d\mu, \tag{4.5}$$

$$J = \frac{1}{2} \int_{-1}^{1} I d\mu, \tag{4.6}$$

where $\mu = \cos\theta$. Using n-point Gaussian quadrature with weighting-factors a_i and corresponding outgoing and incoming intensities I_i^+ and I_i^- respectively, these expressions become

$$F = 2\pi \sum_{i=1}^{n} a_i \{ \mu_i I_i^+ - \mu_i I_i^- \}, \tag{4.7}$$

$$J = \frac{1}{2} \sum_{i=1}^{n} a_i \{ I_i^+ - I_i^- \}. \tag{4.8}$$

For the two-stream approximation $n = 1$, $a_1 = 1$ and $\mu_1 = 1/\sqrt{3}$, in which case

$$F = 2\pi\mu_1 (I^+ - I^-), \tag{4.9}$$

$$J = \frac{1}{2}(I^+ + I^-). \tag{4.10}$$

With no irradiation, the model equations for an elemental ring at disc radius R with local gas density ρ become

$$\frac{dF}{dz} = 4\pi\kappa_R(\frac{\sigma T^4}{\pi} - J), \tag{4.11}$$

$$\frac{dJ}{dz} = -\frac{\chi F}{4\pi\mu_1^2}, \tag{4.12}$$

$$\frac{dP_g}{dz} = -\Omega_K^2 z\rho + \frac{\chi}{c}F, \tag{4.13}$$

$$4\pi\kappa_R(\frac{\sigma T^4}{\pi} - J) = \frac{3}{2}\alpha\Omega_K P_g, \tag{4.14}$$

which give the grey flux F, mean intensity J, gas pressure P_g and temperature T as functions of z: κ_R and χ are Rosseland mean absorption and extinction coefficients respectively, and Ω_K is the angular velocity at disc radius R given by

$$\Omega_K = \sqrt{\frac{GM_1}{R^3}} = 0.423\sqrt{\frac{m_1}{r^3}}\ \mathrm{s}^{-1}, \tag{4.15}$$

which again assumes the white dwarf mass-radius relationship (4.4).

The above constitute a closed algebraic-differential equation system for a *boundary-value* problem with eigenvalue z_0, the semi-thickness of the disc. Boundary conditions at the surface of the disc, $z = z_0$, are

$$F(z_0) = \sigma T_{eff}^4,$$
$$J(z_0) = \frac{\sigma T_{eff}^4}{4\pi\mu_1},$$
$$P_g(z_0) = P_0,$$

with P_0 chosen such that the line formation region is fully within the calculated structure (e.g., $\log P_0 \sim -3$) and $T(z_0)$ is determined via the energy-balance equation (4.14). From symmetry, the boundary condition at the disc mid-plane, $z = 0$, is

$$F(0) = 0. \tag{4.16}$$

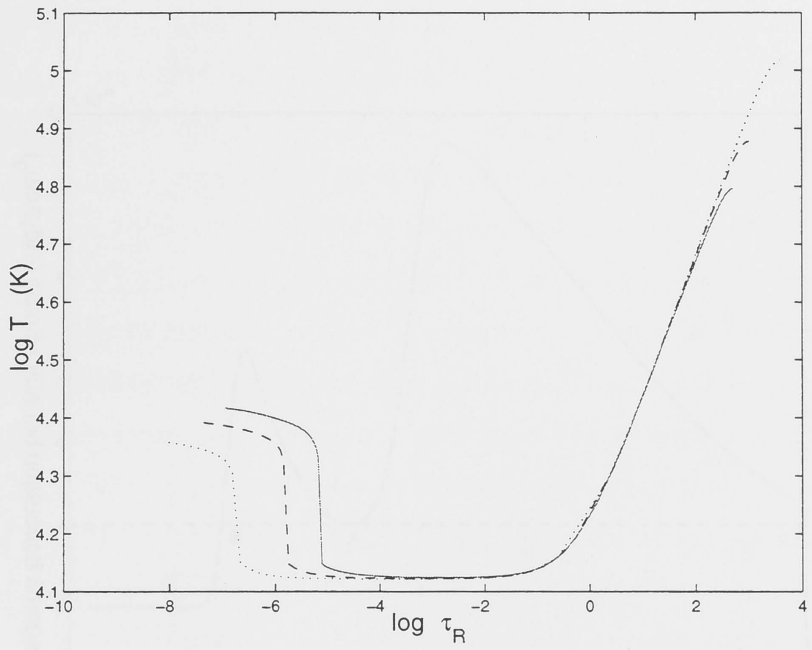

Figure 4.1: Vertical temperature distribution at disc radius $R = 7.4 \times 10^9$ cm with $\log \dot{M}(\mathrm{gs}^{-1}) = 17.0$, $M_1 = 1M_\odot$, $\Gamma = 10^3$ and $i = 15^o$. Dotted line: $\alpha = 0.05$. Dashed line: $\alpha = 0.3$. Solid line: $\alpha = 1.0$

The eigenvalue z_0 is calculated iteratively until the model converges to the solution satisfying (4.16), which is the solution for the vertical structure of the accretion disc ring at radius R. The adaptive finite-difference code FORTRAN DASSL (Brenan et al. 1989) is used to solve the equations. Although DASSL is presented as an *initial-value* algebraic-differential equation solver, we treat the boundary conditions at z_0 as initial values, and then iteratively solve for the central boundary condition at $z = 0$ using Newton's method.

We specify $\alpha = 0.3$ as a typical value for a high-state viscosity parameter. But it is important to subject this assumption to sensitivity analysis because, while T_{eff} is independent of α, the energy equation (4.14) does incorporate α. Fig. 4.1 shows the temperature structure for an accretion disc ring at $R = 7.4 \times 10^9$ cm for the three values $\alpha = 0.05$, 0.3 and 1.0. Clearly, while disc coronal structures are sensitive to α, the line formation regions in the photosphere — and hence the model spectra — are not. Therefore we are justified in using $\alpha = 0.3$ in our investigations.

It is well known — e.g., Adam et al. (1988) — that the energy equation some-

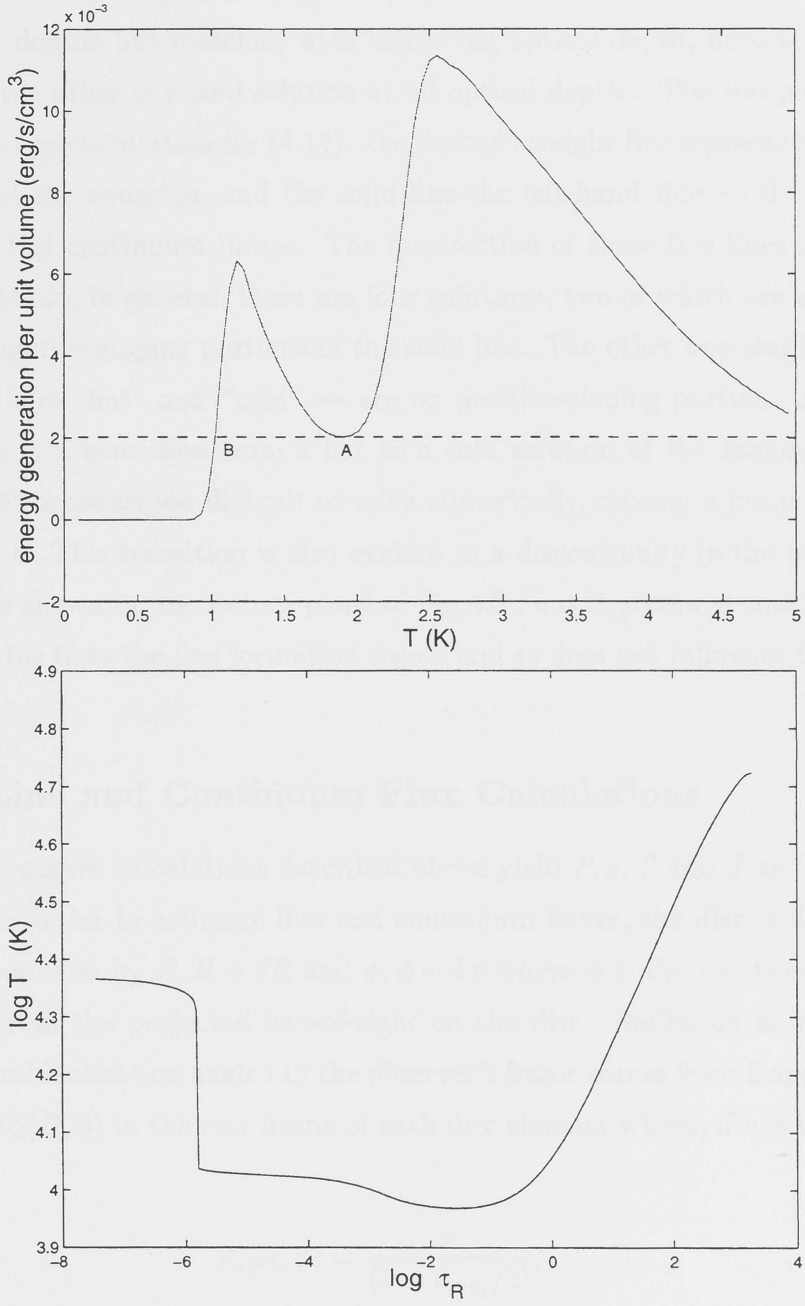

Figure 4.2: Model solutions for a disc ring at $R = 1.2 \times 10^{10}$ cm with $\log \dot{M}(\mathrm{gs}^{-1}) = 17.0$, $M_1 = 1M_\odot$, $\Gamma = 10^3$ and $i = 15^\circ$. Top: the left-hand (dashed line) and right-hand (solid line) sides of (4.14). Bottom: the vertical temperature structure.

times yields more than one solution for temperature at a given pressure. Typically there are two thermally-stable solutions, one of which starts with a hot corona at low optical depths but matches, with increasing optical depth, onto a cooler disc structure: the other is a cold solution at all optical depths. The top panel of Fig. 4.2 shows a typical solution for (4.14): the dashed straight line represents the right-hand side of the equation, and the solid line the left-hand side — the two peaks are due to HeI continuum jumps. The intersection of these two lines is the solution to (4.14) so, in general, there are four solutions, two of which are unstable — those on negative-sloping portions of the solid line. The other two stable solutions — termed here "hot" and "cold" — are on positive-sloping portions of the solid line. There is a transition from a hot to a cold solution at the tangent point A, where (4.14) becomes too difficult to solve numerically, causing a jump to the cold solution at B. This transition is also evident as a discontinuity in the temperature distribution shown in the bottom panel of Fig.4.2 , but it occurs at much shallower optical depths than the line formation region and so does not influence the emitted spectrum.

4.3.2 Line and Continuum Flux Calculations

The disc structure calculations described above yield P, ρ, T and J as functions of R and z. In order to estimate line and continuum fluxes, the disc is divided into elements bounded by $R, R + \delta R$ and $\phi, \phi + \delta\phi$ where ϕ is the rotational azimuth measured from the projected line-of-sight on the disc. Radiation at a given frequency ν and inclination angle i in the observer's frame comes from Doppler-shifted frequency $\nu_d(R, \phi)$ in the rest frame of each disc element where, if c is the velocity of light

$$\nu_d(R, \phi) = \frac{\nu}{(1 - v_{proj}/c)}, \tag{4.17}$$

$$v_{proj} = R\Omega_K(R) \sin i \sin \phi. \tag{4.18}$$

Monochromatic line and continuum opacities $\kappa_{\nu_d}(R, z)$ are then calculated, and the full plane-parallel atmosphere radiative transfer equation is solved in the frame

Table 4.1: HeI lines included in the model

3820	2p-nd triplet
3889	2s-np triplet
3965	2s-np singlet
4026	2p-nd triplet
4121	2p-ns triplet
4144	2p-nd singlet
4169	2p-ns singlet
4388	2p-nd singlet
4472	2p-nd triplet
4713	2p-ns triplet
4922	2p-nd singlet
5016	2s-np singlet
5048	2p-ns singlet
5876	2p-nd triplet

of the disc element. This yields the emergent intensity $I_{\nu_d}(\mu, R, z_0)$ at the surface $z = z_0$ of each element (R, ϕ) of the disc, where $\mu = \cos i$. The flux radiated from the surface of the disc is then calculated as

$$F_\nu = \int_R \int_\phi I_{\nu_d}(\mu, R, z_0) \mu R d\phi dR, \tag{4.19}$$

and the apparent monochromatic flux which is observed

$$f_\nu = \frac{F_\nu}{d^2}, \tag{4.20}$$

where d is the distance of the system from the Earth. These results are used to calculate absolute visual magnitudes for the model disc in order to estimate d, as well as mean colours B-V and U-B for direct comparison with observation.

In calculating the monochromatic and Rosseland opacities, we have included continuum opacities due to hydrogen and helium, but have neglected metals. Given the uncertainties in the treatment of viscosity, this assumption is expected to be of secondary importance in determining details of the vertical structure. Optical spectra are calculated including the HeI lines shown in Table 4.1 and the H_β line λ4861, allowing for Stark and thermal Doppler-broadening. Although most of the strong HeI lines have been included, some lines near series limits have been omitted because of inadequate line data. For this reason, some discrepancies in line modelling could arise with blended lines such as λ3867 and λ3889.

We use a χ^2-minimisation technique to fit observed and modelled spectra, seeking the minimum helium-to-hydrogen number density ratio Γ which gives negligible

H_β line compared with the HeI lines, and which also reproduces the general shape of the observed spectrum. The fitting is conducted in that part of the spectrum containing most of the above lines, with a considerable part of the continuum also included so as to properly fit the the continuum slope.

The best part of the spectrum for χ^2-minimisation fitting turns-out to be $4350 \leq \lambda(\mathring{A}) \leq 5800$ for AM CVn, and $4350 \leq \lambda(\mathring{A}) \leq 5100$ for CR Boo. In the latter case, this excludes the region around $\lambda 5170$, where Patterson et al. (1997) note the likelihood of a Fe/Mg-blend feature: use of this region would therefore require an extension of the model to include metal opacities. Interestingly, inclusion of the interval $\lambda < 4350\mathring{A}$ in the fitting routine yields, for both AM CVn and CR Boo, either no solution or the physically unrealistic one $M_1 > M_{ch}$: this may be because of insufficient lines in our model spectra or calibration difficulties with the observed data. To examine the possibility that a blue spectral contribution from the primary could influence the fitting, we included in some model runs a contribution to the spectrum from a black-body at the same T_{eff} as the accretor: we found the contribution to be typically less than 10% and therefore negligible.

4.3.3 Parameters for the Secondary

The secondaries in helium-rich cataclysmic variables could be degenerate helium white dwarfs (Faulkner et al. 1972), non-degenerate helium stars (Savonije et al. 1986) or helium-mantle stars with CO cores (Tutukov & Yungelson 1996 — hereafter TY96). Although predicted birth rates of these three types differ only by factors of $2 - 10$, current estimates based on binary evolution models suggest that the degenerate category will predominate in magnitude-limited samples: predicted numbers are typically higher by factors of 10^3 compared to systems with non-degenerate helium stars, and typically 10^5 compared to systems with helium mantle stars (TY96). The most promising model for AM CVn systems appears therefore to be an IWDB model where the donor is a low-mass helium-degenerate white dwarf. However for the sake of completeness, we also consider the possibility that the donor may be a semi-degenerate helium star — see Warner (1995) for a review and discussion.

Assuming a semi-degenerate donor, its mass-radius relationship is (Savonije et al. 1986)

$$\frac{R_2}{R_\odot} = 0.029 \left(\frac{M_2}{M_\odot} \right)^{-0.19}, \tag{4.21}$$

Eliminating binary separation a between the expression for orbital period

$$P_{orb} = 2\pi \left\{ \frac{a^3 q}{GM_2(1+q)} \right\}^{1/2}, \tag{4.22}$$

and the approximate expression when $q < 0.8$ for the donor's Roche lobe radius (Paczyński 1971)

$$R_{L2} = 0.462a \left(\frac{q}{1+q} \right)^{1/3}, \tag{4.23}$$

we find

$$R_{2L}^3 = \frac{(0.462)^3}{4\pi^2} GM_2 P_{orb}^2. \tag{4.24}$$

Therefore, in the mass-transfer situation when $R_2 = R_{L2}$, we find from (4.24) and (4.21) that

$$\frac{M_2}{M_\odot} = \left(\frac{0.029 R_\odot}{0.462 M_\odot^3} \right)^{1.91} \left(\frac{4\pi^2}{G P_{orb}^2} \right)^{0.64} = 629.0 P_{orb}^{-1.27}(\mathrm{s}), \tag{4.25}$$

which gives $M_2 = 0.0921 M_\odot$ and $M_2 = 0.058 M_\odot$ for AM CVn and CR Boo respectively.

On the other hand, if we assume a fully-degenerate secondary, then as previously noted

$$\frac{R_2}{R_\odot} = 0.013 \left(\frac{M_2}{M_\odot} \right)^{-1/3}, \tag{4.26}$$

and, following the same procedure as above, we find that $M_2 = 0.046 M_\odot$ for AM CVn and $M_2 = 0.032 M_\odot$ for CR Boo. In our models we assume fully-degenerate mass values for the donor but discuss, towards the end of the paper, the ramifications of varying this assumption.

4.3.4 Range Limits for the Accretion Disc

We have assumed in all our calculations that the disc extends to the surface of the white dwarf accretor, i.e., $R_{in} = R_1$. As we adopt M_1 as the main free-parameter in the model we find R_1, and hence R_{out}, from (4.2), i.e.,

$$R_{out} = 7.79 \times 10^8 \left\{ \left(\frac{M_1}{M_{ch}} \right)^{-2/3} - \left(\frac{M_1}{M_{ch}} \right)^{2/3} \right\}^{1/2} . \tag{4.27}$$

An *upper limit* for R_{out} is clearly the accretor's Roche lobe radius R_{L1} which (Eggleton 1983) is well-approximated for all q by

$$R_{L1} = \frac{0.49 q^{-2/3} a}{0.6 q^{-2/3} + \ln(1 + q^{-1/3})} \tag{4.28}$$

or, using (4.22), by

$$R_{L1} = \frac{0.49 q^{-1}}{0.6 q^{-2/3} + \ln(1 + q^{-1/3})} \left\{ \frac{G M_2 (1+q)}{4\pi^2} P_{orb}^2 \right\}^{1/3} . \tag{4.29}$$

We have estimates of M_2 from above and know P_{orb} from observations so, with M_1 as the main free-parameter, we may find R_{L1} and hence an upper limit for R_{out}. More refined estimates of R_{out} are discussed next in the context of setting a range grid for solving the disc-structure equations.

4.3.5 Setting the Model Grid

Given viscosity parameter α, disc structure — and thus the emergent spectrum — may be calculated once R_{out}, $\dot{M}$, M_1, Γ and i are specified. To do this, for a given value of R_{out}, we form the four parameter grid: $0.5 \leq (M_1/M_\odot) \leq 1.4$, $2 \leq \log \Gamma \leq 4$, $16.5 \leq \log \dot{M}(\mathrm{gs}^{-1}) \leq 18.0$ and $15^\circ \leq i \leq 75^\circ$. Then, aided by the χ^2-minimisation technique, we use this grid to seek those parameters generating model spectra which best fit the observed spectra of AM CVn and CR Boo.

Note that R_{out} is not used as a grid parameter: this is because the concomitant increase in computing time is not warranted by increased precision in comparison with simple models of disc size. The above analysis showing that $R_{out} \leq R_{L1}$ is one such simple model, while the *tidal radius* concept (Frank et al. 1992) suggesting that $R_{out} = 09 R_{L1}$ is a related one. Yet another arises by considering streamlines at

the outer edge of a close binary accretion disc — where disc pressure and viscosity are very small — as simple periodic orbits in the restricted three-body problem. Paczyński (1977) found in these circumstances that the maximum radius of the last stable orbit

$$R_{st} = r_{max} a \tag{4.30}$$

for tabulated $r_{max} = r_{max}(q)$. For all q corresponding to stellar masses of interest here — i.e., $0.5 \leq (M_1/M_\odot) \leq 1.3$ and $0.03 \leq (M_2/M_\odot) \leq 0.1$ — the tables show that $r_{max} = 0.48$ to within 1%. So, using (4.28), a *lower limit* for R_{out} is

$$R_{st} = 0.98\{0.6 + q^{2/3} \ln(1 + q^{-1/3})\} R_{L1}, \tag{4.31}$$

in which case, for the q values of interest here, $0.71 \leq (R_{st}/R_{L1}) \leq 0.92$. Hence $R_{st} \leq R_{out} \leq R_{L1}$ and accordingly, when using the model, we construct two range grids; one with $R_{out} = R_{L1}$ and the other with $R_{out} = R_{st}$. While best fits from these two grids are not greatly different, indications are that R_{out} is in fact closer to R_{L1}, and that is the value we use to present spectral fits.

Note also that, because R_{L1} from (4.28) is not very sensitive to changes in q for typical AM CVn system configurations and hence — from (4.31) — neither is R_{st}, our model results for AM CVn systems are relatively insensitive to q. In particular, changing from fully to semi-degenerate values for M_2 does not greatly change predicted disc spectra.

As a practical compromise between model accuracy and computing time we divide the disc into 10 equally-spaced elemental rings. To demonstrate the reasonableness of this compromise, Fig. 4.3 shows spectra for an accretion disc which have been calculated with 10, 20 and 30 elemental rings: the difference in half-maximum line widths for $\lambda 4471$ between a 10-ring and 30-ring disc is less than 0.1%.

As a further measure to economise on computing resources, all discs are initially constructed with $R_{out} = 1.3 \times 10^{10}$ cm — larger than any disc anticipated for either AM CVn or CR Boo. Then, for each M_1 point in the grid, this large disc is cut-down in size to the appropriate $R_{out} = R_{st}$ or R_{L1}, both of which depend on q. In other words, for given $\dot{M}$, M_1, Γ and i, we use the same $R_{out} = 1.3 \times 10^{10}$ cm disc to construct discs with various $R_{out} \leq 1.3 \times 10^{10}$ cm.

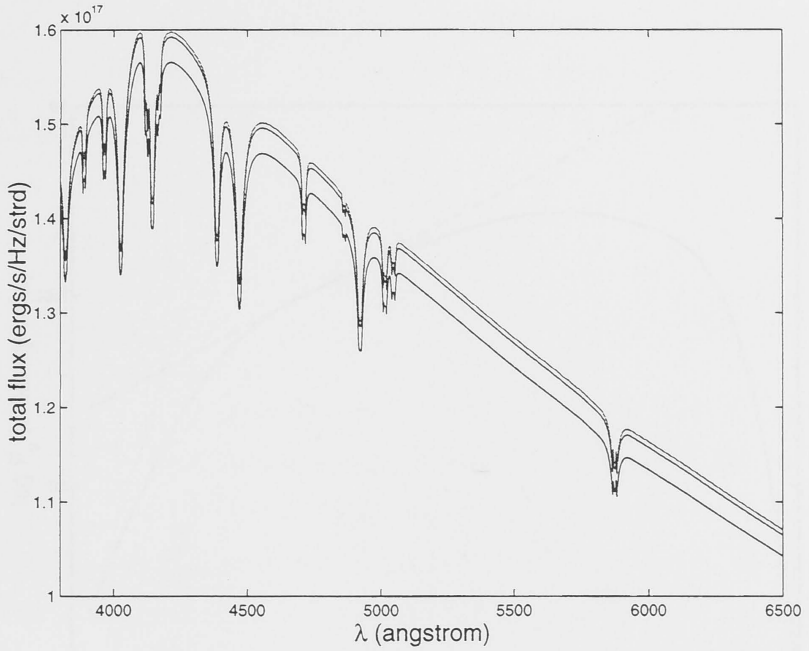

Figure 4.3: Disc spectra with $R_{out} = 1.3 \times 10^{10}$ cm, $\log \dot{M}(\mathrm{gs}^{-1}) = 16.5$, $M_1 = 1 M_\odot$, $\Gamma = 10^3$ and $i = 15°$. Upper to lower: 30, 20 and 10 elemental rings

4.4 Results

To help understand the χ^2-minimisation fitting results presented later in this Section, we first examine whether the $\nu^{1/3}$ spectrum common in accretion discs — e.g., Wade 1984 — is expected in AM CVn systems. This is followed by an investigation of the influence of parameters R_{out}, $\dot{M}$, M_1, Γ and i on the continuum energy distribution and line profiles for radiation emitted by accretion discs.

4.4.1 The General Shape of the Spectrum

In an optically-thick accretion disc, one can approximate the flux from an elemental ring at radius R by that of a black body with effective temperature given by (4.1), and so — see Frank et al. 1992 — the *total disc* flux is

$$F_\nu = \frac{4\pi h \nu^3 \cos i}{c^2} \int_{R_1}^{R_{out}} \frac{R dR}{\exp(h\nu/kT_{eff}) - 1}, \tag{4.32}$$

where h is Planck's constant. Note that the flux is independent of α, which is characteristic of optically-thick discs in a steady-state. For small frequencies —

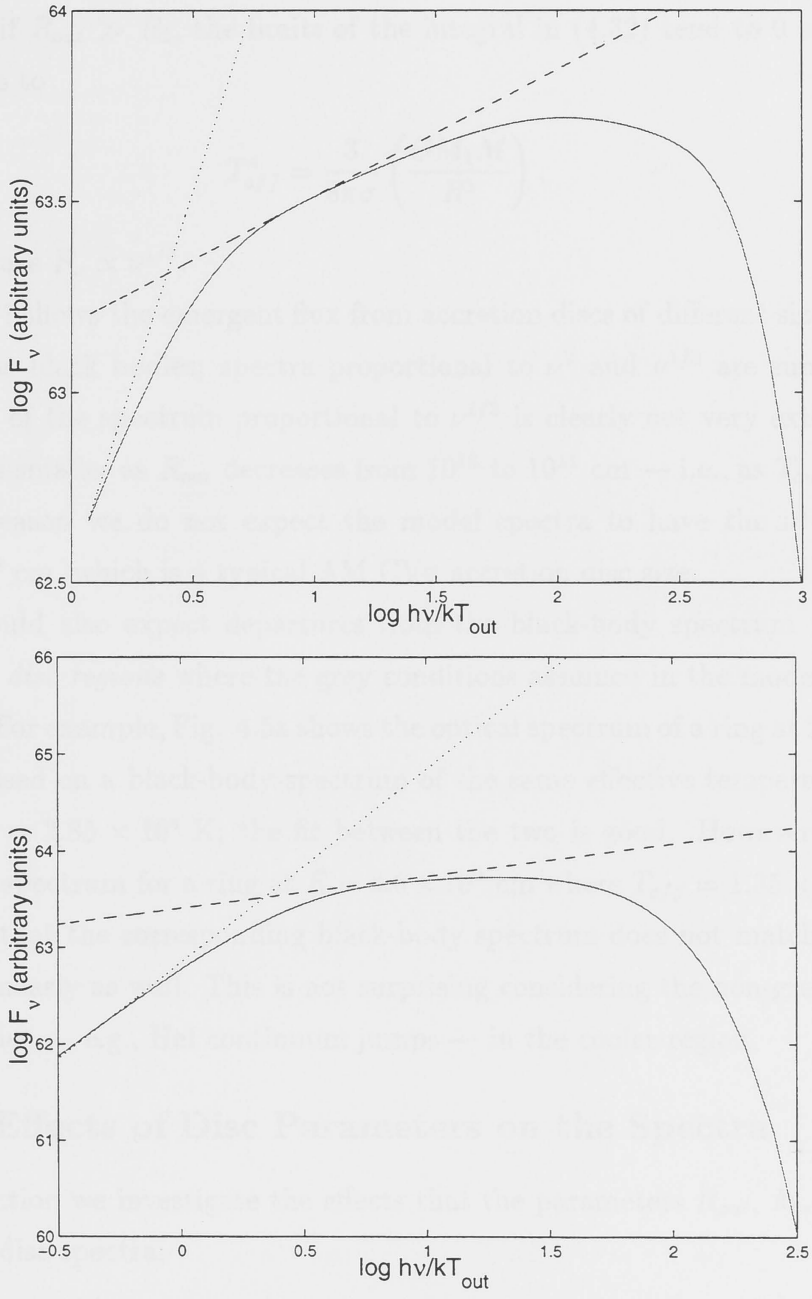

Figure 4.4: The continuum flux F_ν of a disc radiating as a black body (solid line) with $\log \dot{M}(\mathrm{gs}^{-1}) = 17.0$, $M_1 = 1M_\odot$, $\Gamma = 10^3$ and $i = 15^o$. The dashed line is $\propto \nu^{1/3}$ and the dotted line is $\propto \nu^2$. Top: $R_{out} = 10^{12}$ cm. Bottom: $R_{out} = 10^{11}$ cm.

$\nu \ll kT_{out}/h$ — we have the Rayleigh-Jeans behaviour $F_\nu \propto \nu^2$, while for large frequencies — $\nu \gg kT_{out}/h$ — we have the Wien form $F_\nu \propto \nu^2 \exp(-h\nu/kT_{eff})$. Moreover if $R_{out} \gg R_1$, the limits of the integral in (4.32) tend to 0 and ∞, and (4.1) tends to

$$T_{eff}^4 = \frac{3}{8\pi\sigma}\left(\frac{GM_1\dot{M}}{R^3}\right), \tag{4.33}$$

in which case $F_\nu \propto \nu^{1/3}$.

Fig. 4.4 shows the emergent flux from accretion discs of different size which are emitting as black bodies; spectra proportional to ν^2 and $\nu^{1/3}$ are superimposed. That part of the spectrum proportional to $\nu^{1/3}$ is clearly not very extensive, and it becomes smaller as R_{out} decreases from 10^{12} to 10^{11} cm — i.e., as T_{out} increases. For this reason we do not expect the model spectra to have the $\nu^{1/3}$ form for $R_{out} \sim 10^9$ cm, which is a typical AM CVn accretion disc size.

We would also expect departures from the black-body spectrum to be more evident in *disc regions* where the grey conditions assumed in the model clearly do not hold. For example, Fig. 4.5a shows the optical spectrum of a ring at 2.9×10^9 cm superimposed on a black-body spectrum of the same effective temperature as the ring, $T_{eff} = 2.85 \times 10^4$ K; the fit between the two is good. However, Fig. 4.5b shows the spectrum for a ring at $R = 8.6 \times 10^9$ cm where $T_{eff} = 1.35 \times 10^4$ K, and it is clear that the corresponding black-body spectrum does not match the model spectrum nearly as well. This is not surprising considering the non-grey nature of the opacities — e.g., HeI continuum jumps — in the cooler region.

4.4.2 Effects of Disc Parameters on the Spectra

In this Section we investigate the effects that the parameters R_{out}, $\dot{M}$, M_1, Γ and i have on disc spectra.

Disc Size R_{out}

Fig. 4.6 shows spectra for discs with $R_{out} = 1.3 \times 10^{10}$ cm and 6.3×10^9 cm. In general, if all other parameters are held constant, line profiles become deeper and narrower with increasing disc radius. This is expected, because contributions to

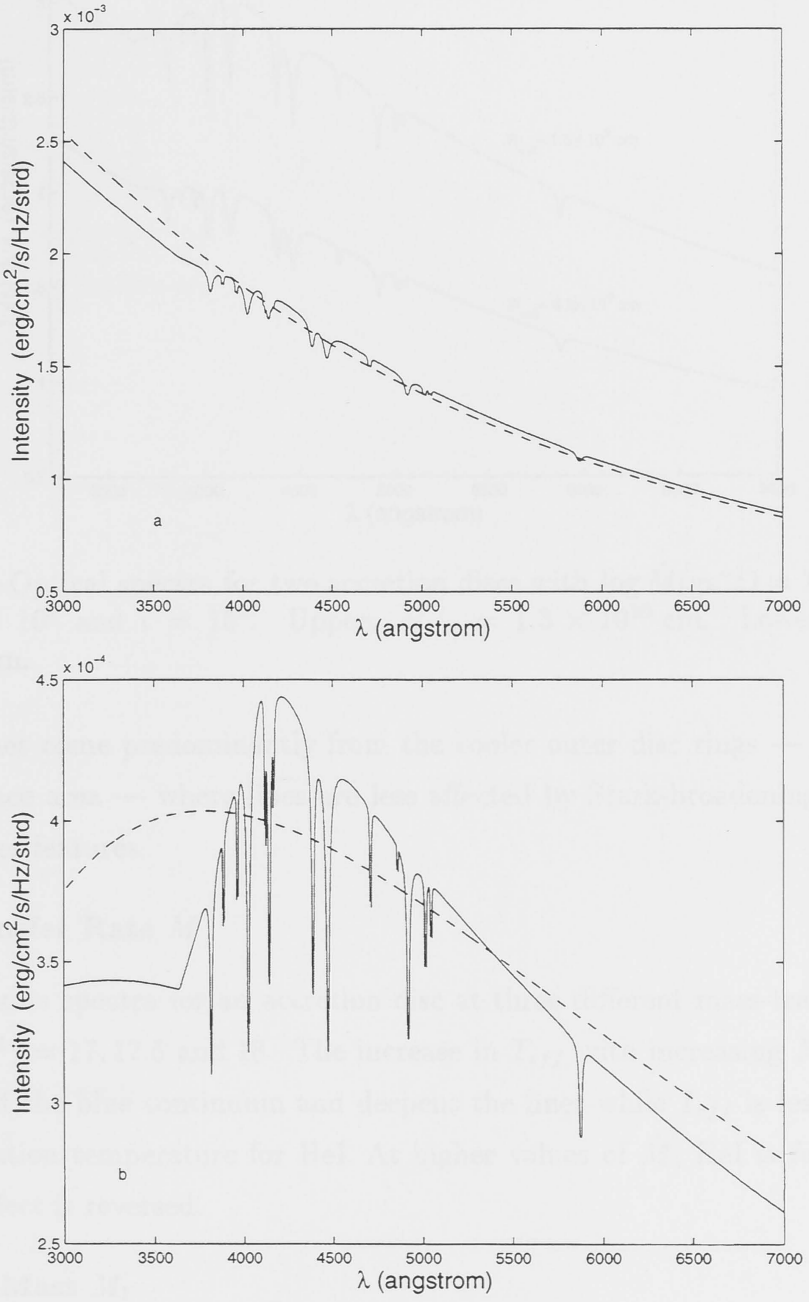

Figure 4.5: Optical spectra from the outer ring in accretion discs with $\log \dot{M}(\ \mathrm{gs}^{-1}) = 17.0$, $M_1 = 1M_\odot$, $\Gamma = 10^3$ and $i = 15^\circ$. Top: ring at $R_{out} = 2.9 \times 10^9$ cm. Bottom: ring at $R_{out} = 8.6 \times 10^9$ cm.

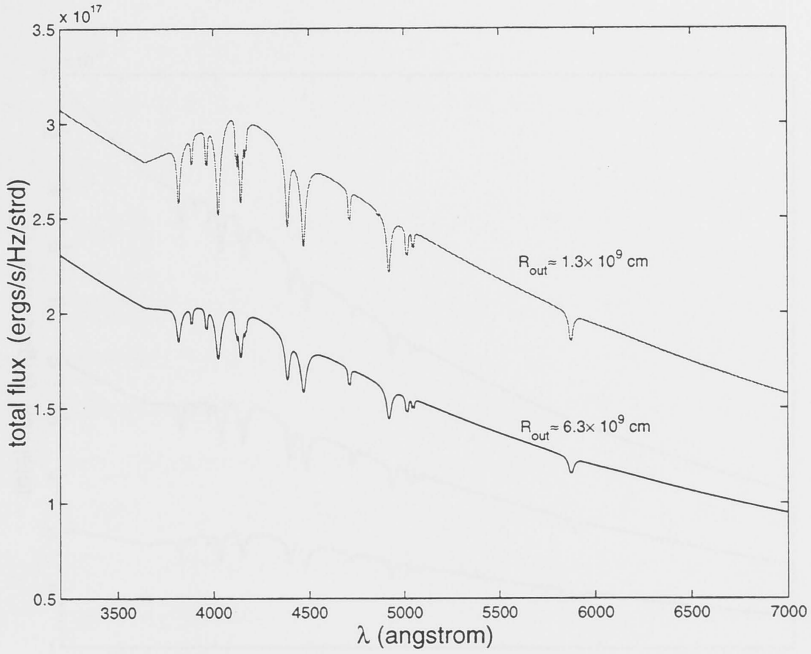

Figure 4.6: Optical spectra for two accretion discs with $\log \dot{M}(\mathrm{gs}^{-1}) = 17.0$, $M_1 = 1M_\odot$, $\Gamma = 10^3$ and $i = 15^\circ$. Upper: $R_{out} = 1.3 \times 10^{10}$ cm. Lower: $R_{out} = 6.3 \times 10^9$ cm.

spectral lines come predominantly from the cooler outer disc rings — with their larger surface area — where lines are less affected by Stark-broadening and thus have sharper features.

Mass-Transfer Rate $\dot{M}$

Fig. 4.7 shows spectra for an accretion disc at three different mass-transfer rates $\log \dot{M}(\mathrm{gs}^{-1}) = 17, 17.5$ and 18. The increase in T_{eff} with increasing $\dot{M}$ steepens the slope of the blue continuum and deepens the lines while T_{eff} is less than the peak ionisation temperature for HeI. At higher values of $\dot{M}$, HeI is fully-ionised and this effect is reversed.

Accretor Mass M_1

Fig. 4.8 shows that, as expected from (4.1), the effect of increasing gravity as M_1 increases is similar to that of $\dot{M}$ noted above; i.e., the continuum slope and line depths increase with increasing M_1. But, as $M_1 \propto R_1^{-3}$, the M_1-effect is even more

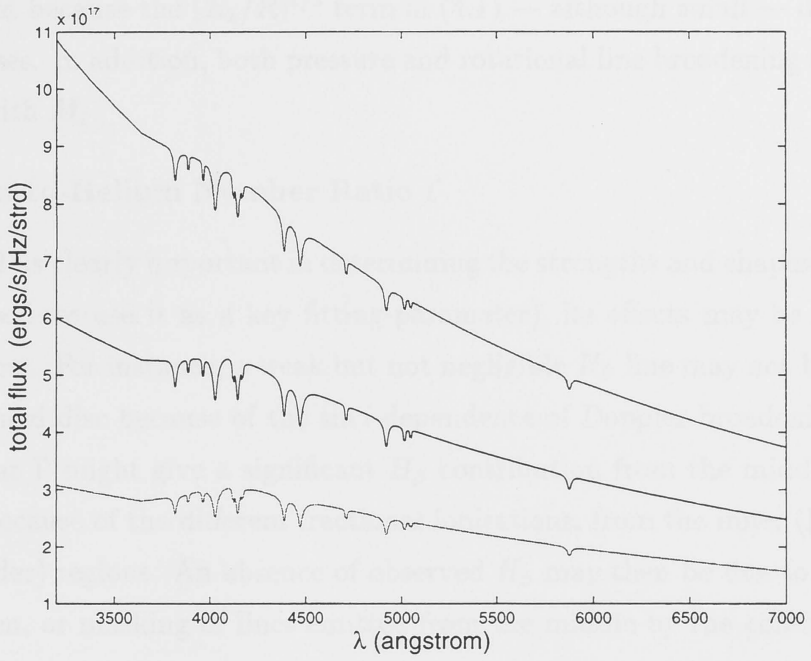

Figure 4.7: Optical spectra for an accretion disc with $R_{out} = 1.3 \times 10^{10}$ cm, $M_1 = 1M_\odot$, $\Gamma = 10^3$ and $i = 15^o$. Upper to lower: $\log \dot{M}(\mathrm{gs}^{-1}) = 18.0$, 17.5 and 17.0.

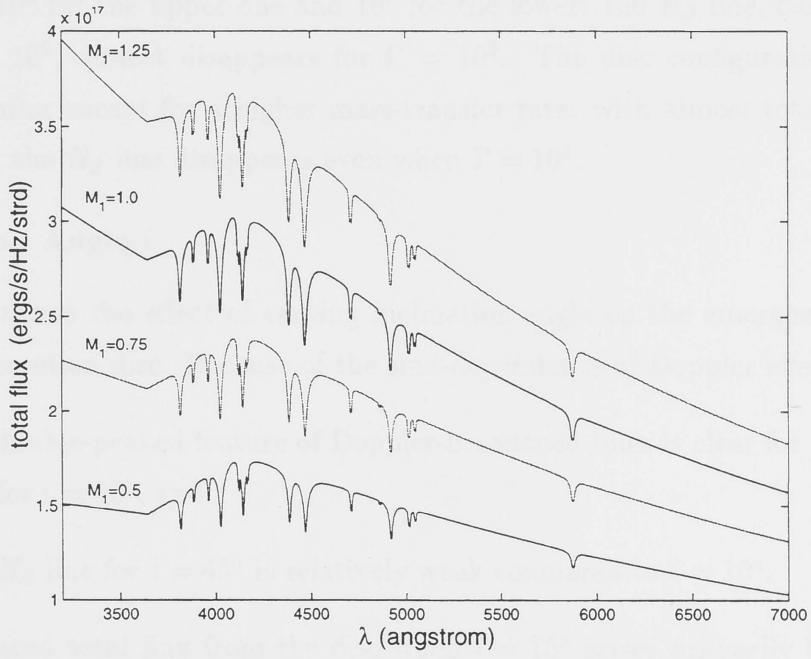

Figure 4.8: Optical spectra for an accretion disc with $R_{out} = 1.3 \times 10^{10}$ cm, $\log \dot{M}(\mathrm{gs}^{-1}) = 17.0$, $i = 15^o$. Upper to lower: $(M_1/M_\odot) = 1.25$, 1.0, 0.75 and 0.5.

pronounced because the $(R_1/R)^{1/2}$ term in (4.1) — although small — decreases as M_1 increases. In addition, both pressure and rotational line broadening (for $i \neq 0^o$) increase with M_1.

Hydrogen-to-Helium Number Ratio Γ

Although Γ is clearly important in determining the strengths and shapes of spectral lines (indeed we use it as a key fitting-parameter), its effects may be masked by other factors. For instance, a weak but not negligible H_β line may not be observed in an inclined disc because of the $\sin i$-dependence of Doppler-broadening. Again, a particular Γ might give a significant H_β contribution from the middle of a disc but not, because of the different fractional ionisations, from the inner (hotter) and outer (colder) regions. An absence of observed H_β may then be due to either lack of hydrogen, or masking of lines emitted from the middle by the continuum from elsewhere in the disc.

The spectral influence of Γ is strongly-dependent on T_{eff} — and hence $\dot{M}$ — as is shown in Fig. 4.9. Fig. 4.9a shows spectra from two discs differing only in that $\Gamma = 10^2$ for the upper one and 10^3 for the lower: the H_β line, clearly visible with $\Gamma = 10^2$, almost disappears for $\Gamma = 10^3$. The disc configuration for Fig. 4.9b is similar except for a higher mass-transfer rate: with almost total hydrogen ionisation, the H_β line disappears even when $\Gamma = 10^2$.

Inclination Angle i

Fig. 4.10 shows the effect of varying inclination angle on the emergent spectrum from an accretion disc. Because of the $\sin i$-dependence of Doppler effects:

- the double-peaked feature of Doppler-broadened lines is clear for $i = 45^o$ but not for $i = 15^o$, and
- the H_β line for $i = 45^o$ is relatively weak compared to $i = 15^o$.

The enhanced total flux from the disc when $i = 15^o$ arises primarily because the projected surface area of the disc seen by the observer depends on $\cos i$.

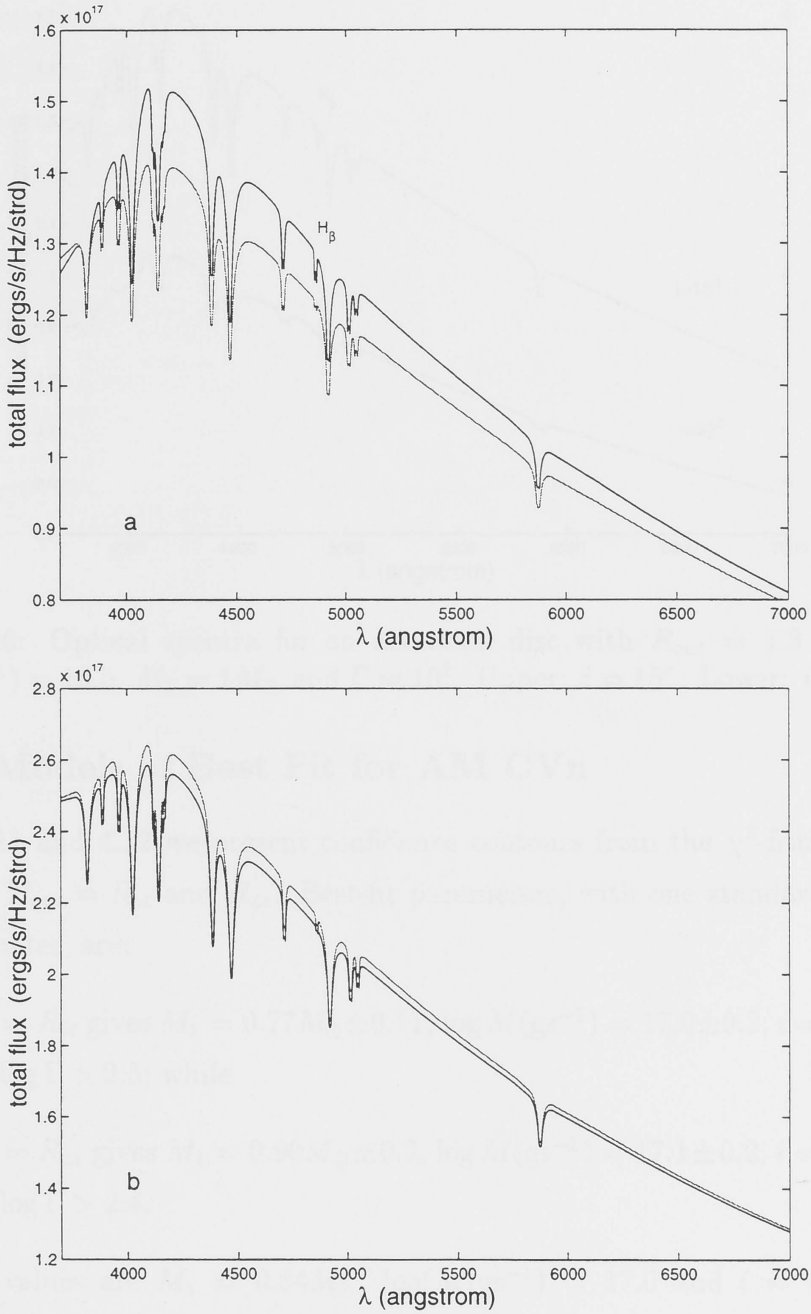

Figure 4.9: Optical spectra for an accretion disc with $R_{out} = 8.6 \times 10^9$ cm, $M_1 = 1M_\odot$ and $i = 15^o$. Panel (a): $\log \dot{M}(\mathrm{gs}^{-1}) = 16.5$, with (upper) $\Gamma = 10^2$ and (lower) $\Gamma = 10^3$. Panel (b): $\log \dot{M}(\mathrm{gs}^{-1}) = 17.0$, with (upper) $\Gamma = 10^2$ and (lower) $\Gamma = 10^3$.

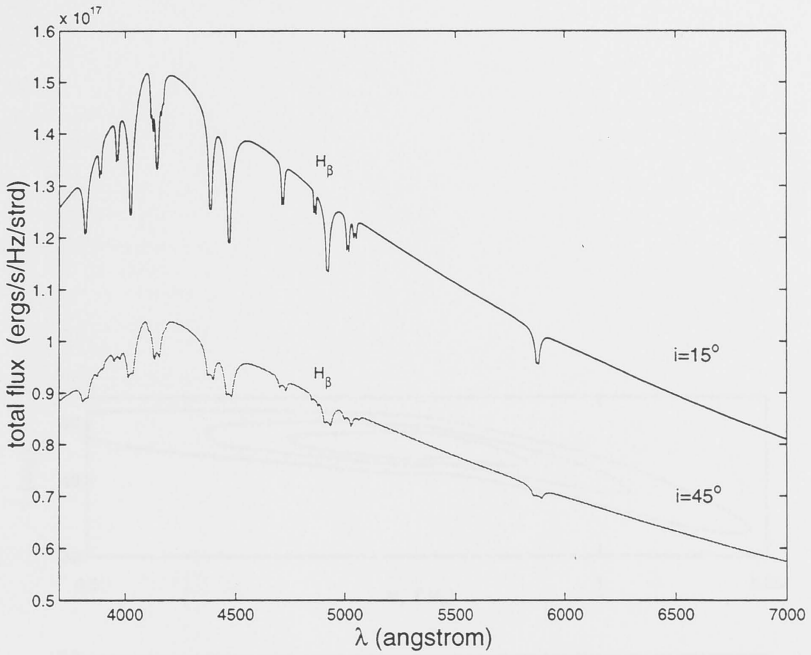

Figure 4.10: Optical spectra for an accretion disc with $R_{out} = 1.3 \times 10^{10}$ cm, $\log \dot{M}(\mathrm{gs}^{-1}) = 16.5$, $M_1 = 1M_\odot$ and $\Gamma = 10^2$. Upper: $i = 15^o$. Lower: $i = 45^o$.

4.4.3 Models of Best Fit for AM CVn

In Figs 4.11 and 4.12 we present confidence contours from the χ^2-fitting for AM CVn with $R_{out} = R_{st}$ and R_{L1}. Best-fit parameters, with one standard deviation error estimates, are:

- $R_{out} = R_{st}$ gives $M_1 = 0.77M_\odot \pm 0.11$, $\log \dot{M}(\mathrm{gs}^{-1}) = 17.0 \pm 0.2$, $i = 46.0^o \pm 2.6$ and $\log \Gamma > 2.5$; while

- $R_{out} = R_{L1}$ gives $M_1 = 0.90M_\odot \pm 0.2$, $\log \dot{M}(\mathrm{gs}^{-1}) = 17.1 \pm 0.2$, $i = 43.7^o \pm 3.5$ and $\log \Gamma > 2.4$.

Averaged values are $M_1 = 0.84M_\odot$, $log(\dot{M}(\mathrm{gs}^{-1}) = 17.0$ and $i = 44.9^o$. The value for M_1 is near the $0.65M_\odot$ peak value of the distribution of primary masses predicted for AM CVn systems in TY96.

The difference in fit between the two cases is not great, although an increase in M_1 with increasing R_{out} is evident. This may be explained by two competing effects noted earlier:

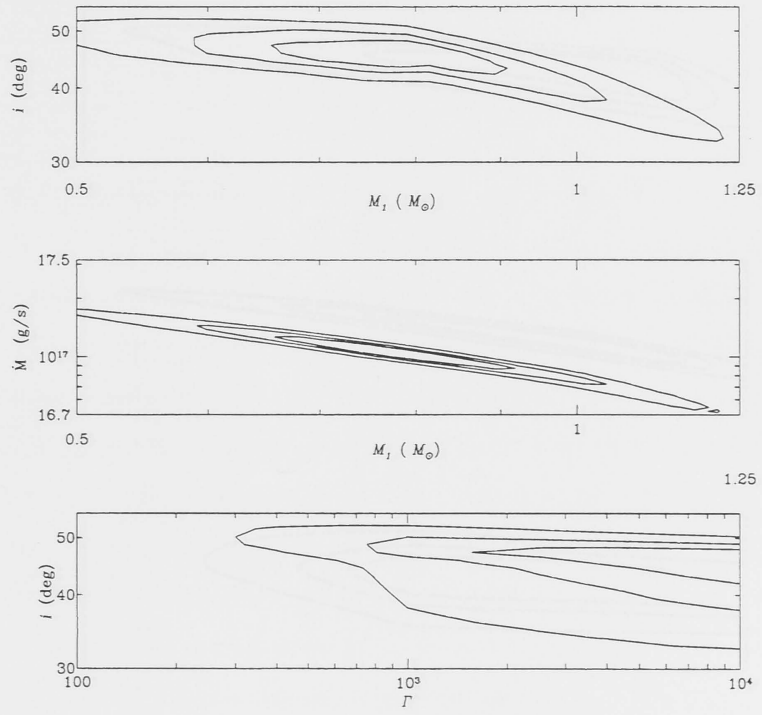

Figure 4.11: Confidence contours from χ^2-fitting for AM CVn with $R_{out} = R_{st}$. Inner to outer: 99%, 90% and 66% confidence level.

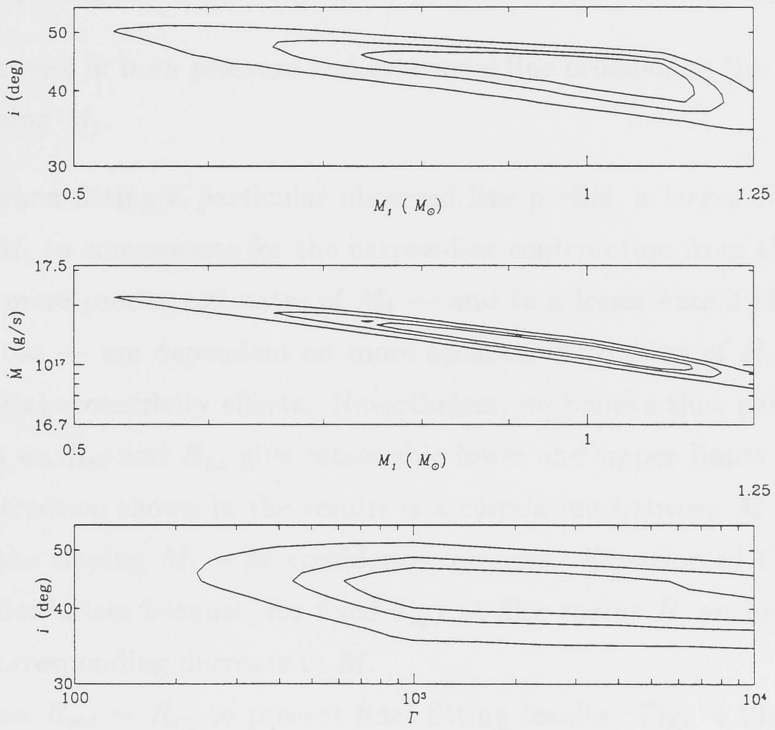

Figure 4.12: Confidence contours from χ^2-fitting for AM CVn with $R_{out} = R_{L1}$. Inner to outer: 99%, 90% and 66% confidence level.

Table 4.2: Mean colours for AM CVn and CR Boo

mean colour	observed	predicted
	AM CVn	
B-V	-0.074	-0.073
U-B	-0.955	-0.966
	CR Boo	
B-V	-0.050	-0.072
U-B	-0.972	-0.966

- the deepening and narrowing of line profiles with increasing R_{out}, and
- the increase in both pressure and rotational line broadening (for $i \neq 0°$) with increasing M_1.

Therefore, when fitting a particular observed line profile, a larger R_{out} needs an increase in M_1 to compensate for the narrow-line contribution from the outer disc regions. So more precise estimates of M_1 — and to a lesser extent the other disc parameters too — are dependent on more accurate estimation of R_{out}, including possible orbital-eccentricity effects. Nevertheless, we believe that parameter estimates based on R_{st} and R_{L1} give reasonable lower and upper limits respectively. Another interaction shown in the results is a correlation between $\dot{M}$ and M_1, evident from the sloping $M_1 - \dot{M}$ confidence contours. Equation (4.1) shows that this correlation arises because, for fixed T_{eff} at disc radius R, an increase in M_1 requires a corresponding decrease in $\dot{M}$.

We choose $R_{out} = R_{L1}$ to present final fitting results. Fig. 4.13a shows that part of the observed spectrum where χ^2-minimisation is applied, on which is superimposed the best-fit model spectrum when $R_{out} = R_{L1}$. Fig. 4.13b shows the same best-fit model spectrum superimposed on the full observed spectrum. Using (4.20), these results indicate that the distance d of AM CVn from the Earth lies in the interval $338 - 495$ pc. Mean colours B-V and U-B from observed and predicted data for AM CVn are compared in the upper part of Table 4.2: despite a possible bias caused by the $3550 \leq \lambda \leq 6150$ bandpass for observed data, there is less than 1.5% difference between corresponding values.

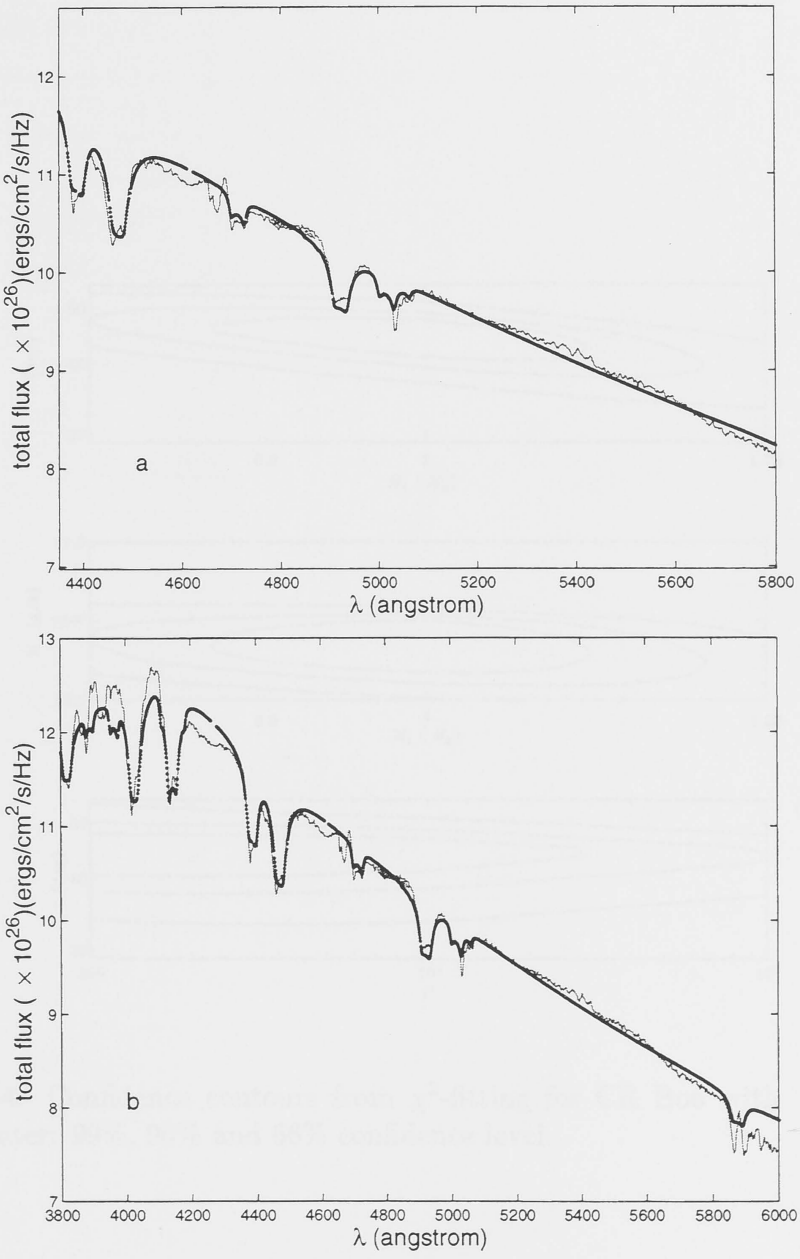

Figure 4.13: Observed spectrum of AM CVn (thin line) superimposed on the best-fit spectrum (thick line) with $R_{out} = R_{L1}$. Panel (a) shows that part of the spectrum where χ^2-minimisation is applied. Panel (b) shows the full spectrum.

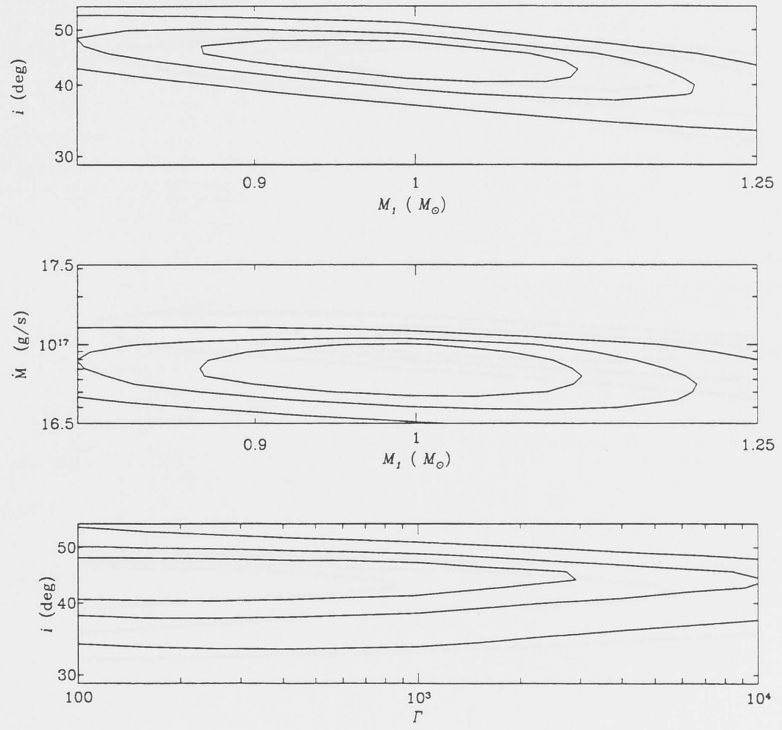

Figure 4.14: Confidence contours from χ^2-fitting for CR Boo with $R_{out} = R_{st}$. Inner to outer: 99%, 90% and 66% confidence level.

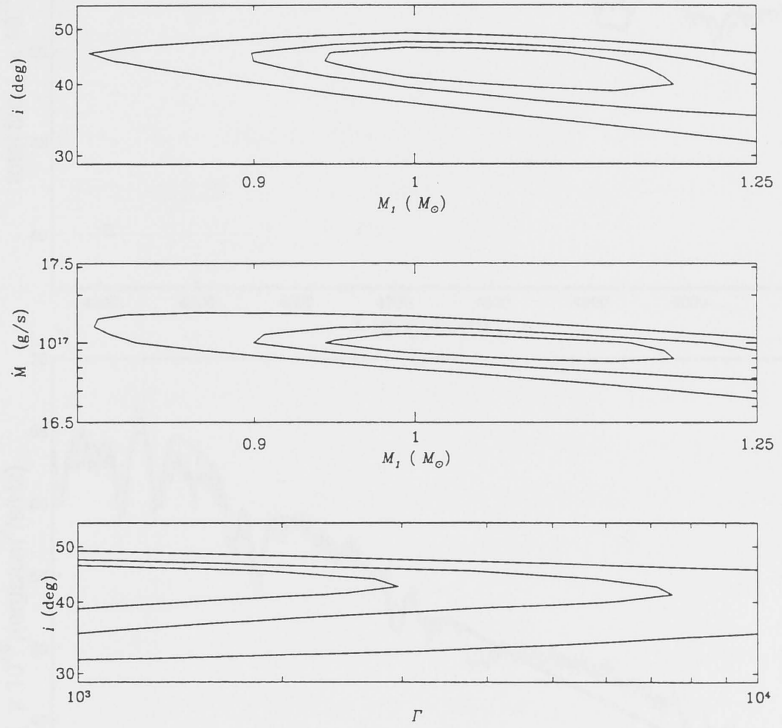

Figure 4.15: Confidence contours from χ^2-fitting for CR Boo with $R_{out} = R_{L1}$. Inner to outer: 99%, 90% and 66% confidence level.

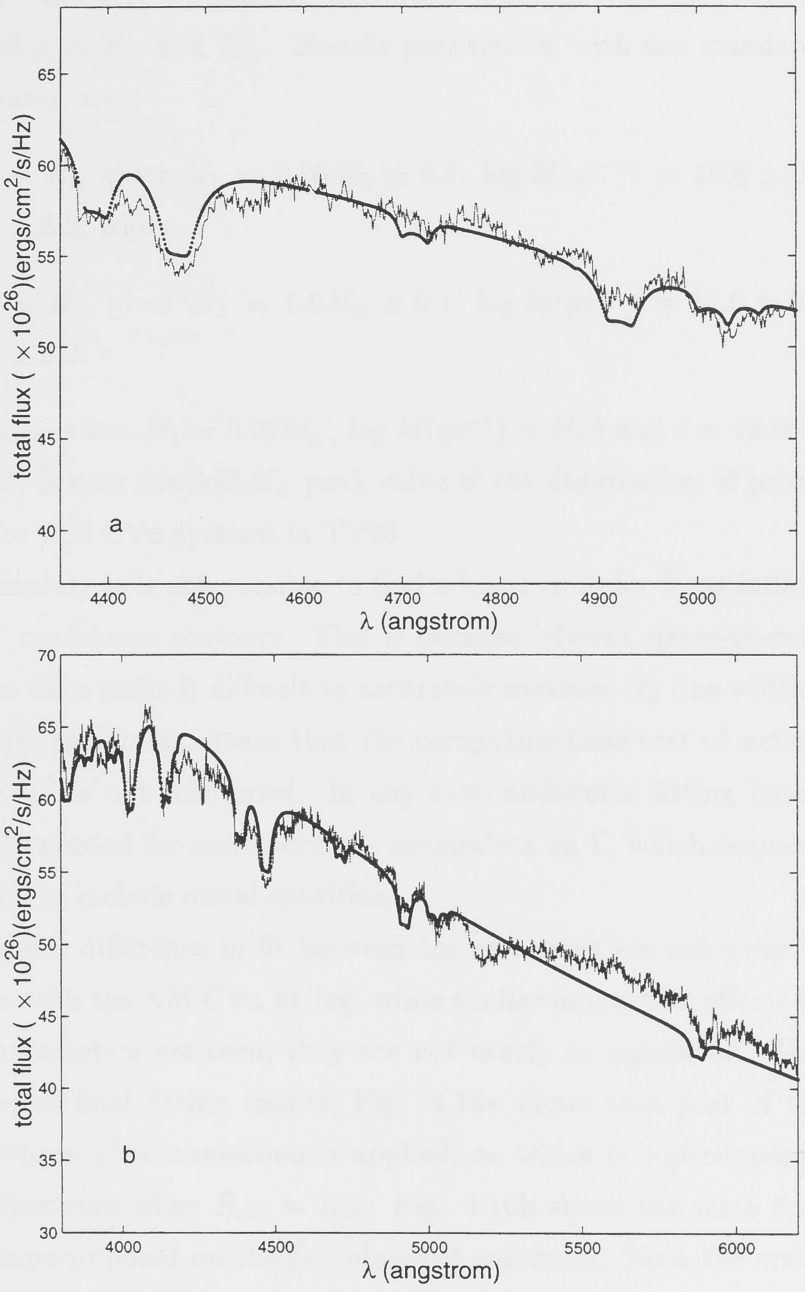

Figure 4.16: Observed spectrum of CR Boo (thin line) superimposed on the best-fit spectrum (thick line) with $R_{out} = R_{L1}$. Panel (a) shows that part of the spectrum where χ^2-minimisation is applied. Panel (b) shows the full spectrum.

4.4.4 Models of Best Fit for CR Boo

In Figs 4.14 and 4.15 we present confidence contours from the χ^2-fitting for CR Boo with $R_{out} = R_{st}$ and R_{L1}. Best-fit parameters, with one standard deviation error estimates, are:

- $R_{out} = R_{st}$ gives $M_1 = 0.98M_\odot \pm 0.1$, $\log \dot{M}(\mathrm{gs}^{-1}) = 16.8 \pm 0.3$ and $i = 44.6^o \pm 3.2$; while
- $R_{out} = R_{L1}$ gives $M_1 = 1.0M_\odot \pm 0.1$, $\log \dot{M}(\mathrm{gs}^{-1}) = 17.0 \pm 0.2$ and $i = 43.0^o \pm 3.2$.

Averaged values are $M_1 = 0.99M_\odot$, $\log \dot{M}(\mathrm{gs}^{-1}) = 16.9$ and $i = 43.8^o$. Again the value for M_1 is near the $0.65M_\odot$ peak value of the distribution of primary masses predicted for AM CVn systems in TY96.

Unfortunately it is not possible to find a lower limit for Γ, as indicated by the open $i - \Gamma$ confidence contours. This is because adverse signal-to-noise levels in the CR Boo data make it difficult to accurately measure H_β line widths. And this inherent data limitation means that the computing-time cost of extending the Γ grid below 10^2 is not warranted. In any case, additional fitting based on metal lines may be needed for more accurate constraints on Γ, which requires extension of the model to include metal opacities.

Once again, difference in fit between the two cases are not great. Indeed, in comparison with the AM CVn fitting, while similar interaction effects between CR Boo disc parameters are seen, they are not nearly as significant. Using $R_{out} = R_{L1}$ to present final fitting results, Fig. 4.16a shows that part of the observed spectrum where χ^2-minimisation is applied, on which is superimposed the best-fit model spectrum when $R_{out} = R_{L1}$. Fig. 4.16b shows the same best-fit model spectrum superimposed on the full observed spectrum. Note the crude fitting of the continuum around the Fe/Mg-blend feature near $\lambda 5170$, which — as mentioned earlier — is not within the spectral interval used for χ^2-minimisation.

Using (4.20), these results indicate that the distance d of CR Boo from the Earth lies in the interval $191 - 221$ pc. Mean colours B-V and U-B from observed and predicted data for CR Boo are compared in the lower part of Table 4.2: note

that there is a possible bias caused by the $3450 \leq \lambda \leq 6450$ bandpass for observed data. The difference between predicted and observed mean colours is less than 1% for U-B but, probably because the Fe/Mg-blend feature is lacking in our model, is about 44% for B-V. Nevertheless, our estimates of mean colours for CR Boo are well within those of Wood et al. (1987). Furthermore, our results are consistent with observational data (Warner 1995) suggesting that mean colours for CR Boo in a high state are similar to those of AM CVn.

4.5 Discussion and Conclusions

It is widely believed (Warner 1995) that AM CVn systems are cataclysmic variables at a late evolutionary stage. A plausible scenario (TY96) has them originating as high-mass wide binaries which evolve through two common envelope stages, leaving components which are remnant cores from evolved stars. The present accretor's progenitor would have been initially the more massive, typically leaving a C-O white dwarf after ejection of the first common envelope. The less massive — and hence less evolved — progenitor of the present donor enters the second common envelope stage with a helium-rich core. They emerge from the second common envelope stage as a short-period binary and, when orbital angular momentum losses from gravitational radiation bring them close enough for the present donor to experience Roche lobe overflow, mass transfer at rate $\dot{M}$ through a helium-rich accretion disc commences.

During this latter quasi-stable mass-transfer phase, assuming mass conservation but orbital angular momentum losses from gravitational radiation, the donor's mean mass-loss rate $\dot{M}_2$ is related to the orbital period P_{orb} by (Warner 1995)

$$\dot{M}_2 = 8 \times 10^{17} \frac{q^2}{(1+q)^{1/3}} \left(\frac{5}{6} + \frac{\xi_{ad}}{2} - q \right)^{-1} \left(\frac{M_1}{M_\odot} \right)^{8/3} \left(\frac{P_{orb}}{1\mathrm{hr}} \right)^{-8/3} \mathrm{gs}^{-1} \quad (4.34)$$

where, for entropy S

$$\xi_{ad} = \left. \frac{\partial \ln R_2}{\partial \ln M_2} \right|_S \quad (4.35)$$

is the donor's adiabatic radius-mass coefficient. If the accretion disc is in a *stable*

thermal regime then we expect $\dot{M}_2 \approx \dot{M}$ but if, on the other hand, it is in an *unstable* regime then we expect

- $\dot{M}_2 < \dot{M}$ if the system is in a low state, and
- $\dot{M}_2 > \dot{M}$ if it is in a high state.

We now consider whether our results are consistent with this general picture and, in particular whether the results

- support the thermal disc-instability explanation of the brightness variations observed in CR Boo but not in AM CVn, and
- throw any light on the level of degeneracy in the helium-rich binary component.

4.5.1 Thermal Stability of the Best-Fit AM CVn Disc

For the purposes of studying disc stability we take the average of relevant best-fit parameters from Section 4.4.3 for the AM CVn model. The mean value $M_1 = 0.84M_\odot$ and we know that $P_{orb} = 1028.7$ s, so with the fully-degenerate donor mass $M_2 = 0.046M_\odot$ and $\xi_{ad} = -1/3$ from Section 4.3.3 we find $\log \dot{M}_2(\mathrm{gs}^{-1}) = 16.8$. As this is approximately the same as the average disc mass-transfer rate $\log \dot{M}(\ \mathrm{gs}^{-1}) = 17.0$, our results are consistent with the observed stable behaviour of AM CVn.

If we assume a semi-degenerate donor mass $M_2 = 0.092M_\odot$ with $\xi_{ad} = -0.19$ then $\log \dot{M}_2(\mathrm{gs}^{-1}) = 17.4$. As this is a factor of 2.5 greater than the average disc mass-transfer rate from modelling, a semi-degenerate donor seems inconsistent with the observed stable behaviour of AM CVn. Further supportive evidence for a fully-degenerate donor in AM CVn comes from the detectable upper limit 50 km/s on K_1 noted by PHS. Using averaged best-fit values for AM CVn parameters, we find that $K_1 = 32$ km/s with the fully-degenerate donor and 62 km/s with the semi-degenerate one: so a fully-degenerate donor seems more plausible on these grounds too.

If the above arguments about thermal stability of the best-fit AM CVn model hold, then we should be able to find an R_{out} within the allowable $R_{st} \leq R_{out} \leq R_{L1}$ interval for which the whole best-fit disc is thermally stable. In fact using the average best-fit parameters, $R_{out} = 8.7 \times 10^9$ cm — which is within the $7.1 \times 10^9 \leq R_{out}(\mathrm{cm}) \leq 9.2 \times 10^9$ allowable range — generates an S-curve which places AM CVn just on the stable branch. This is shown in Fig. 4.17, where it is clear that the upper turning-point occurs at $\log \dot{M}(\ \mathrm{gs}^{-1}) = 17.0$, and any part of the disc inside this radius will also be stable at that mass-transfer rate. Hence our best-fit parameters are able to give disc models for AM CVn that are thermally stable, which is in accord with observations.

4.5.2 Thermal Stability of the Best-Fit CR Boo Disc

For CR Boo, the mean value $M_1 = 0.99 M_\odot$ and we know that $P_{orb} = 1471$ s, so with the fully-degenerate donor mass $M_2 = 0.032 M_\odot$ and $\xi_{ad} = -1/3$ we find $\log \dot{M}_2(\mathrm{gs}^{-1}) = 16.1$. As this is considerably less than the average disc mass-transfer rate $\log \dot{M}(\ \mathrm{gs}^{-1}) = 16.9$, our results are consistent with CR Boo being in the instability regime but in a high state.

If we assume a semi-degenerate donor mass $M_2 = 0.058 M_\odot$ with $\xi_{ad} = -0.19$, then $\log \dot{M}_2(\mathrm{gs}^{-1}) = 16.7$. As this is also considerably less than the average disc mass-transfer rate from modelling, a semi-degenerate donor is also consistent with the observed unstable behaviour of CR Boo. The predicted value of K_1 for CR Boo using averaged best-fit parameters are 18 km/s for a fully-degenerate donor and 32 km/s for the fully-degenerate donor. Both values are too small to be detectable at present, so no conclusion may be drawn from them about the nature of the secondary in CR Boo.

If the best-fit CR Boo model is in the instability regime as suggested above, then we should be able to find a best-fit disc satisfying $R_{st} \leq R_{out} \leq R_{L1}$, within which there is a region where $\dot{M}_2$ lies on the unstable branch of the S-curve but $\dot{M}$ lies on the hot branch. We find that $R = 7.0 \times 10^9$ cm — which is within the $9.4 \times 10^9 \leq R_{out}(\mathrm{cm}) \leq 1.3 \times 10^{10}$ allowable range — generates an S-curve which does just this. This is shown in Fig. 4.18, where the upper turning-point occurs at

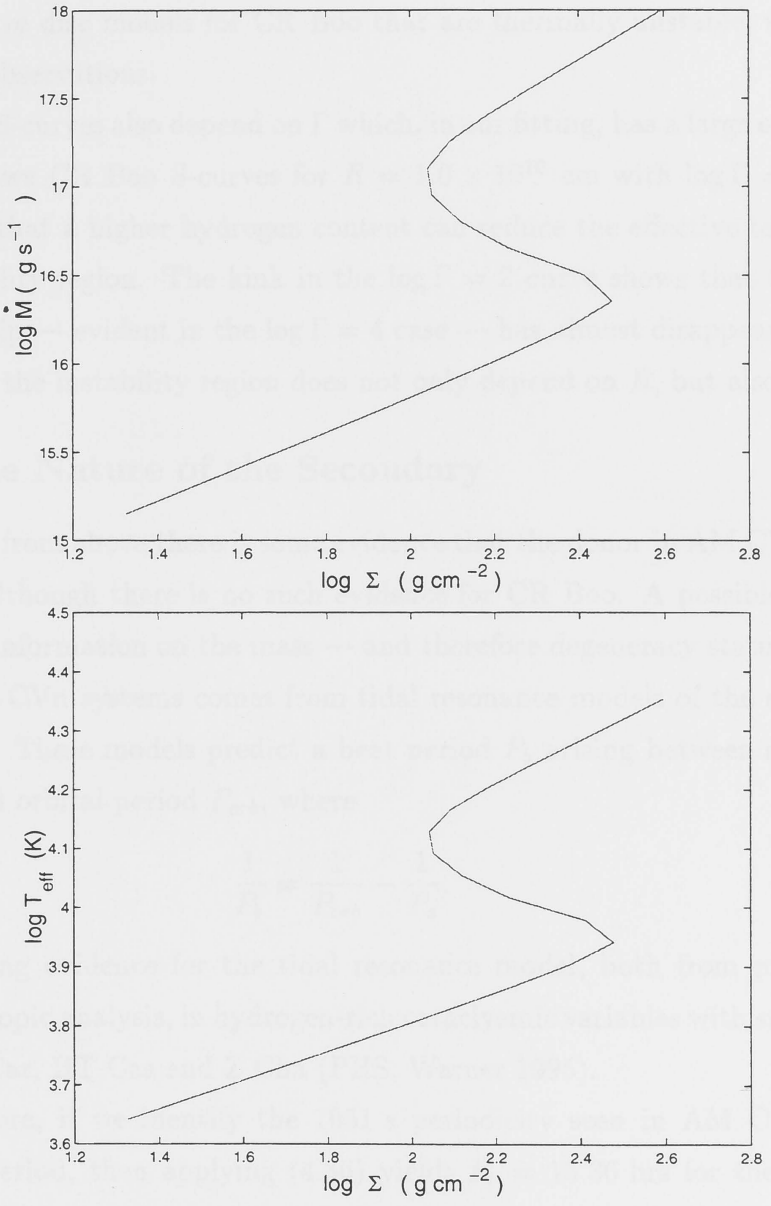

Figure 4.17: S-curves for the best-fit AM CVn model with $R_{out} = 8.7 \times 10^9$ cm, $M_1 = 0.84 M_\odot$ and $\log \Gamma = 3$.

about $\log \dot{M}(\ \mathrm{gs}^{-1}) = 16.9$, $\log \dot{M}_2(\mathrm{gs}^{-1})$ is on the unstable branch. Any part of the disc inside this radius will also be unstable at the average CR Boo mass-transfer rate as is also shown in Fig. 4.18 for $R = 5 \times 10^9$ cm. Hence our best-fit parameters are able to give disc models for CR Boo that are thermally unstable, which is in accord with observations.

However, S-curves also depend on Γ which, in our fitting, has a large error range: Fig. 4.19 shows CR Boo S-curves for $R = 1.0 \times 10^{10}$ cm with $\log \Gamma = 2$, 3 and 4. It is clear that a higher hydrogen content can reduce the effective temperature of the instability region. The kink in the $\log \Gamma = 2$ curve shows that the helium instability strip — evident in the $\log \Gamma = 4$ case — has almost disappeared. Hence the nature of the instability region does not only depend on R, but also on Γ.

4.5.3 The Nature of the Secondary

We have seen from above there is some evidence that the donor in AM CVn is fully-degenerate, although there is no such evidence for CR Boo. A possible source of independent information on the mass — and therefore degeneracy status — of the donor in AM CVn systems comes from tidal resonance models of the superhump phenomenon. These models predict a beat period P_b arising between superhump period P_s and orbital period P_{orb}, where

$$\frac{1}{P_b} = \frac{1}{P_{orb}} - \frac{1}{P_s}. \tag{4.36}$$

There is strong evidence for the tidal resonance model, both from photometric and spectroscopic analysis, in hydrogen-rich cataclysmic variables with superhumps such as OY Car, HT Cas and Z Cha (PHS, Warner 1995).

Furthermore, if we identify the 1051 s periodicity seen in AM CVn with a superhump period, then applying (4.36) yields $P_b = 13.36$ hrs for the AM CVn orbital period $P_{orb} = 1028.7$ s. And similarly the hypothesised 1490 s superhump period in CR Boo gives $P_b = 32.0$ hrs. Now (Warner 1995) the tidal resonance model for superhumps leads to the relationship

$$\frac{P_b}{P_{orb}} = \frac{3.73(1+q)}{q} \tag{4.37}$$

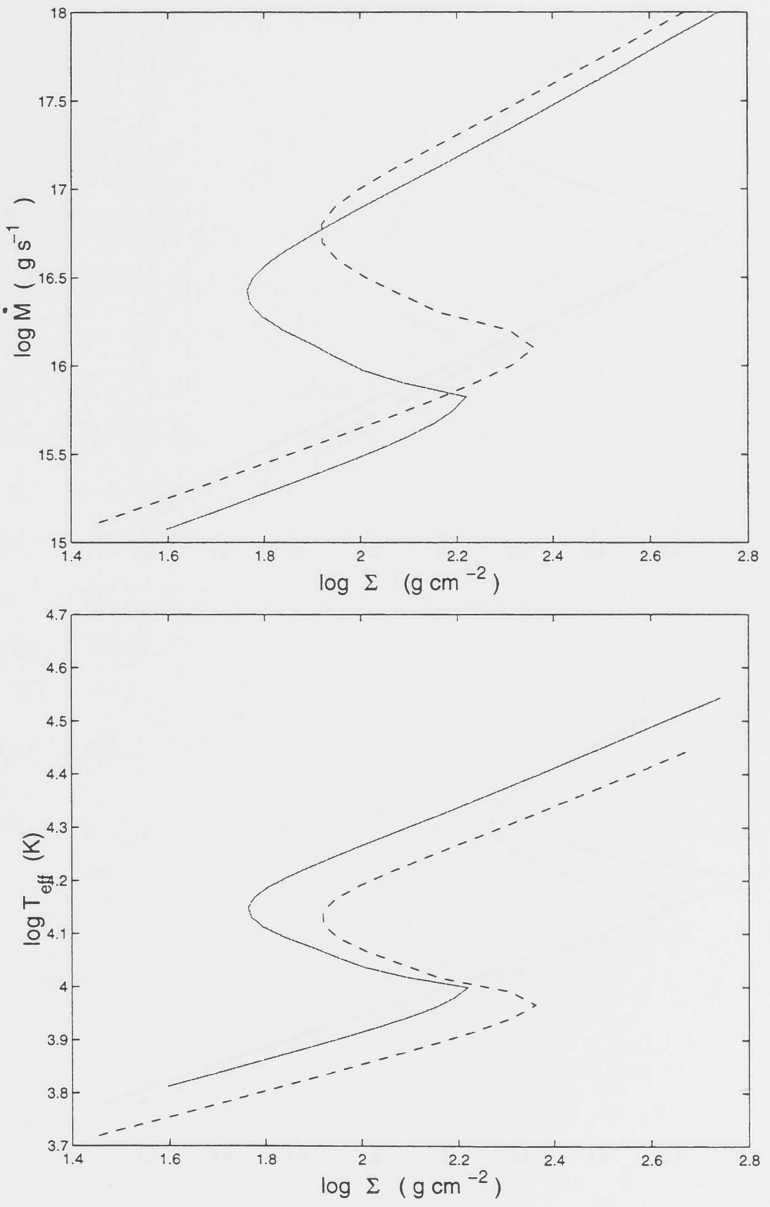

Figure 4.18: S-curves for the best-fit CR Boo model with $M_1 = 0.99 M_\odot$ and $\log \Gamma = 3$. Dashed line: $R = 7 \times 10^9$ cm. Solid line: $R = 5 \times 10^9$ cm.

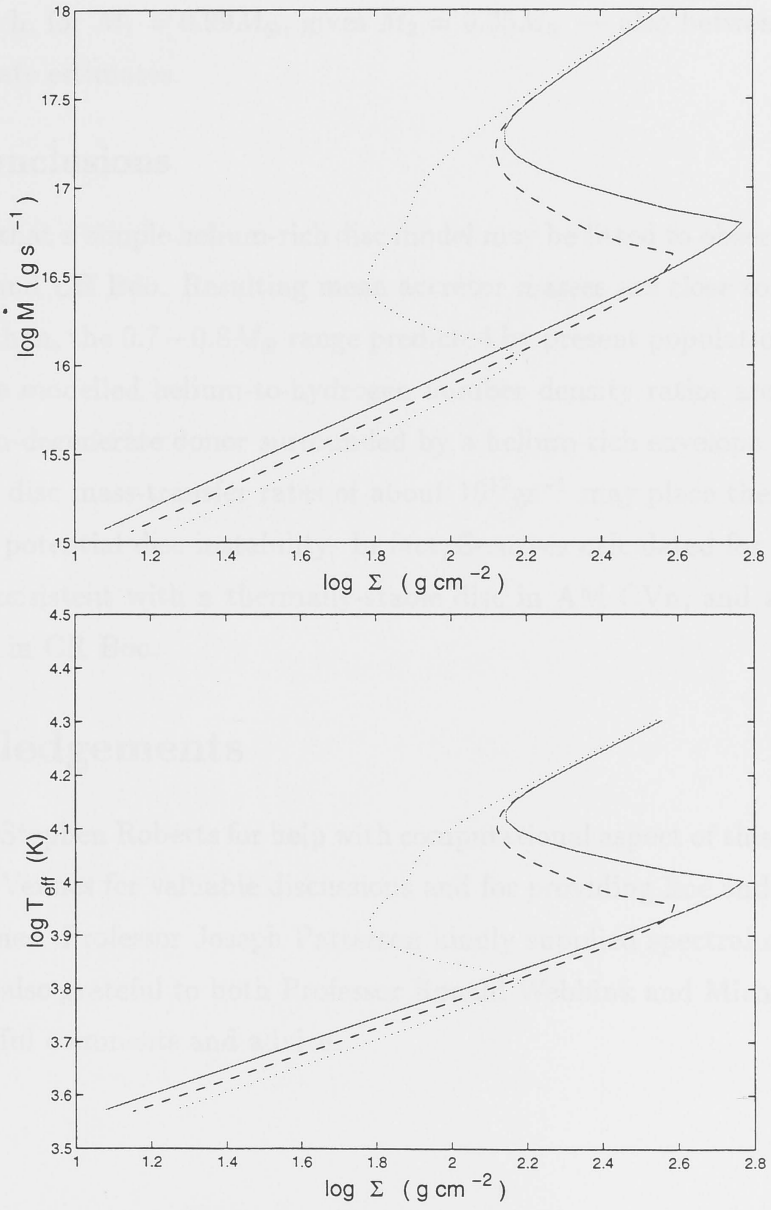

Figure 4.19: S-curves for the best-fit CR Boo model with $M_1 = 0.99 M_\odot$ at $R = 1.0 \times 10^{10}$ cm. Dotted line: $\log \Gamma = 2$. Dashed line: $\log \Gamma = 3$, Solid line: $\log \Gamma = 4$.

for low mass ratios q. Hence, for AM CVn we find $q = 0.087$, which, using our average best-fit estimate $M_1 = 0.84M_\odot$, results in $M_2 = 0.07M_\odot$, between our estimates of fully and semi-degenerate secondary masses. Similarly for CR Boo $q = 0.05$ which, for $M_1 = 0.99M_\odot$, gives $M_2 = 0.05M_\odot$ — also between fully and semi-degenerate estimates.

4.5.4 Conclusions

We conclude that a simple helium-rich disc model may be fitted to observed spectra of AM CVn and CR Boo. Resulting mean accretor masses are close to, but somewhat higher than, the $0.7 - 0.8M_\odot$ range predicted by present population synthesis studies, while modelled helium-to-hydrogen number density ratios are consistent with a helium-degenerate donor surrounded by a helium-rich envelope.

Predicted disc mass-transfer rates of about $10^{17}\mathrm{gs}^{-1}$ may place the systems in the region of potential disc instability. In fact, S-curves calculated for the best-fit models are consistent with a thermally-stable disc in AM CVn, and a thermally unstable disc in CR Boo.

Acknowledgements

We thank Dr Stephen Roberts for help with computational aspect of this paper, and Dr Stéphane Vennes for valuable discussions and for providing line and continuum opacity routines. Professor Joseph Patterson kindly supplied spectral data on CR Boo. We are also grateful to both Professor Ronald Webbink and Michael Burgess for their helpful comments and advice.

Bibliography

[1] Adam, J., Störzer, H., Shaviv, G., & Wehrse, R. 1988, A&A, 193, L1

[2] Brenan, K. E., Campbell, S. L., & Petzold, L. R. 1989, Numerical Solution of Initial-Value Problems in Differential-Algebraic Equations (New York: Elsevier)

[3] Burbidge, G., Burbidge, M., & Hoyle, F. 1967, ApJ, 147, 121

[4] Burbidge, E. M., & Strittmatter, P. A. 1971, ApJ, 170, L39

[5] Eggleton, P. P. 1983, ApJ, 268, 368

[6] Faulkner, J., Flannery, B. P., & Warner, B. 1972, ApJ 175, L79

[7] Frank, J., King, A. R., & Raine, D. 1992, Accretion Power in Astrophysics (Cambridge: Cambridge Univ. Press)

[8] Greenstein, J. L., & Mathews, M. S. 1957, ApJ, 126, 14

[9] Harvey, D. A., Skillman, D. R., Kemp, J., Patterson, J., Vanmunster, T., Fried, R. E., & Retter, A. 1998, ApJ, 493, L105

[10] Howell, S. B., Szkody, P., Kreidel, T. J., & Dobrzycka, D. 1991, Publ. Astr. Soc. Pac, 103, 300

[11] Humason, M. L., & Zwicky, F. 1947, ApJ, 105, 85

[12] Malmquist, K. G., 1936, Stockholms Observatoriums Annaler Vol. 12, 7, 130

[13] Nather, R. E. 1985, in NATO ASI Ser. C Vol.150, Interacting Binaries, ed, P. P. Eggleton, & J. E. Pringle (Dordrecht: Reidel), 349

[14] Nauenberg, M. 1972, ApJ, 175, 417

[15] O'Donoghue, D., Menzies, J. & Hill, P. W. 1987, MNRAS, 227, 295

[16] O'Donoghue, D., Kilkenny, D., Chen, A., Stobie, R. S., Koen, M. C., Warner, B., & Lawson, W. A. 1994, MNRAS, 271, 910

[17] Osaki, Y. 1996, Pub. Astr. Soc. Pac., 108, 390

[18] Paczyński, B. 1971, Ann. Rev. A&A, 9, 183

[19] Paczyński, B. 1977, ApJ, 216, 822

[20] Patterson, J., Sterner, E., Halpern, J., & Raymond J. C. 1992, ApJ, 384, 234

[21] Patterson, J., Halpern, J., & Shambrok, A. 1993, ApJ, 419, 803

[22] Patterson, J., Kemp, J., Shambrook, A., & Thomas, E. 1997, Publ. Astr. Soc. Pac., 103, 1100

[23] Savonije, G. J., de Kool, M,. & Van den Heuvel, E. P. J. 1986, A&A, 155, 51

[24] Shakura, N. I., & Sunyaev, R. 1973, A&A, 24, 337.

[25] Shaviv, G., & Wehrse, R. 1986, A&A, 159, L5

[26] Smak, J. 1967, Acta Astron., 17, 255

[27] Tutukov, A., & Yungelson, L. 1996, MNRAS, 280, 1035

[28] Wade, R. A. 1984, MNRAS, 208, 381

[29] Wampler, E. J. 1967, ApJ, 149, L101

[30] Warner, B. 1972, MNRAS, 159, 315

[31] Warner, B., & Robinson, E. L. 1972, MNRAS, 159, 101

[32] Warner, B. 1995, Cataclysmic Variable Stars (Cambridge: Cambridge Univ. Press)

[33] Wehrse, R., Baschek, B., & Shaviv, G. 1994, in ASP Conf. Ser. Vol. 56, Interacting Binary Stars, ed. A. W. Shafter (Provo: Brigham Young Univ.), 35

[34] Wood, M. A., Winget, D. E., Nather, R. E., & Hessman, F. V. 1987, ApJ, 313, 757

Chapter 5

Accretion Disc Model for EC15330-1403

Walid El-Khoury[1,†] Stéphane Vennes[1,‡]
& Dayal Wickramasinghe[1,*]

[1] The Astrophysical Theory Centre and The Department of Mathematics, Australian National University, ACT, 0200, Australia.

[†] email: walid@maths.anu.edu.au

[‡] email: vennes@maths.anu.edu.au

[*] email: dayal@maths.anu.edu.au

5.1 Introduction

EC15330-1403 was discovered in the Edinburgh-Cape survey of blue stars and subsequently categorised as an AM CVn system by photometric and spectroscopic analysis (O'Donoghue et al. 1994). It is therefore expected to comprise a white dwarf accretor with a helium-rich donor (probably either semi or fully-degenerate) and accretion disc (Warner 1995). The fundamental period of its rapid brightness variations is 1119 s, with only two harmonics: no radial velocity variations were detected.

In this paper we attempt to fit, using a χ^2-minimisation technique, optical spectra of EC15330-1403 to predicted spectra from a model of the vertical structure and emergent flux from thin accretion discs (El-Khoury & Wickramasinghe 1999). We present model fits for both phase and averaged spectra of EC15330-1403.

Table 5.1: Spectral data for EC15330-1403. First column shows the phase, second column the radial velocity V and third column the standard deviation ΔV.

MJD	V	ΔV
982.414484	-22.7980	49.294
982.416992	5.6549	48.301
982.419492	-33.9373	59.542
982.422000	55.0316	56.486
982.424508	-39.1798	100.532
982.427010	-37.5153	80.395
982.429521	8.4646	71.085
982.432020	29.0098	75.887
982.434520	-48.6109	58.706
982.437028	8.9037	61.567
982.442794	48.8498	57.425
982.444606	-29.2396	66.985
982.446411	33.4872	61.076
982.448215	20.0478	60.836
982.450019	113.3627	91.627
982.451824	6.8426	102.536
982.453630	-38.0421	62.020
982.455433	-32.6557	93.007
982.457239	62.9086	61.953
982.459045	-13.7138	71.899

5.2 Spectroscopic Study

We obtained two consecutive series of spectra on June 18 1998 with Siding Spring Observatory's 2.3m telescope and the DBS spectrograph equipped with 300 g/mm grating on the blue side and a 316 g/mm grating on the red side — resolution of 6 Å. The first series for ten spectra was exposed for 3 minutes each and the second series of 10 spectra for 2 minutes each. The spectra were flux calibrated with standard star Feige 110, and wavelength calibrated with FeAr arcs on the blue side and NeAr arcs on the red side.

The radial velocities shown in Table 5.1 and Fig. 5.1 are obtained by cross-correlating (using NOAO IRAF's fxcor) each spectrum with the averaged spectrum used as a template over the wavelength range between λ3500 and λ4500. At the spectral resolution, 6 Å, the standard deviation, $\Delta V = 41.7$ km/s, is consistent with no measurable motion — expected velocity accuracy is 45 km/s. We also estimate the mean colours to be B-V= -0.08 ± 0.1 and U-B= -1.14 ± 0.15. However, it is difficult to correct for atmospheric dispersion in the U-band using a narrow slit.

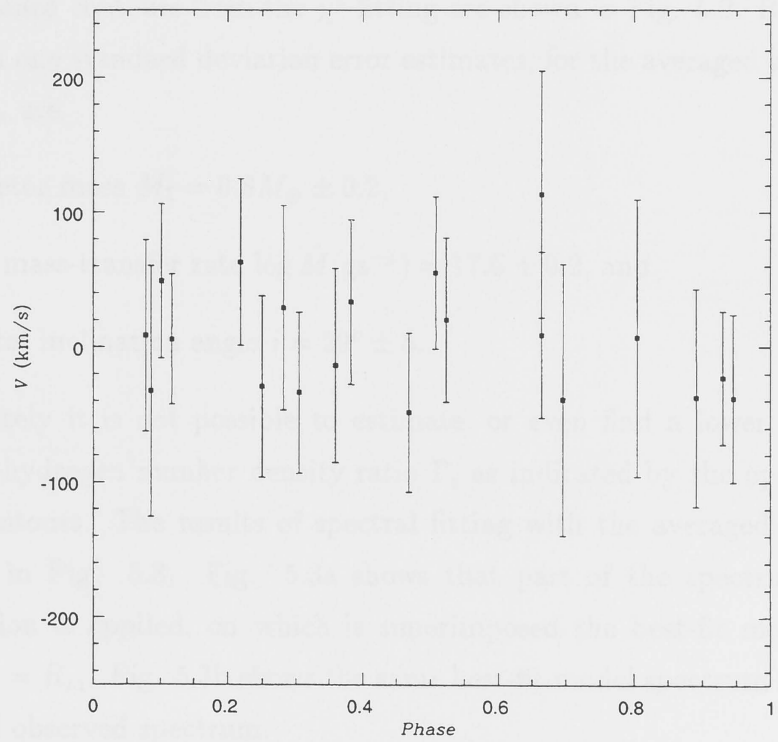

Figure 5.1: The phase radial velocities shown in Table 5.1

5.3 Fitting the Averaged Spectrum

Application of our χ^2-minimisation technique to spectral fitting requires one to assume a value for the outer accretion disc radius R_{out}. As discussed in El-Khoury & Wickramasinghe (1999), it is reasonable to assume that $R_{st} \leq R_{out} \leq R_{L1}$, where R_{st} is the maximum radius of the last stable orbit in the disc (Paczyński 1977) and R_{L1} is the Roche lobe radius of the accretor. Indications are that R_{out} is in fact closer to R_{L1}, and that is the value used here to present results.

Confidence contours from the χ^2-fitting are shown in Fig. 5.2. Best-fit parameters, with one standard deviation error estimates, for the averaged spectrum with $R_{out} = R_{L1}$ are

- accretor mass $M_1 = 0.8 M_\odot \pm 0.2$,
- disc mass-transfer rate $\log \dot{M}(\mathrm{gs}^{-1}) = 17.6 \pm 0.2$, and
- orbital inclination angle $i = 29^\circ \pm 5$.

Unfortunately it is not possible to estimate, or even find a lower limit for, the helium-to-hydrogen number density ratio Γ, as indicated by the open $i - \Gamma$ confidence contours. The results of spectral fitting with the averaged spectrum are presented in Fig. 5.3. Fig. 5.3a shows that part of the spectrum where χ^2-minimisation is applied, on which is superimposed the best-fit model spectrum when $R_{out} = R_{L1}$. Fig. 5.3b shows the same best-fit model spectrum superimposed on the full observed spectrum.

It is clear from Fig. 5.3 that the fit is not particularly good. This accounts for the problem in estimating Γ, and suggests that we cannot be as confident about these EC15530-1403 results as we are for the AM CVn fit reported in El-Khoury & Wickramasinghe (1999)

Even in the narrower spectral interval of Fig. 5.3a, there is a discrepancy in fitting the continuum within 4500 – 4900 Å. This is probably because metals are presently not incorporated in the model — a similar problem arises with CR Boo in El-Khoury & Wickramasinghe (1999). However Fig.5.3b shows a very significant discrepancy in the blue fit below 4000 Å. Any attempt to remedy this by fitting over

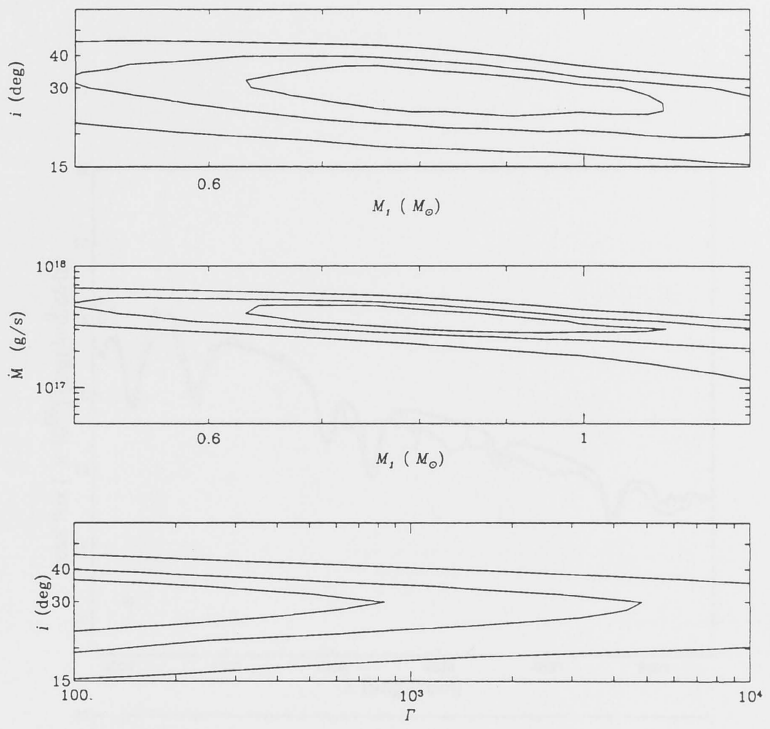

Figure 5.2: Confidence contours from χ^2-fitting of averaged spectrum for EC15330-1403 with $R_{out} = R_{L1}$. Inner to outer: 99%, 90% and 66% confidence level.

a wider wavelength interval only results in improved continuum fits, while modelled spectral lines become too shallow to fit those observed, and the M_1 contours cross the Chandrasekhar mass limit for white dwarfs. Use of $R_{out} = R_{st}$ instead of R_{L1} yields no better results.

5.4 Fitting the Phase Spectra

By applying the χ^2-fitting technique to the individual phase spectra obtained, we hoped to gain some insights on disc dynamics in EC15530-1403. For example, any disc wobbling could manifest itself through changes in the inclination angle i of the system; and significant differences in the R_{out} required for phase-fitting could indicate expansion or contraction of the outer disc regions.

Unfortunately, the phase-fitting results are inconclusive because of insufficient

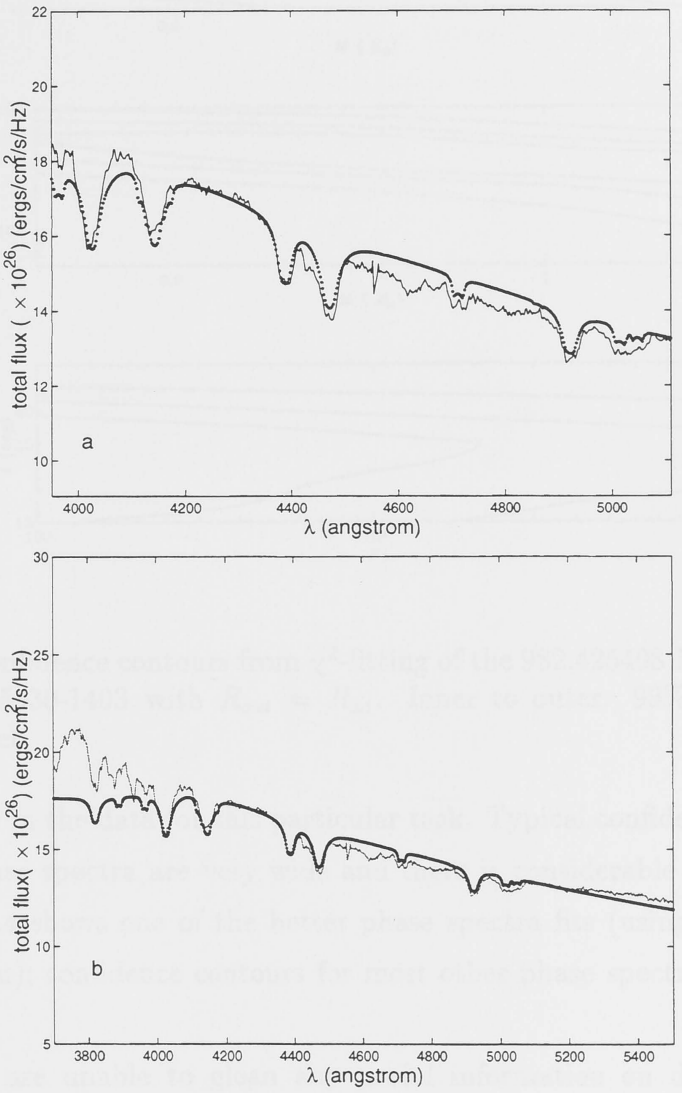

Figure 5.3: Observed averaged spectrum of EC15330-1403 (thin line) superimposed on the best-fit spectrum (thick line). Panel (a) shows that part of the spectrum where χ^2-minimisation is applied. Panel (b) shows the full spectrum.

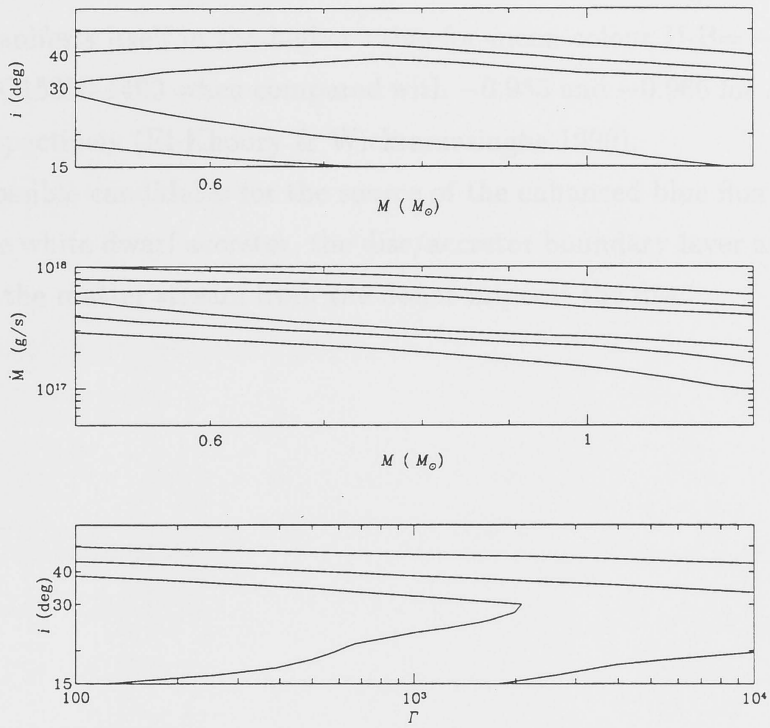

Figure 5.4: Confidence contours from χ^2-fitting of the 982.425408 MJD phase spectrum for EC15330-1403 with $R_{out} = R_{L1}$. Inner to outer: 99%, 90% and 66% confidence level.

signal-to-noise in the data for this particular task. Typical confidence contours for individual phase spectra are very wide and there is considerable overlap between them. Fig. 5.4 shows one of the better phase spectra fits (using the 982.424508 MJD spectrum); confidence contours for most other phase spectra are even more open.

Hence we are unable to glean any useful information on disc dynamics in EC15530-1403 from phase spectra fitting.

5.5 Conclusion

We conclude that standard models of thin accretion discs do not correctly predict the optical spectrum of EC15330-1403. In particular, there appears to be a con-

siderable spectral flux contribution from other sources in the region below 4000 Å: this also manifests itself in the higher value for mean colour U-B= −1.14 that we found for EC15330-1403 when compared with −0.955 and −0.966 for AM CVn and CR Boo respectively (El-Khoury & Wickramasinghe 1999).

Some possible candidates for the source of the enhanced blue flux in EC15330-1403 are the white dwarf accretor, the disc/accretor boundary layer and the bright spot where the matter stream from the donor impacts the disc.

Bibliography

[1] El-Khoury, W., & Wickramasinghe, D. T. 1999, A&A *submitted*

[2] O'Donoghue, D., Kilkenny, D., Chen, A., Stobie, R. S., Koen, M. C., Warner, B., & Lawson, W. A. 1994, MNRAS, 271, 910

[3] Paczyński, B. 1977, ApJ, 216, 822

[4] Warner, B. 1995, Cataclysmic Variable Stars (Cambridge: Cambridge Univ. Press)

Appendix A

Two-Stream Approximation for $\tau \gg 1$

We examine the asymptotic behaviour of our two-stream approximation to show that it converges to the diffusion approximation at large optical depths. For an outgoing radiation stream I^+, the solution to the radiative transfer equation is

$$I^+(\tau) = \int_\tau^\infty S(t) e^{-(t-\tau)/\mu_1} dt/\mu_1 \tag{A.1}$$

which, with change of variable $x = t - \tau$, becomes

$$I^+(\tau) = \int_\tau^\infty S(x+\tau) e^{-x/\mu_1} dx/\mu_1. \tag{A.2}$$

Using a Taylor approximation around τ

$$I^+(\tau) = \int_\tau^\infty (S(\tau) + x\frac{dS(\tau)}{d\tau}) e^{-x/\mu_1} dx/\mu_1 \tag{A.3}$$

whose solution is

$$I^+ = S(\tau) + \mu_1 \frac{dS(\tau)}{d\tau}. \tag{A.4}$$

Similarly, for incoming radiation

$$I^- = S(\tau) - \mu_1 \frac{dS(\tau)}{d\tau}. \tag{A.5}$$

Consequently for large optical depth $\tau >> 1$ and using $B = \sigma T^4/\pi$, we find

$$\frac{dT}{dz} = \frac{\xi F}{4\mu_1^2 acT^3}. \tag{A.6}$$

For the commonly-used two-stream approximation where $\mu_1 = 1$ (Shaviv & Wehrse 1986) then (A.6) gives

$$\frac{dT}{dz} = \frac{\chi F}{4acT^3}. \tag{A.7}$$

However if, as in our model, we take $\mu_1 = 1/\sqrt{3}$ then the diffusion equation is recovered, i.e.,

$$\frac{dT}{dz} = \frac{3\chi F}{4acT^3}. \tag{A.8}$$

Therefore our two-stream approximation is preferred to the commonly-used version.